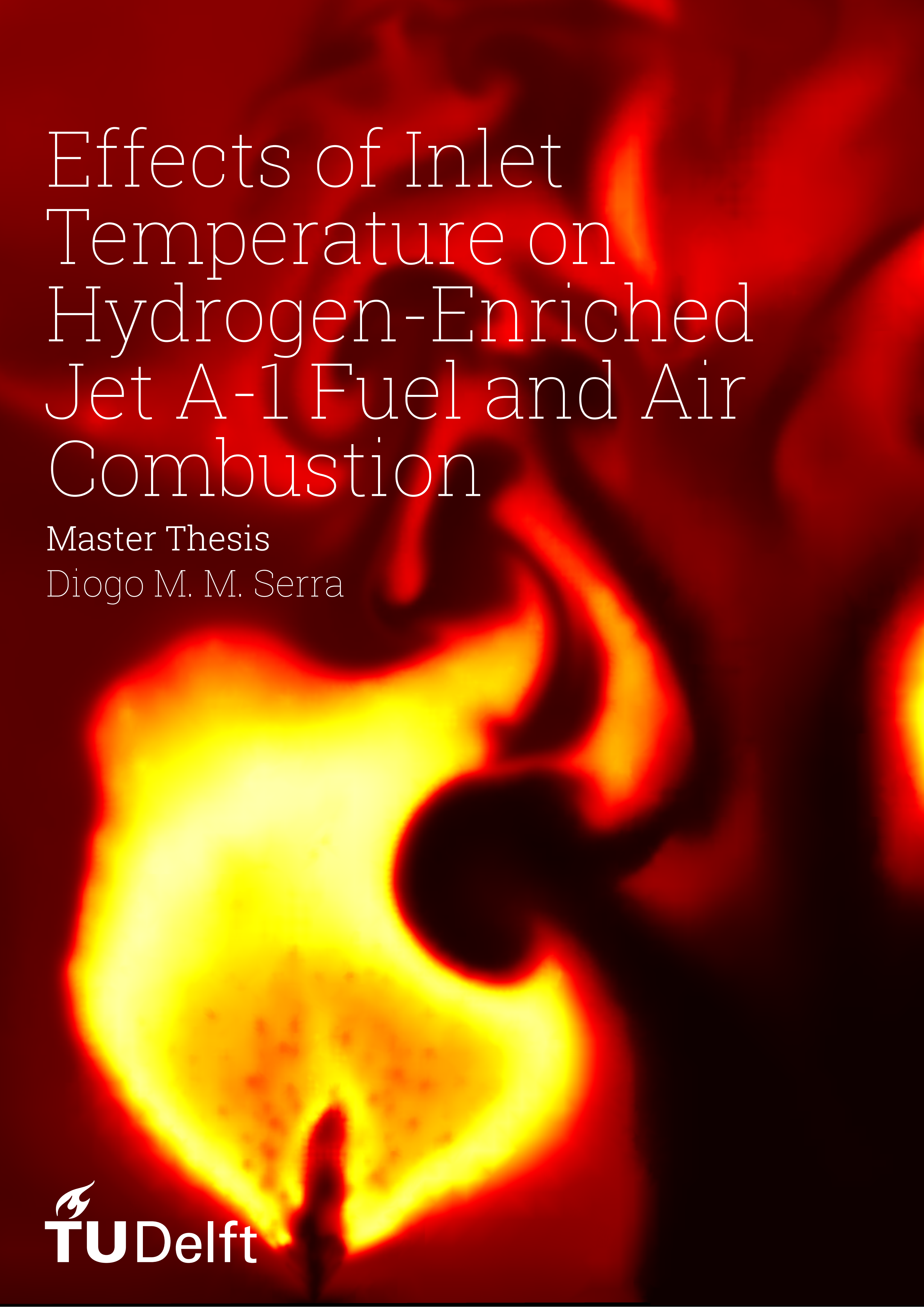

Effects of Inlet Temperature on Hydrogen-Enriched Jet A-1 Fuel and Air Combustion

Master Thesis

Diogo M. M. Serra

TU Delft

Effects of Inlet Temperature on Hydrogen-Enriched Jet A-1 Fuel and Air Combustion

Sunday 21st December, 2025

Student Name	Student Number
Diogo Serra	6067786

Supervisor:	Dr. Ivan Langella
Project Duration:	10 months
Faculty:	Faculty of Aerospace Engineering, Delft

TU Delft

Preface

I want to express my deepest gratitude to my PhD supervisor, Pablo Rouco Pousada, for his unwavering support throughout this project. His mentorship helped me close the significant learning gap I faced when I first started this project, and the experience in combustion modelling he shared with me undeniably enabled me to develop the full scope of this research. I also want to thank my supervisor, Dr. Ivan Langella, for his insights on how to tackle some of the challenges of data processing and analysis, and how to best approach the planning of such a significant project. I want to extend my gratitude to the Aerospace FPT PhD department at TU Delft for their support during the several setbacks I have had during this project. In particular, I want to thank Vittorio De Lauso for his invaluable insights on this research, which significantly elevated the work presented herein. These mentors and friends have supported me beyond the technical aspects of a thesis program and helped me develop the spirit I needed to ensure my work did not stop at the setbacks I faced.

I want to thank my friends, all the ones I met 15 years ago when I was just a kid, all the ones I met when I was 8000 Km away overseas, all the ones I met when I was facing hardship during university, and all the ones who met me in the Netherlands. It is pretty unbelievable that I ended up here, but even more so that all these people have not only stayed by my side all this time and supported me through all these years of academic hardships, including this project, but have also been there for every significant part of this journey. I genuinely believe I have become a far better person because of the impact they have had on my life, and sincerely wish I can continue to share in their journey and offer them the same unwavering support they gave me.

Lastly, I want to thank my parents for their support and the love they gave me throughout the thesis. It goes without saying that their impact is immeasurable on both the opportunities I've had and on the resilience I've shown in moments of adversity. I'm deeply grateful for everything they have done for me.

Abstract

A growing concern over the irreversible effects of global warming has led to the creation of international carbon neutrality goals by 2050. The mounting demand placed on the aviation sector creates growing pressure on new and innovative solutions to offset the growth in predicted aircraft emissions. Among many, hydrogen combustion offers a uniquely auspicious yet challenging approach to carbon neutrality in aviation. This project aims to study the effect of low temperature hydrogen and air injection on fuel mixing quality, the emission of secondary combustion pollutants, and the reaction zone interactions with the flow field. Large Eddy Simulations using detailed combustion models and a skeletal chemical kinetic mechanism are implemented to simulate the combustion of a hydrogen enriched jet A-1 spray flame. Using a scale model of the Auxiliary Propulsion and Power Unit (APPU) combustor, two similar simulations are set up, the first with an air/hydrogen inlet static temperature of 250 K and the second with an air/hydrogen inlet static temperature of 400 K. The final results are post processed and analysed. The results show a clear increase in mixing quality between hydrogen and jet A-1 when the temperature is decreased for this combustor geometry, strongly corroborating the initial hypothesis. Additional results suggest that the combined effect of lower injection velocity and lower temperature injection of air/hydrogen may lead to an increase in the flame stretch for the reaction zones closest to the injector and an increase in flame structure length. Analysis of species distributions reveals significant spatial variations across the combustor. Still, only a significant and conclusive reduction in CO emissions with a decrease in inlet temperature could be established. The limited computational resources associated with this research consequently limit the quantification of the observed phenomena, however, the analysed trends provide sufficient evidence to support the use of lower temperature hydrogen as a potential solution to the issues associated with the mixing of both fuels and towards lower emissions combustion.

Keywords Hydrogen-assisted combustion; Aircraft combustors; Aircraft emissions; Fuel mixing quality; Large Eddy Simulation (LES); Skeletal chemical kinetics; Detailed combustion chemistry; Flame stretch;

Contents

List of Figures

List of Tables

Abbreviations

AAI Axial Air injection.
AMR Adaptive Mesh Refinement.
APPU Auxiliary Propulsion and Power Unit.
ATF Artificially Thickened Flame.
AZ Adaptive Zoning.

BiCG Biconjugate gradient method.
BiCGStab Biconjugate gradient stabilized method.

CFD Computational Fluid Dynamics.
CFL Courant–Friedrichs–Lewy number.

DNS Direct Numerical Simulations.
DPM Discrete Phase Modelling.
DTFLES Dynamically Thickened Flame model for LES.

EDC/EDM Eddy dissipation Concept/Model.
ERF (Effective) Radiative forcing.

FGM Flamelet Generated Manifold.

HOPE Hydrogen Optimized multi-fuel Propulsion system for clean and silent aircraft.
HRR Heat Release Rate.

LBO Lean Blowout Limit.
LES Large Eddy Simulations.

NS Navier-Stokes.

PISO Pressure Implicit with Splitting of Operator.
pPV Pseudo Progress Variable.
PV Progress Variable.

RANS Reynolds Averaged Navier Stokes (simulations).
RV Radiative Factor.

SAF/AJF Sustainable Aircraft Fuel/Alternative Jet Fuel.
SGS Sub-grid (turbulent) scales.
SIMPLE Semi-Implicit Method for Pressure-Linked Equations.
SMD Sauter Mean Diameter.
SOR Sucessive Over-Relaxation.
SSD Stochastic Secondary Droplet.

UHC Unburned Hydrocarbons.

Nomenclature

Symbol	Definition	Unit
$U_{i,\text{tang}}$	Wall tangential velocity	m/s
u^*	Shear velocity	m/s
u^+	Non-dimensional streamwise velocity	-
τ	Specific stress	Pa/s
ρ	Density	kg/m^3
D_{th}	Thermal Diffusivity	m^2/s
S_l	Laminar flame speed	m/s
δ_l	Laminar flame thickness	m
$\dot{\omega}$	Specific reaction rate	kg/m^3s
$\dot{\Omega}$	Specific reaction rate (Freely propagating laminar flame)	kg/m^3s
Ψ	Jaravel's transported scalar	-
$\mathcal{F}$	Thickening factor	-
τ, α	Numerical timescales	s
$S, \hat{S}$	(Unfiltered,Filtered) sensor variable	-
V	Relative Diffusion velocity	m/s
$\bar{\Delta}$	Filter Width	m
C_s	Smagorinsky Constant	-
R	Rosin-Rammler cumulative probability of droplet diameter	-
B_d	Spalding mass transfer number	-
Sh_d	Sherwood number	-
ψ	Fuel to air ratio	-
W	Molecular weight	kg/mol
ERF	Effective Radiative Forcing	W/m^2
$\alpha_{c,\Psi}$	Cold-side sink timescale of Ψ	s
$\alpha_{h,\Psi}$	Hot-side sink timescale of Ψ	s
τ_{Ψ}	Source timescale of Ψ	s
GCS	Global Consumption Speed	m/s
I_0	Stretch factor	-
Re	Reynolds number	-
k_1, k_2, k_c	Forward/backwards rate coefficients of the Arrhenius equation	-
χ_m	Molar concentration	-
$\nu_{m,i}$	Stoichiometric coefficient of species m in reaction i	-
E_i	Activation energy	kJ/mol
A_i	Pre-exponential factor	-
S_0^i	Standard molar entropy	$J/(mol\,K)$
H_0^i	Standard molar enthalpy	$J/(mol\,K)$
M	Pope's M critereon for appropriate mesh resolution	-

1

Introduction

1.1. Review of aircraft emissions and clean energy goals

As concerns about global warming lurk around almost every service and manufacturing based sector of the economy, topics surrounding the reduction of aircraft emissions have taken centre stage in Aerospace research. Currently, the aviation sector accounts for 2% of the total CO_2 emissions and 4% of the global greenhouse emissions accounted for in a 2024 study by United Nations Environment Programme (UNEP) [1]. Predicting how these emissions will evolve over the coming decades has recently proven to be challenging, as the COVID-19 pandemic halted most air travel for nearly one year, highlighting uncertainties in past emission projections that did not account for this effect. ICAO emission reports from 2019 [2], and from 2025 [3] show that the pandemic will likely result in a reduction of the predicted total aviation emissions over the following decades compared to the previous estimates. As of the writing of this report, the pandemic is still a recent event, and the latest emission reports are still marked by uncertainties over how the market will recover over the next few years. However, newer data from European Commission, Climate Action [4] shows that aircraft emissions levels in 2023 equalled 80% of the emission levels reported before the pandemic, and while emissions have still not matched the previous estimates, these results suggest that the original trend might hold accurate over the long run as the demand for commercial flights returns to the estimated values[5] and emission levels are expected to reach a new record by 2025[6]. Attending to these emission reports, it can be estimated that fuel consumption, and consequently aircraft CO_2 emissions, is expected to triple or quadruple over the next 30 years if no other pre-emptive measures are taken to address this issue. Additionally, the reports also predicts a rise in NO_x emissions at altitudes below $915\,m$ by 2 to 3 times the current value over the same period, which directly translates into worse ground level air quality.

Aircraft emissions can be broken down into the unavoidable, direct products of a theoretically perfect combustion of fossil fuels, that is, CO_2 and H_2O, and the indirect by-products from the incomplete combustion of fuel and from several secondary reactions that lead to the formation and emission of Soot, NO_x, CO, Unburned Hydrocarbons (UHC), SO_x, among others. One study from Teoh et al. [7] modelled the emissions of a significant portion of all regional and international flights in 2019 and estimated that the aviation sector was responsible for the emission of 892 Tons of CO_2 and 348 Tons of H_20, which would be expected from the reported 283 Tons of fuel burn. These emissions constitute an overwhelming majority of aircraft emissions and directly contribute to the greenhouse effect. The emission rates of both pollutants are relatively constant across different engine technologies. On the other hand, the same model also estimated that, in total, as many as 4.49 Tons of NO_x, 0.4 Tons of CO, 0.34 Tons of SO_2, and 0.02 Tons of soot were emitted from all the recorded flights in this database. Despite these indirect pollutants making up a fractional portion of the total emissions count, the impact on the atmosphere is still significant and unique.

The specific impact of aviation emissions on global warming has been previously studied with the use of a Radiative Forcing (RF) factor, which measures the change in the balance between incoming and outgoing infra-red radiation from the earth's atmosphere immediately after the pollutant is introduced into the atmosphere, and the Effective Radiative Forcing (ERF) which measures the same change but taking into account fast changing atmospheric phenomena that may or may not result in a suppression of the impact that pollutant has on the net infra-red radiative flux. Lee et al. [8] studied and estimated the impact of each of the common aircraft emissions using this metric, and the data collected in Figure 1.1 highlights how each pollutant contributes to the greenhouse effect. Using this analysis, it can be seen that CO_2 has a consistent and significant long term impact on the radiation flux balance, making its impact on the greenhouse effect fairly predictable. The other direct pollutant, H_2O, has a much less significant direct impact on the RF, however, it can lead to the formation of contrails, which do significantly change this balance, even when accounting for the short term dissipation of these formations, as observed from the ERF metric in Figure 1.1.

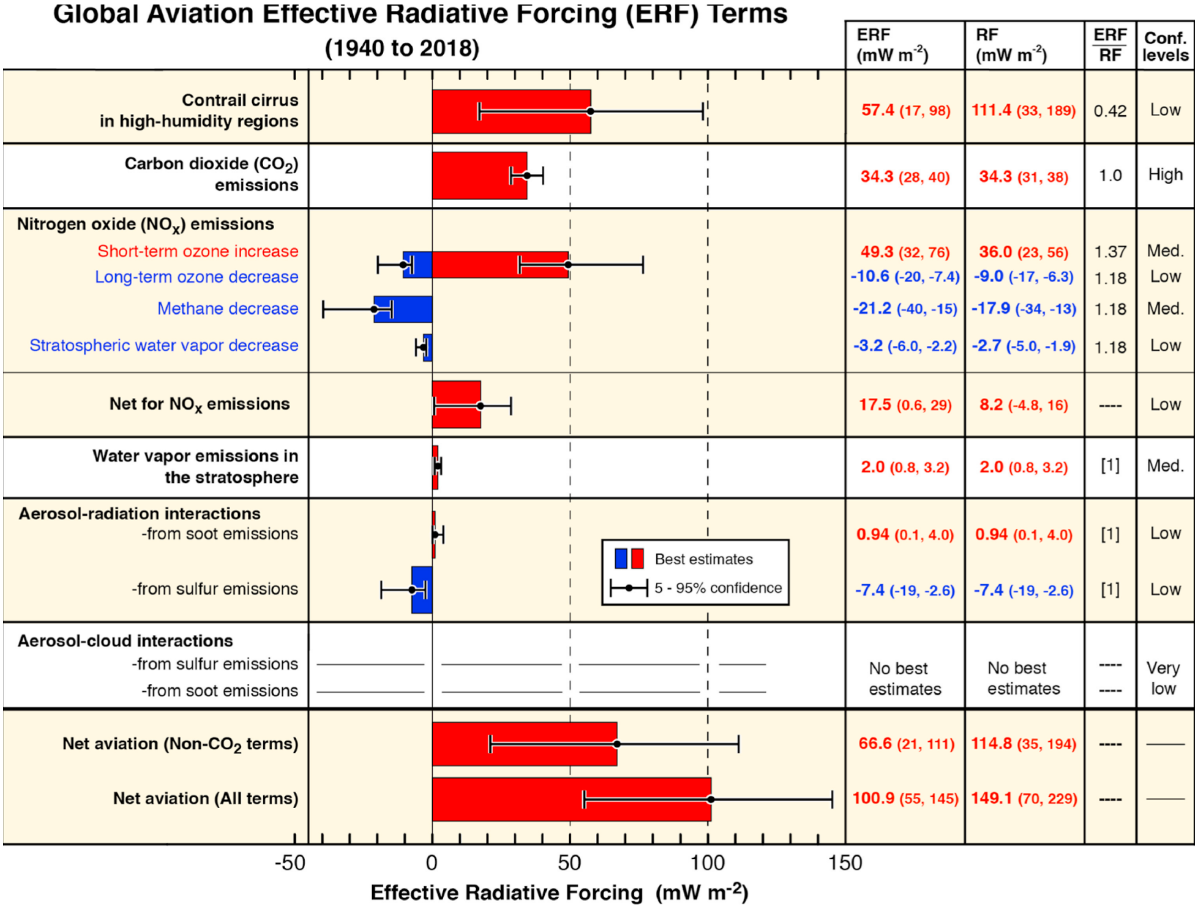

Figure 1.1: Best estimates for climate forcing terms from global aviation from 1940 to 2018. The bars and whiskers show ERF's best estimates and the 5–95% confidence intervals, respectively. Red bars indicate warming terms and blue bars indicate cooling terms. Numerical ERF and RF values are given in the columns with 5–95% confidence intervals along with ERF/RF ratios and confidence levels. Courtesy of [8].

Not only is NO_x a greenhouse gas, with the increase of this species immediately leading to the increase of overall RF, but it has also been studied to be the dominant contributor to changes in atmospheric ozone and aerosol concentration, dominating changes in surface air quality [9]. NO_x emission traceable to aircraft operations has been found to significantly worsen annual human exposure to particulate matter, which is typically not seen with CO_2 or H_2O emissions [10][11]. Lee et al. [8] quantified some of these effects in their ERF calculations (Figure 1.1) which further allows for an interpretation of the impact of NO_x emissions on the greenhouse effect compared to CO_2, and while the combined effect of all the long term phenomena will result in an $ERF < 1$, the short term increase of ozone due to this pollutant will have a significantly higher impact on global warming than CO_2. Additionally, beyond the greenhouse effect, NO_x alongside SO_x are both responsible for the formation of acid rain that disrupts crop formation [12].

Soot emissions represent a small direct contribution to global warming compared to almost all other emissions as account for by [8], however it has been suggested that the impact of soot might be higher at cruise phases, where soot might interact with contrails to increase their ERF further [8], [13], [14]. The lack of research on this topic results in low confidence estimates for the real impact of soot, however it's reusable to say that this pollutant should be reduced as it leads to the decrease in air quality around airports [9].

Although UHC and CO are typically not directly responsible for significant changes in ERF values and are not considered significantly impactful greenhouse gases, their impacts on air quality and atmospheric phenomena have been well documented. Most concerningly, when injected into the atmosphere, CO can react with NO_x to form ozone, CO_2, and other greenhouse gases, which do play a significant role in increasing the RF [8]. Both UHC and CO emissions are considered hazardous air pollutants and have been linked to adverse health effects [15].

The concern placed on aircraft emissions reflects the knowledge that has been obtained about the impact of each pollutant on the greenhouse effect, air quality, and, by extension, human and animal health. If predicted trends accounting for the lack of action towards the carbon neutrality targets are realized, then the impact of aircraft on the atmosphere could become far more dominant. Alternative trends that reflect the existing effort towards the reduction of some or most of these pollutants have been made and show a more optimistic outcome for the next 30 years, depending on the success of upcoming technologies [2].

1.2. Alternative jet fuel for the reduction of aviation emissions

The 2025 ICAO emission trend report [3] underlines a series of strategies for the reduction of the estimated emissions over the next decades and shows that aircraft technology improvements account for the most significant reductions in emissions directly emitted by aircraft. Furthermore, the best scenario for the adoption of alternative aircraft fuels as a replacement for traditional jet fuel blends can yield an additional 53% reduction in total CO_2 emissions (including lifecycle emissions), in addition to the aforementioned CO_2 reductions. Current action focuses on the development of fuel efficient engines such as high bypass ratio engines, alternative fuel powered propulsion systems such as hybrid or fully electric propulsion systems, lightweight materials and fuselage drag reduction strategies and on the implementation of alternative jet fuels (SAF/ATJ).

The use of SAF has been strongly encouraged as a readily applicable emission reduction strategy and $Drop-in$[1]. SAF blends are currently at a Technology Readiness Level category of 8-9 and already represent close to 0.5% of all jet fuel consumption as of 2024 [3], [16]. Current commercially viable $Drop-in$ SAF blends are similar in chemical composition and thermodynamic characteristics to typical aircraft fuels and are typically only used in blends of up to 50% with typical aircraft jet fuel [17]. Consequently, the impact on aircraft emissions from the use of SAF is negligible when considering only direct aircraft emissions. However, depending on fuel sources and production pathways, CORSIA certified sustainable aviation fuels are reported to have significantly lower lifecycle emissions compared to the lifecycle emissions of typical aircraft fuels [18], [19]. Independent studies have also found that the implementation of SAF can lead to measurable improvements in air quality near airports [15]. Furthermore, a recent climate modelling study has found that not only significant equivalent CO_2 emissions reductions can be achieved for certain SAF, depending on the production pathways, but also that this positive effect scales with flight range [20]. Future directives by the ReFuelEU aviation initiative have set goals for 70% of all aircraft fuel to be sourced from sustainable pathways by 2050 [16], [21], reflecting an optimistic push for SAF in efforts of reaching carbon neutrality within the next 30 years.

However, the current limitations of SAF pose significant obstacles to the goals defined by the ReFuelEU initiative. A report from the U.S. department of Energy [17] highlights the high costs of SAF production and certification relative to traditional jet fuel, the limitations in the feedstock availability that tighten the production rate of SAF, the lack of sufficiently similar fuel properties for some of the production pathways that limit operability limits and typically restrain the use of SAF to a certain blend and lack of policy incentives for the use of SAF as reasons for the slow adoption of SAF into the market. Despite the current availability of SAF, market research suggests that a significant amount of technology research

---

[1] $Drop-in$ SAF fuel blends refer to fuel blends that can be used in traditional aircraft engines

and investment is needed in both aviation and all the sectors of feedstock production, which presents a considerable challenge in itself. Furthermore, if a combination of policy, funding and research align to overcome the challenges of SAF until 2050, the estimated reduction in overall CO_2 emissions [3] might be offset by the environmental impacts of increasing the feedstock production rate and any sudden rise in total passengers per year, leading to an ambiguity of whether the investment will lead to the goals defined for CO_2 emissions in and out of the aviation industry [22], [23]. For this reason, research on fuel reduction strategies is currently diversified beyond the use of already existing SAF.

An alternative strategy with the potential to curb CO_2 emissions at their source is the use of non-$Drop-in$ SAF. These fuels are held back by either limitations in current engine and facilities technology or by constraints associated with the fuel itself. Non carbon based alternatives such as hydrogen and ammonia, and the research associated with these alternatives, are underlined as highly promising strategies for deeper carbon emission cuts by governmental aviation agencies [3], [16]. The face value of this alternative is the reduction of carbon emissions roughly proportionally to the blend ratio of jet fuel with hydrogen based SAF, where an aircraft running on 100% hydrogen based SAF will not emit any carbon emissions. However, the lack of infrastructure and regulations to deal with the storage, transport, and consumption of hydrogen, either in its liquid or gaseous form, and the issues related to the energy extraction from hydrogen, either by direct combustion or by the spontaneous redox reaction associated with hydrogen fuel cells, presents serious challenges for the use of hydrogen in aviation [24]. Current trends by the Air Transport Action Group [25] suggest that, if focus is directed towards the successful development of electrification of the propulsion based systems and towards the hybridization and electrification of large and small aircraft propulsion systems, then hydrogen could represent up to $20-25\%$ of total aviation fuel consumption by 2025. This scenario is overly optimistic and arguably unrealistic as it assumes a significant shift in the technological state of the art and in policies over a short period of time. However, it reveals a potential end goal of the development of hydrogen based propulsion systems. The feasibility of these trends depends on the effort invested in researching solutions to the many challenges faced by these $Drop-in$ SAF.

1.3. Hydrogen as an alternative fuel

As an alternative fuel, liquid and gaseous hydrogen requires extensive research and investment to become economically and regulatory viable. Liquid hydrogen has a mass energy density close to three times that of traditional jet fuel [26] and is about 100 times more energy dense than typical market batteries, representing a much lighter option compared to other fuels and propulsion systems. The issue, however, is that long term liquid hydrogen storage is impractical and requires systems capable of handling the extreme storage conditions [27]. The storage issue can be alleviated by keeping hydrogen in its gaseous state, however, the volumetric density of gaseous hydrogen is several hundred times less than that of typical carbon based fuels [26], requiring unreasonably large storage volumes typically not achievable for aircraft. Even so, studies suggest that long haul aircraft specifically optimized for pure hydrogen combustion can significantly benefit from a reduction in total energy consumption [26], [28], [29].

The use of hydrogen in fuel blends has the trivial impact of lowering the carbon based emissions compared to the same amount of traditional jet fuel burned since it lacks any carbon in its chemical description. Additionally, it has been reported that hydrogen is able to diffuse and mix with air far more efficiently when compared to typical jet fuel, which, when paired with the smaller lean flammability limit of a hydrogen/air combustion, can allow for combustor designs with a reduction of up to 90% in nitrogen oxide emissions [30], [31], [32]. Hydrogen is not entirely emission free, as one of the primary products formed from this combustion process is water. For the same energy released, hydrogen combustion can produce up to 2.6 times more H_2O than typical jet fuel combustion, which although concerning since the impact of H_2O on the upper troposphere is still not fully understood, current climate models have shown that the reduction of carbon based emissions off-sets the impact due to increase in H_2O emissions on global warming [30], [33].

Concerns over hydrogen combustion in aircraft are often centred on the differences between a hydrogen flame and a kerosene flame in the same combustor, which make hydrogen a Non $Drop-in$ fuel and require a significant overhaul of current engine technology. Hydrogen diffuses and mixes in the combustor far faster, and the resulting flame speed is ten times as fast as the flame speed of typical kerosene or methane mixtures in aircraft combustors [34], [35]. This behaviour increases the risk of flashback in combustors where hydrogen is injected upstream with the oxidizer, as hydrogen mixtures can be observed to be within flammability limits much closer to the injection point and can lead to a premixed flame that quickly travels upstream for a combustor design that is not engineered for the new flame speeds. New combustor designs account for this risk of flashback by either keeping the hydrogen to jet fuel blend ratio low, increasing the injected flow velocity to avoid flashbacks or by using novel Micro Mixing combustor technologies [32], [35]. Furthermore, depending on the combustor configuration, the production of NO_x emissions might be amplified by the formation of high-temperature hydrogen flames, which enhance NO_x production through thermally activated pathways that would otherwise not be as active in typical jet fuel flames [34], [35].

Hydrogen can also achieve the same net-zero goals established by the ReFuelEu initiative through the reduction of lifecycle emissions. Some of the production pathways, such as ”black hydrogen” production using coal, ”grey hydrogen” production using gas, ”blue hydrogen” production using gas but with CO_2 sequestration and ”magenta hydrogen” production with methane dissociation, also lead to the production carbon based emissions that are either emitted into the atmosphere or retained in containers. Other alternative production pathways such as ”green hydrogen” production, do not produce any carbon based pollutants, yielding zero lifecycle carbon emissions. Depending on how pollutants are accounted for, ”green hydrogen”, ”magenta hydrogen” and ”blue hydrogen” might allow for the production of hydrogen with net zero emissions of carbon based pollutants. Depending on the market evolution and future investments, a framework can be built for the increase of production of hydrogen through ”green hydrogen” production pathways, paving the way for a strictly net zero fuel alternative [35].

Hydrogen stands as one of the most promising SAF that could help achieve the 2050 aviation emission goals. However, significant challenges have hindered its use in the current industry. A review of the current state of liquid hydrogen use in aviation [32] highlights projects such as FlyZero from the Aerospace Technology Institute [36], HySIITE from Pratt & Whitney [37] and CRYOPLANE from Airbus Deutschland GmbH [38] and their successes in in assessing the viability of hydrogen as a alternative fuel for net-zero carbon emissions, either by the direct combustion of hydrogen or by the use of hydrogen fuel cells. Common challenges of these approaches include the lack of sufficiently advanced technology state of the art to address the issues with storage, combustion and transport of hydrogen in its critical conditions and consequently the high cost necessary for the development of these technologies.

1.4. Synthesis of relevant fields of work

Facing the challenges posed by a growing global warming problem with limited time for impactful action, the growing demand from the aviation industry is mounting pressure on research into emission reduction strategies. The impact of the reduction or increase of each pollutant species on global warming is often evaluated separately to assess the net change in global radiative forcing relative to reference levels. The result of this analysis allows for the classification of each strategy according to its net climate impact.

One of the most promising strategies is the use of SAF as an alternative to traditional jet fuel. The reduction of lifecycle CO_2 emissions from $Drop-in$ SAF currently account for the majority of total CO_2 emission reductions estimated by the scenarios proposed by ICAO, EASA [3], [16]. Current challenges with the introduction of SAF into the market postulate serious doubts over the optimistic scenarios for 2050 and suggest that research could continue and extend into non $Drop-in$ SAF with greater potential for reduction in aviation emissions. This review covers the choice of hydrogen as a potential SAF and the significant benefits associated with its implementation, potentially in conjunction with $Drop-in$ SAF. The current scientific panorama points to several issues with the feasibility of hydrogen as a SAF and highlights a growing interest in addressing issues with hydrogen combustion stability, hydrogen storage and transport costs and lack of advanced technology to allow for the operation of hydrogen powered aircraft with a measurable positive climate impact.

Past hydrogen aircraft projects further incentivize additional studies on each of these issues. In this particular study, there is an interest in studying the dynamics of hydrogen combustion and exploring possible methods of reducing high temperature regions and improving emissions from the combustion of jet fuel and hydrogen blends in a typical model combustor.

2

Literature Review

A plethora of studies have been conducted on numerical and experimental combustion, including the combustion of hydrogen, hydrogen/jet fuel blends and numerical combustion in LES, which encompass the relevant topics necessary to conduct this research. The literature collection presented in this chapter draws relevant conclusions and suggestions regarding the typical behaviour of hydrogen/jet fuel flame structures, including findings on emission reductions, changes in emitted species distributions, changes in flame structure and flammability limits, and relevant modelling approaches used in similar problems.

Although the change in primary combustion emissions is trivial with the change in mass ratio of hydrogen to jet fuel in a fuel blend, the change in secondary emissions is far more dependent on the specific combustor conditions. However, several studies [39], [40], [41], [42] have shown consistent and conclusive evidence that the CO emissions are drastically reduced with just a small mass percentage of H_2 injected. This effect has been associated not only with the replacement of a carbon based fuel with hydrogen but also with the increased concentration of free oxygen radicals, which speed up the CO oxidation.

Concerns over the increase of NO_x emissions have been brought up over the existence of higher temperature hydrogen flame structures influencing the thermal NO_x formation mechanism [34], [35]. While some experimental studies [39], [40] have shown a significant increase in NO_x emissions with the injection of H_2, other studies [41], [42] suggest that this increase is not significant and some studies [43] suggest that the effects are significant but only after a certain mass flow of hydrogen (in relation to the jet fuel mass flow) is achieved. This disagreement in results has also been noted by other authors [44]. Burguburu et al. [39] suggested that the NO_x formation mechanism was highly influenced by mixing quality[1], which could partially explain this discrepancy between results. The study looked at the effects of hydrogen injection on fully premixed and partially premixed flames and found that partially premixed hydrogen/jet fuel flames had a tendency to form local hydrogen/air pilot flames near the injection ports, which was found to lead to areas of high NO_x production and overall lead to the formation of more NO_x compared to fully premixed flames. Most of the aforementioned studies attribute the cause of higher NO_x emissions to the increase in flame temperature, associated with the thermal NO_x formation mechanism, however it is important to note that this is not the isolated cause and that other mechanisms such as the prompt NO_x mechanism seem to be responsible to higher NO_x production even when the flame temperature is kept constant [39]. Dave et al. [44] studied the changes in flame structure and noted that the formation of soot was affected by hydrogen injection, and a visible reduction of soot emissions was recorded. This observation is also consistent with other experimental results [43].

Numerical investigations mostly agree with the experimental results. By simulating a n-decane combustor with hydrogen enrichment, Hui et al. [45] observed that NO_x production rate was heavily dependent on equivalence ratio after the hydrogen injection, and not necessarily on just the hydrogen concentration. Palanti et al. [46] studied the NO emissions of a kerosene/hydrogen flame and not only confirmed that NO_x production increased significantly in the combustion of 2 poorly mixed fuels but also showed

---

[1] In this work, mixing quality is used to assess how homogenous the mixture between fuels is.

that poor mixing of hydrogen/kerosene can lead to higher NO$_x$ emissions compared to just hydrogen flames or just kerosene flames. However, the authors admitted that NO$_x$ production in the simulation is exaggerated and potentially affected by the RANS model used and further simplifications.

Hydrogen is theoretically expected to react much faster, and the resulting flame speeds are typically several times higher than the reaction speed and flame speed of typical jet fuels in a traditional jet engine combustor. The exact behaviour of a mixture of hydrogen and kerosene, however, is still a subject of research as the perfect premixing between both fuels is often not consistently attained across different combustion case setups. Richards et al. [47] used an experimental test combustor to enrich a partially premixed, spray injected kerosene mixture with hydrogen and concluded that the injection of hydrogen leads to an increase in the flame propagation speed, which, for this test combustor model, most likely further indicates an increase of overall flame reactivity with hydrogen addition. Other numerical and experimental studies have also backed up the general increase in flame speed when hydrogen is used to enrich hydrocarbon flames [48], [49]

Zeng et al. [50] numerically resolved spherically expanding premixed flames and found that the Markstein number decreased with hydrogen content in a spherically expanding RP-3 kerosene flame, which points to the decrease in flame stability with hydrogen addition. Furthermore, using an experimental setup, the same study found that the surface of a spherically expanding premixed flame became increasingly rugged with hydrogen addition, further indicating the growth in flame instability under these conditions. On the other hand, additional experimental studies [41], [43] have found that hydrogen enrichment can significantly extend the flame extinction limits towards lean conditions, which gives way for the reduction of NO$_x$ emissions at lower combustion temperatures through the use of dry-low-NO$_x$[51] combustors and MicroMix combustors [35]. Burguburu et al. [40] showed that for a partially premixed flames there is the chance for the formation of local hydrogen pilot flames that help further stabilise the flame and extend the flammability limits. Richards et al. [47] noted that the hydrogen pilot flames operate in lean conditions considerably past the Lean Blowout Limit, but are maintained through the energy output of the kerosene flames. The author concluded that the kerosene flames are, in turn, maintained and stabilised by the hydrogen flames and vice versa. Numerical studies also confirm the stabilising effect of hydrogen addition to the overall hydrogen/jet fuel flame, underlining the role of hydrogen in reducing the auto-ignition delay of a kerosene flame, especially at higher temperatures [45], [52].

The combustion efficiency of a gas turbine has been linked to the mixing and evaporation quality of the fuel in a previous experimental study by Lefebvre [53]. A number of research papers [44], [47] have pointed out that the addition of hydrogen to a kerosene flame significantly improves the evaporation rate of kerosene droplets, leading to the better mixing of kerosene/hydrogen, reducing the incomplete combustion of kerosene and increasing combustion efficiency. Hiroyaso et al. [43] showed that with an increase in hydrogen concentration, the combustion efficiency increases up until a certain hydrogen injection rate. Annushkin and Maslov [54] showed that in a straight duct, the enrichment of hydrogen initially leads to an increase in combustion efficiency as the additional hydrogen concentration leads to an increase in the reaction rate of the combined flame, this efficiency starts decreasing with the improper mixing of fuels. This review is to suggest not only that hydrogen enrichment can lead to the overall increase in combustion efficiency but also that some of the reduction of CO emissions, can be attributed to this increase in efficiency and not just to the decrease in carbon content of the fuel mixture.

Some research has focused on improving the kerosene and hydrogen mixing quality in order to avoid high temperature, pure hydrogen pilot flames upstream of the main kerosene flame. Palanti et al. [46] studied the effect of different injector configurations in the Auxiliary Propulsion and Power unit (APPU) combustor and found that NO$_x$ emissions were reduced when better mixing was achieved due to a decrease in high temperature regions. In the same combustor, Dave et al. [44] experimentally observed that mixing is improved with an increase in hydrogen mass blend ratio, leading to changes in flame topology. However, on a different test combustion chamber, Annushkin and Maslov [54] found that an increase in injected hydrogen past a certain threshold led to a decrease in combustion efficiency, likely associated with poorer fuel mixing. This means that the imperfect fuel mixing is not due to an insufficient amount of hydrogen, even though hydrogen should diffuse and mix much faster than kerosene in the domain, but rather due to other factors such as the hydrogen flame's higher consumption speed and the hydrogen's lower ignition delay. Some studies [55], [56] have looked into the behaviour of hydrocarbon and hydrogen fuel blends at cryogenic temperatures and have consistently found an exponential relation between unburned mixture temperature and laminar burning velocity. These studies suggest that by controlling the temperature of the unburned mixture, the laminar (and possibly turbulent) flame speed can be controlled and attenuated, possibly addressing the issue of hydrogen pilot flames being formed upstream of the flame front. Unfortunately, as of the knowledge of the author of this project, there are no studies that specifically look into this possibility.

2.1. Past work in numerical fluid modelling

2.1.1. Fluid flow field modelling

In order to simulate hydrogen injection, 3 of the most common approaches can be taken: Direct Numerical simulations (DNS); Large Eddy Simulations (LES); Reynolds Averaged Navier Stokes (RANS) simulations. DNS simulations are often prohibitively expensive and are only performed with small scale geometry, which makes this approach not suitable for the size of the combustor to be tested. RANS and LES simulations are both valid options, but have significant drawbacks. RANS is often used in research [57], [58] as a low computational cost solution alternative, which allows for simulations using coarser grids and larger geometries, such as a gas turbine, while keeping the computational resources low, allowing for a broader study of combustion characteristics. RANS has been shown to compute fluid flow solutions with acceptable results given the use of appropriate models [59]. However, since none of the scales are resolved, RANS can not correctly capture scalar fluctuations, often leading to incorrect pollutant emission values. Additionally, since all scales are Favre averaged, RANS computed solutions are often characterised by an over prediction of model attributed diffusiveness of turbulent kinetic energy and overall scalar gradient smoothing, which can lead to inaccuracies when solving for thin flame front characterised by sharp gradients.

LES, on the other hand, is considerably more computationally expensive than RANS, requiring a much finer grid because it models only smaller turbulent structures below a filter size corresponding to the scales at which turbulent kinetic energy dissipation is more relevant. The main advantage of exactly solving large scale turbulent eddies for combustion modelling boils down to the lack of any averaging of scalar fields, leading to a solution that better captures sharp gradients and sensitive interactions between flow turbulence and the flame front. Furthermore, the better accuracy in scalar diffusion computations leads to a better description of scalar mixing, which is relevant for studying the detailed behaviour of the flame structures in complex flows. As a result, although research is often limited in the allocated computational budget, academia has shown a recent and consistent shift towards the use of LES in order to better model more detailed chemistry with faster reactants such as hydrogen [60].

In his work, Pope [61][62] outlined that for turbulent combustion, the relevant molecular mixing and chemical reaction phenomena are most predominant at the smaller scales. In this sense, since both LES and RANS models model these scales, the choice between the two models is ambiguous, and the return from the investment in a more expensive simulation might not be worth the additional resources. However, in simulations where the flow is not properly premixed, correctly modelling the momentum transfer over larger scales can theoretically yield far better results compared to RANS. Furthermore, for sufficiently low filter sizes, the LES model can approximate the ideal *pure physical* LES, which yields results equiparable to DNS and would not be feasibly achieved with RANS models.

The turbulence model used in combustion modelling is important to the correct calculation of turbulent combustion interaction. Yilmaz et al. [59] explored different turbulence models for RANS in order to model hydrogen combustion and found that the realizable $k-\epsilon$ was capable of correctly predicting pressure, temperature and species concentration profiles. Furthermore, the study outlined that some models, such as the standard $k-\epsilon$ and RSM, might be inadequate for this type of modelling. Alabaş and Çeper [63] modelled the combustion process using realizable, standard and RNG k-ϵ on a colourless distributed combustion combustor with good validation results for the standard and realizable eddy viscosity closure models. Smirnov and Nikitin [64] also modelled a hydrogen combustion chamber using a modified $k-\epsilon$ model to better account for temperature deviations and found the model to give reasonably accurate results when compared to experimental data. Palanti et al. [46] chose to use the k-ω SST model in order to correctly capture wall interactions while still having the $k-\epsilon$ model compute the free stream flow field. It was also found that at least 1 study[58] used the Reynolds Stress Model (RSM), however, no further explanation is given, and the same model has been shown to be unstable in other studies and reviews [59], [65].

2.1.2. Combustion modelling

In LES, closure models are required to model the sub-grid scales (SGS) scalar fluxes and the unresolved SGS transport terms [66]. One of the simpler models, the (laminar steady) flamelet model, that assumes that a multi-dimensional flame can be reduced to a one dimensional flame, has been used in previous studies with hydrogen flame combustion [67]. It is a viable model for when the reaction rate is so great that the reaction zone is deemed too thin to be significantly affected by turbulence, however, it over simplifies the flame front by assuming that the internal flame structure is never affected by even the smallest turbulence scales. Alternative models exist, such as the Flamelet Generated Manifold (FGM) by Oijen and Goey [68]. FGM adapts the simplistic one dimensional modelling of the progress variable from the original flamelet model in order to model additional progress variables, which allow it to correctly capture premixed flames and increase overall prediction accuracy. Lemmi et al. [69] studied 2 different approaches of capturing the flame front, the Flamelet Generated Manifold (FGM) and the Artificially Thickened Flame (ATF), and found that both models could accurately resolve the velocity and pressure fields of hydrogen enriched methane flames. The study, however, outlined that both models might struggle with flames that undergo high stretch. Pérez-Sánchez et al. [70] simulated hydrogen/air flames and found that the FGM model is capable of correctly simulating flame structure and propagation.

FGM might not correctly account for kerosene combustion compared to other models, as these flames have higher Karlovitz numbers than hydrogen flames, making them subject to the effects of the smallest turbulent scales [71], contradicting the one dimensional flame assumption. Additionally, as a consequence of being a flamelet model, FGM assumes that there is a homogeneous diffusion of species through the flame front, which is a very aggressive assumption for a hydrogen/kerosene flame. However, this issue can be resolved by combining information between premixed and non premixed flames into a single manifold, which has led to the significant improvement in accuracy of diesel/hydrogen flames [72]. It is also worth noting that some studies have looked into increasing accuracy by incorporating FGM with Artificially Thickened Flame model(ATF), which aims to artificially increase the timescales such that the flame can be properly resolved, theoretically allowing for the the chemical source terms to be computed without the use of combustion models, albeit at the expense of being a expensive computational model. Kuenne et al. [73] used the ATF model, with a dynamic scaling method, coupled with the FGM model. This coupling allowed the researchers to correctly resolve the timescales of the relevant species while accounting for the effect of the remaining chemical reactions on the flame propagation speed and temperature with the FGM tabulation. The results for a methane flame showed good agreement with the experimental data. Wan et al. [74] simulated a kerosene flame using ATF coupled with FGM in order to correctly capture the flame structure and found fairly good agreements between experimental and simulation datasets. Although at the time of this research, no studies are openly available on the use of this coupling in hydrogen/kerosene flames, one predictable problem with this approach is the markedly different timescales of the primary reactions between hydrogen/air and kerosene/air, which will significantly increase the computational time. Additionally, if improper mixing is observed, several flame fronts can form, leading to strong interactions between flames that the model would not accurately capture.

Alternatively, the Eulerian Dissipation Model (EDM) by Magnussen and Hjertager [75] and derivatives such as the Eddy Dissipation Concept (EDC) can be used for the closure of the filter scale chemical reaction rates. This model assumes that the reaction rate is far lower than the mixing rate, making it so that reaction timescales are limited by turbulent mixing and dissipation timescales. The reaction rates are thus determined from either the mixing and dissipation rate of oxygen, fuel or products, whichever is the minimum rate. In practise, this implies that combustion only happens in well mixed zones[60]. Although this model has been used in the past for kerosene/hydrogen combustion simulations [46], the limitations associated with the strong assumptions made with this model often do not justify its use in more complex cases, leading to limited applicable cases [60].

Most of the aforementioned models rely on aggressive simplifications of the combustion process, which greatly improve model performance at the cost of limited applicability and the inability to accurately capture certain phenomena (e.g., flame extinction in FGM). The detailed transient chemistry solver (SAGE) model by Senecal et al. [76] differentiates itself from these models by solving detailed chemistry steps from a set of pre-defined chemical reactions. This model uses a previously tuned and validated chemical kinetics model to directly solve for the chemical species concentrations and production rates ahead of the transport equations for each time step, coupling the chemistry computations to the remaining LES simulation. This model is expected to be computationally expensive, however, CONVERGE offers the use of techniques such as Adaptive Mesh Refinement (AMR) and Adaptive Zoning (AZ) to improve accuracy by further refining the flame front and to group cells in order to reduce the number of chemical kinetic calculations performed, respectively.

Most of the mentioned combustion closure models require a chemical kinetics model to close the model, which depends heavily on the type of fuels used in combustion. Because there needs to be a balance between the accuracy of modelling a large number of species and the computational cost of modelling only the important species, a multitude of models exist depending on the intended reactions to analyse. Some studies use previously researched models such as the San Diego mechanism for hydrogen combustion [46], [77], the Z77 mechanism for kerosene and, implicitly, hydrogen combustion [78], sustainable Aircraft Fuel(SAF) based mechanisms [45], [79], among several other publicly available mechanisms. These chemical kinetic mechanisms are often used with software such as Cantera [80] or Chem1D [81] to either interact directly with the combustion model, develop a lookup table for models such as FGM or generate laminar flame results for use in the overall analysis.

One such model recently introduced is the C3MechV3.3 by Dong et al. [82]. This model has been validated against experimental data on hydrogen flames and kerosene flames, yielding significantly accurate results. Additionally, it has been developed to allow for mechanism reductions in order to study specific fuels with reduced computational costs. This mechanism by default has roughly 30000 reactions, with reduced forms for n-heptane fuels with roughly 16000 reactions and further minimal versions for specific fuel types settling for close to 2000 reactions. This is in comparison with smaller mechanisms such as the z77 mechanism with 77 reactions for the same fuel, the HyChem A2 mechanism[83], [84] with 538 reactions and San Diego's mechanism with 30 reactions for hydrogen. The choice of the correct model needs to account for the computational budget of the simulation.

2.2. Synthesis and main hypothesis

Overall, research on the specific behaviour of hydrogen and kerosene fuel blend combustion remains nuanced. It is certain that the replacement of kerosene by hydrogen leads to the reduction of carbon based emissions, including particulates. However, research has also shown that NO$_x$ production does not consistently change with an increase in injected hydrogen, and different studies have achieved different results with different setup cases. It is suggested that, due to the significantly different thermodynamic properties of the two fuels, improper mixing can lead to different OH emissions. Additionally, other factors such as equivalence ratio could have a far more significant impact than just the hydrogen concentration upstream of the flamefront. Current research also points to the significant increase in the consumption speed of the kerosene flame, an increase in the blowout limits of the flame and a decrease in overall flame auto-ignition delay, but points to the possible increase in flame stretch with a higher hydrogen mass blend ratio, however, research of the latter observation has not been conducted for partially premixed flames. Finally, it has been suggested that hydrogen enrichment can lead to a significant increase in combustion efficiency, however, it has been evidently shown that this increase in combustion efficiency is also negated by improper mixing of fuels.

Modelling approaches have been covered in this review in terms of their benefits and drawbacks, as well as their use in academia. For the study of general combustion properties such as ignition-delay, flammability limits and general far field scalar quantities, RANS realizable and RNG $k - \epsilon$ have proved to yield reasonably accurate results compared to experimental data. RANS is typically preferred by academic projects that intend to perform an overview study of a new combustor design or study a wide range of parameters, given the relatively low computational cost of RANS simulations. This approach, however, has the drawback of requiring the modelling of all scales and the use of aggressive simplifications in RANS compatible combustion models (i.e. EDC assumes combustion only at almost perfectly premixed conditions). Alternatively, with a shift into the study of more detailed phenomena from hydrogen addition to kerosene flames, LES models are favoured in their ability to much more accurately capture scalar mixing phenomena, sharp scalar gradients and relevant turbulent scale interactions with the flame fronts. LES also allows for the use of more theoretically accurate combustion models that significantly improve the accuracy of the modelled flame front. For the study of flame characteristics, including the effect of turbulence scales on the flame front, for the study of fuel mixing processes and for a more accurate study of combustion properties previously studied using RANS simulations, the preferred approach by research projects is typically LES.

The review of typical combustion models highlights the need to assess the current simulation case and understand how the choice of a combustion model compromises the analysed data and the overall computational cost. Models such as FGM and EDM could likely be far too simplistic for the detailed analysis of mixing phenomena and flame/flow interactions, and the SAGE mechanism could likely be too expensive. The use of reduced chemical reaction mechanisms allows for the use of more detailed combustion closure models while simultaneously allowing the simulation to stay within the computational budget and achieve reasonably accurate results.

Main hypothesis Since hydrogen has a lower ignition-delay, a much higher diffusion rate and forms flame fronts with a much higher consumption rate compared to kerosene and kerosene flame fronts when reacting with air, it is well recognised that hydrogen flames will typically burn ahead of the kerosene flame when proper fuel mixing is not ensured. The studied literature focuses on modifying the combustor and injector geometry to achieve better fuel mixing upstream of the flame front, however, it is suggested that the mixing quality typically decreases with injected hydrogen mass flow rate as hydrogen concentrates and reacts in additional active reaction zones.

It is hypothesized that, if a hydrogen flame is forced to anchor further downstream by controlling the unburned reactant temperature and consequently reducing its propagation speed, then the additional transport time could allow for a significant amount of additional spatial diffusion of hydrogen, reducing the amount of hydrogen that burns in separate pure hydrogen reaction zones and increasing the amount of hydrogen that mixes properly with kerosene. If this yields true, then the mixing quality is said to increase, and NO$_x$ and CO emissions should decrease.

3

Case setup and Research

3.1. Research Questions

This research aims to study how the process of fuel premixing between hydrogen and vaporized kerosene is altered by changes in inlet temperature. Additionally, this work also aims to explore and understand how the change in inlet temperature affect the flame characteristics and the pollutant emissions and draw observations on whether the resulting changes can be attributed to the changes in fuel mixing, which could pave the way for a novel way to combat some of the limitations of kerosene/hydrogen flames and speed up the development of hydrogen/kerosene powered gas turbines. Finally, with the use of more accurate models to compute the studied solutions, this project also aims to expand and reinforce existing research on the feasibility of hydrogen injection in a jet fuel/air gas combustor and its outcomes. In its exact form, the following main research question is posed:

> *"What is the impact of cooled hydrogen injection on the fuel mixing quality, flame structure and combustor emissions?"*

Additionally, the secondary and additional research questions, in their exact form, are formed from the intended and described objectives for this study:

> *"What is the impact of hydrogen temperature on species and particle distribution over the combustor"*
>
> *"What is the impact of hydrogen temperature on flame stretch and flame front turbulent interactions"*

In this work, the implemented methodology, the execution of the simulations, and the data processing methods should ideally allow these questions to be answered properly.

3.2. Setup Case

For the execution of this project, including understanding and answering the proposed research questions, CFD simulations will be conducted using TUDelft's High Performance Computing (HPC12) Center [85] and the DelftBlue Computational Center [86]. The setup of these simulations is done to closely replicate the combustion environment previously validated experimentally in the Auxiliary Propulsion and Power Unit (APPU) combustor, which influences the choice of the geometry and boundary conditions.

3.2.1. Combustor

The combustion will be simulated in a model replica of the APPU combustor, illustrated in Figure 3.1. This model includes a dual spray nozzle configuration and an injection port for kerosene/air located axially on the combustor that allows for the control of air swirl through the use of a swirler and an axial air injection (AAI) inlet.

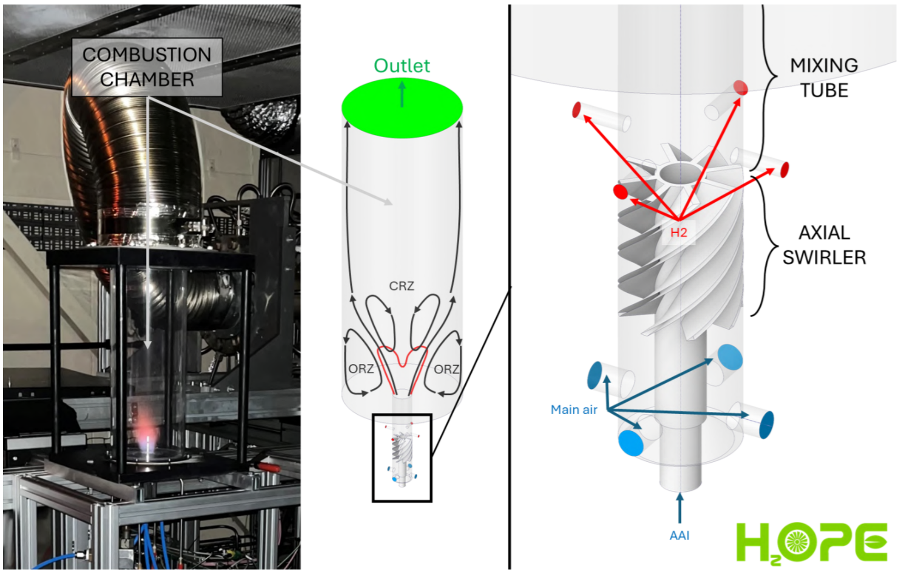

Figure 3.1: APPU Combustor and the isometric view of the model used with labelled boundaries. From [46].

The model domain of the APPU combustor shown in Figure 3.1 is measured to be 500 mm in total height and 148 mm in total width. The main structure can be into an upper combustion chamber and a lower injection port, both mostly cylindrical. The combustion chamber is measured to be 380 mm in height and includes two fuel injectors symmetrically positioned at the bottom face of the combustion chamber and equally spaced from the centreline. The fuel injectors are designed such that the fuel is sprayed in an axisymmetrical, 80 degree vertical cone, and the spray distribution is modelled to replicate the spray cone from the Simplex atomizers by Fluidics Instruments B.V. [87] used in the real APPU combustor. The top cylindrical surface of the combustion chamber is defined as the outlet.

The injection port, characterized by a main tubular section of roughly 24 mm in diameter, includes a total of 9 inlets perpendicular to the main injection tube, 4 5 mm lower ones for air injection, 4 5 mm upper ones for hydrogen injection and one bottom 8 mm inlet for the Axial Air Injection tube (AAI). Between the upper hydrogen and lower air injection inlets, a 30 mm long swirler, characterized by a swirl number of 1.1 [46], introduces a rotational momentum to the air flow from the bottom four air ports before mixing with the hydrogen from the upper four injection ports and with the air injected axially from the AAI port.

3.2.2. Simulation Conditions

A CFD simulation case for this combustor with all relevant modelling approaches is set up using the commercially available CONVERGE CFD software from Convergent Science [88][89] with a non-commercial license. To study the effect of temperature, the $R_h = 20\%$ case from Dave et al. [44], where R_h is the hybrid ratio defined in Equation 3.1 using the enthalpy of reaction of each fuel ΔH_r, is taken, and the temperature of the air and hydrogen inlets are changed to effectively change the temperature of the hydrogen at the exit of the injection tube. Given the issues with fuel mixing that characterize this combustor and the lean conditions of the reference 20% hybrid ratio that place the reaction near its lower flammability limit, two simulations will be done, one one with $T = 250K$ and another with $T = 400K$ hydrogen injection temperature to study this effect without risking pushing the flame to the blowout limits by using near cryogenic temperatures but still leave a significant temperature margin to outline any changes in the studied variables. The relevant parameters that define each of the cases are stated in Table 3.1.

$$R_h = \frac{\Delta H_{r,H_2}}{\Delta H_{r,H_2+C_{12}H_{23}}} \tag{3.1}$$

Table 3.1: Inlet (static) temperature conditions for case A and case B.

Case	$T_{air,inlet}$ $[K]$	$T_{H_2,inlet}$ $[K]$	$T_{C_{12}H_{23},injector}$ $[K]$
A	250	250	300
B	400	400	300

A LES fluid field simulation coupled with combustion and multiphase models is expected to incur several stabilization issues, including possibly not achieving convergence at all. In order to minimize the risk of poor stabilization in iteration cycles, the total simulation workflow will first be divided into a Cold Flow[1] portion and a Combustion/reacting portion. The Cold Flow portion of this workflow will be further divided into a RANS portion and a LES portion of the Cold Flow simulation. The flow rates of each of the reactants for either RANS or LES simulations are summarized in Table 3.2.

Table 3.2: Set-up conditions of the Cold Flow and Combustion simulation cases.

Simulation	R_h $[\%]$	AAI $[\%]$	$\dot{m}_{C_{12}H_{23}}$ $[g/min]$	$\dot{m}_{H_2}$ $[g/min]$	$\dot{m}_{air}$ $[g/min]$
Cold Flow	20	10	0	0.89	444
Combustion	20	10	10	0.89	444

Initially, a RANS Cold Flow simulation will be set up in order to initialize the flow field for the LES Cold Flow simulation and speed up the overall Cold Flow portion of the Cold Flow simulation, as convergence towards statistical steady state is much faster when starting from a previous solution. This initial simulation is also intended to study the flow field of the reactants to understand if there is any issues characteristic to the geometry model before continuing to the more demanding LES simulations. This RANS simulation is run for $\Delta t = 0.2$ s, and the details of the modelling approach are discussed in chapter 4. For both RANS solutions obtained (one for each case), the LES simulations are initialized from the corresponding fluid flow fields. The simulation is run for $\Delta t = 0.15$ s and the Cold Flow modelling approach, including the mesh, chemical mechanism, injection parameters and numerical schemes, is discussed in chapter 4.

The Combustion simulation is initialized from the resulting fluid flow fields obtained from both LES Cold Flow simulations. In order to ignite the flame, a non-reacting spray is initialized for $\Delta t = 5 \cdot 10^{-3} s$ until a spray penetration of roughly 30 mm is obtained, Note that initially the conditions of the spray do not match those stated in Table 3.1 as the spray is first injected at $T = 450$ K and is slowly reduced down to the final static temperature $T = 300$ K as the flame is ignited, developed and anchored. After so, two cylindrical volumetric energy sources are instantiated for $\Delta t = 4 \cdot 10^{-3}$ s, each with a source value of $S = 1 \cdot 10^9$ W/m^3 (with a cell temperature limit of 3000 K) to vaporize the spray and ignite the fuel mixture. The combustion simulation is run for $\Delta t = 0.125\, s$, with flow field solutions recorded at several time checkpoints.

---

[1] Cold Flow simulation is defined in this work as nominal injection of the reactants (except kerosene) without chemistry kinetics modelling

3.3. Theoretical review of relevant combustion phenomena

Due to the existence of a swirler, the overall flame structure is significantly affected. In their work, Palanti et al. [46] simulated a kerosene hydrogen blend combustion in the APPU combustor and identified the existence of an outer recirculation zone between the walls of the combustor and the flames and a toroidal recirculation zone, located roughly in an axial position downstream of the flame and ”pierced” by the axial flow from the injection port. The existence of the swirl also induced a stabilizing effect by reducing the axial component of the velocity and thus the axial pressure drop.

The swirl number of the injected flow has significant impact on how the flame is distributed across the combustor. Previous studies [90], [91] have found that the introduction and increase of swirl number in the incoming flow leads to flame structures that are shorter in length and wider, with reaction zones closer to the injection point and with higher axial temperatures near the reaction zones. Palanti et al. [46] noted additionally that with the addition of hydrogen, due to its low density, the axial to radial velocity component ratio increases, leading to lower swirl numbers and potentially to longer flames. However, it is not straightforward to pin point the change of flame structure to the swirl number as Dave et al. [44] noted in his experimental work on the APPU combustor that the increase in hydrogen to fuel ratio lead to shorter and wider flames. Furthermore, in the same work, significant differences were found between pure kerosene and hydrogen enriched kerosene flames. Whilst in pure kerosene flames, the flame structure resembled 2 well structured and well contained reaction zone lobes were contained, hydrogen enriched flames structures are characterized by a distribution of primary and (less intense) secondary reaction zones that result from the changes in fuel distribution in the combustor.

It is known then that the flame structures in the combustor and the subsequent recirculation zones are affected by the existence of the swirl and how intense it is. Furthermore, in the characterization of the flame, the terms ”primary reaction zone” and ”secondary reaction zones” can be used to identify the most intense reaction zones anchored close to the kerosene injector and the secondary less intense reaction zones that are chaotic in time as previously studied, respectively. Due to the poor mixing in the combustor, the flame is often described as highly diffusive or partially premixed, with significant reaction zones of either flame regime.

4

Methodology of fluid flow field modelling

In this section, the methodology behind the modelling of fluid flow field and the setup of the simulation before any combustion modelling is properly defined. The relevant models and their impact on the solution are explored, and the modelling assumptions are properly highlighted.

4.1. Grid mesh

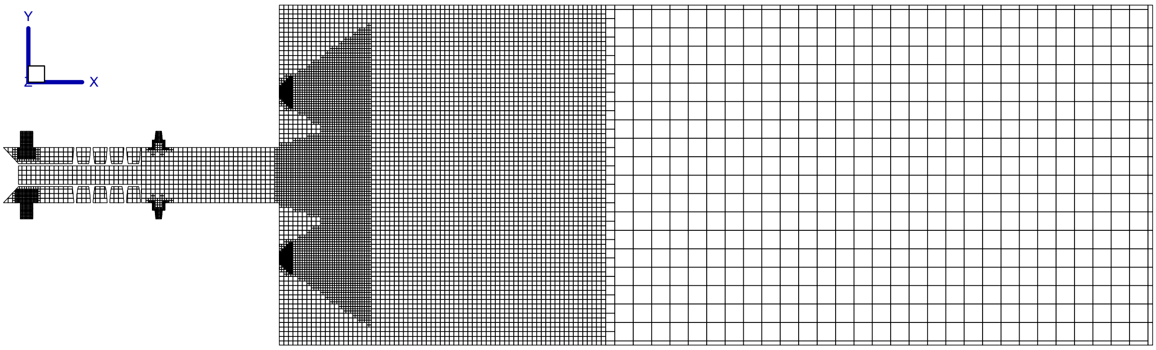

Figure 4.1: Domain and base mesh (without AMR cells) used for the LES simulations.

The mesh for this work is created at runtime by the CONVERGE program using a cut-cell Cartesian grid generation method [88], which allows the software to wrap an orthogonal hexahedral mesh around a complex geometry and cut the cells that intersect the surface of the geometry such that the interior cell structure remains almost entirely unskewed, which is beneficial for good spatial discretization. In order to avoid cut cells with a fractional volume and poor skewness compared to neighbouring cells, the grid generation algorithm will merge wall cells with neighbouring cells when a certain volume ratio is lower than the limit user defined value, which in this work is defined as 1.1. The mesh is generated at runtime and, if AMR is used, is regenerated every n cycles according to the defined criterion.

For both LES simulations, a structured hexahedral mesh is created with cells of $64\,\text{mm}^3$ ($dx = 8\,\text{mm}$) all throughout, a mesh size chosen to save on computational time for the less relevant flow field modelling ahead of the flame. From experimental data, the high temperature, high reaction rate areas are expected to occupy less than roughly a third of the total, which is used to define a second mesh refinement zone from the bottom of the injection tube up until this defined height with cells of $8\,\text{mm}^3$ ($dx = 2\,\text{mm}$), refereed to as main refinement block. This choice in modelling means that diffusion and mixing ahead of this main refinement block are grossly overestimated, and the flow field is aggressively smoothed. This effect is mainly due to the introduction of significant numerical diffusion when the grid is too coarse or when the grid size changes significantly over short distances, due to the growth of truncation error in the spatial discretization scheme used. This is an issue if there is an interest in accurately solving for flow momentum and energy past this main refinement block as the respective diffusive gradients will not be solved correctly, however since the height of this refinement block should allow for the flow to cool down enough for the species to not react significantly past the finely refined mesh and since the flow dynamics are not of interest past this point, the impact on the simulation results should be minimal. The practical consequences of modelling the combustion chamber in this manner are the increased rate of mixing between species past $x = 0.15\,m$ and the increase of flow homogeneity.

To model the spray cones in combustion simulations, accurate grid refinement is critical for determining correct spray/vapour penetration and spread. Depending on the size of parcels, the momentum transferred from the Lagrangian parcels to the Eulerian fields can be diffused over a coarser grid, which will lead to the overestimation of particle drag and underestimation of particle/vapor penetration (the inverse will happen on a finer than needed mesh) [92]. Previous studies on LES spray modelling [93] have shown that reasonable convergence for diesel spray/vapour penetration and spray spread is typically obtained for cell sizes close to $0.00195\,\text{mm}^3$ ($dx = 0.125\,\text{mm}$). Modelling the entire spray and vapour plume using this level of grid refinement is not only prohibitively expensive but would also likely directly affect the flame front as the mesh algorithm implemented by CONVERGE does not control smooth cell volume increase between refinement blocks, leading to steep changes in neighbouring cell sizes between the nozzle refinement block and the surrounding main refinement block, introducing strong numerical diffusion on the edges of this cone. Instead, only a small section up to $5\,\text{mm}$ ahead of the injector (50 injector diameters) is refined to this level, a mesh refinement strategy adopted and validated by several studies on fuel spray injection modelling [93][94][95]. To model the particles further away from the spray, the choice of refining the mesh using a cone block of cell size $1\,\text{mm}^3$ ($dx = 1\,\text{mm}$, roughly 50 nozzle diameters) is made in order to minimize the effect of droplet drag overestimation with minimal added cell cost. The resulting mesh is represented in Figure 4.1.

On top of the static mesh, an Automatic Mesh Refinement (AMR) algorithm is used to ensure accurate modelling of other pertinent flow features. CONVERGE allows for spatial refinement of the mesh at runtime using either a scalar value threshold or its sub grid scale value (in the case of LES). For a given scalar, CONVERGE defines the sub-grid scale in the same way as in the LES integration, that is the difference between the actual field and the resolved field, however for the AMR algorithm, the sub-grid scale is estimated based on a truncated form of an infinite series [88][96], show in Equation 4.1 for an arbitrary variable ϕ in each cardinal direction k of a rectangular cell. In LES, using AMR to refine areas according to a threshold can be seen in practice as better resolving smaller scales in areas where turbulent mixing and diffusion are expected to be more relevant, which further explains the choices made for the AMR thresholds.

$$\phi_{SGS} = -\sum_{k} \frac{dx_i}{24} \frac{\partial^2 \phi}{\partial x_i^2} \tag{4.1}$$

In the region of the injection tube, the AMR algorithm acts to refine areas where the velocity SGS value exceeds $0.5\,\text{m/s}$, and areas where the hydrogen mass fraction exceeds 2%, the latter threshold is used as a way to dynamically refine the interface between the low velocity hydrogen flow and the high velocity air flow near the hydrogen port interface with the injection port, ensuring better prediction of relevant mixing phenomena between these quantities. In the combustion chamber region, the AMR algorithm refines areas where the temperature SGS exceeds $5\,\text{K}$ and where the Thickened Flame Model sensor variable S exceeds 0.85, in an attempt to correctly capture thermal diffusive fluxes and turbulent structures in high temperature regions and around the flame front, respectively. Additionally, due to the way the Thickened Flame Model sensor is implemented, the hydrogen flame front is not properly captured or refined (In chapter 5, a breakdown of this issue is explored). In an attempt to reduce the error from the lack of proper refinement around hydrogen flames, the AMR algorithm is used to refine areas where the hydrogen mass fraction exceeds 0.2%, which should allow the algorithm to capture the turbulent scales better before and close to any flame front anchored near the injection tube that is relatively richer in hydrogen compared to the main kerosene flame structures. Finally, in order to correctly model the wall profile, the y^+ was chosen to be kept at roughly $y^+ = 25$, and AMR is used to refine all the walls in the injection tube such that this value is maintained for each near wall cell.

Note that for the size of this domain, the number of cells used by the AMR algorithm to fulfil these requirements are estimated to be around 20 M cells, which exceeds the computational budget assigned to this work. In order to work around this limitation, the AMR algorithm is not allowed to exceed 10 M cells, loosening the aforementioned threshold criteria to reduce the number of cells refined, which means that on average, the simulation is run with 10 M cells. The cell refinement is validated using the Pope [62] criterion.

For the RANS simulations, a structured hexahedral mesh is created with cells of 3375 mm^3 ($dx = 15$ mm) and AMR is used to model both the injection tube and the combustion chamber with a velocity SGS threshold of 0.5 m/s and a hydrogen mass fraction threshold of 2%. Note that the aforementioned wall y^+ based refinement and nozzle refinement blocks are not included in this simulation.

4.2. Boundary conditions

The numerical domain is delimited by one outlet, six inlets and seven walls. The outlet is defined with a Dirichlet condition for static pressure set to 1 atm and a Neumann condition for velocity, with zero gradient, for both inflow and backflow. The walls of the combustion chamber are all defined as isothermal, smooth walls with a law-of-the-wall condition for both velocity and temperature. The temperature of the walls is fixed at 300 K. For the injection port, the same conditions apply except the temperature is fixed at the temperature of the injected air, defined for both cases in Table 3.1. The inlets are defined with a Neumann condition for pressure set to zero gradient and Dirichlet conditions for mass flow and temperature defined according to each case by Table 3.1 and Table 3.2. In order to simulate the species at the inlet, the air inlets are defined with $Y_{O_2} = 0.767$ and $Y_{N_2} = 0.233$ and the hydrogen inlets are defined with $Y_{H_2} = 1$. The backflow at the outlet of the combustor is defined using the same species composition as the air inlets.

4.3. Fluid flow field modelling

The fluid flow field of a Newtonian fluid simulation can be described through the general Navier-Stokes equations for a Cartesian frame of reference (Equation 4.2 through Equation 4.6) and the equation of state for pressure-temperature-density coupling (Equation 4.7). The Mass and Momentum transport equations are fundamental but not sufficient for the modelling of combustion processes, which require the energy transport equations and the species transport equations for each species m. Some of the other mathematical relations pertaining to additional models are discussed in separate sections of this work.

$$\text{Mass transport}: \frac{\partial \rho}{\partial t} + \frac{\partial (\rho u_i)}{\partial x_i} = 0 \tag{4.2}$$

$$\text{Momentum transport}: \rho \left(\frac{\partial u_i}{\partial t} + u_j \frac{\partial u_i}{\partial x_i} \right) = -\frac{\partial p}{\partial x_i} + \frac{\partial \tau_{ij}}{\partial x_i} + \rho \sum_{m=1}^{M} Y_m f_{m,i} \tag{4.3}$$

$$\text{Energy transport}: \rho \left(\frac{\partial e}{\partial t} + u_j \frac{\partial e}{\partial x_i} \right) = -\frac{\partial q_i}{\partial x_i} - p \frac{\partial u_i}{\partial x_i} + \boldsymbol{\tau_{ij}} \frac{\partial u_i}{\partial x_j} \tag{4.4}$$

$$+ \frac{\partial}{\partial x_i} \left(\rho \sum_{m=1}^{M} D_m h_m \frac{\partial Y_m}{\partial x_i} \right) + S \tag{4.5}$$

$$\text{Species transport}: \rho \left(\frac{\partial Y_m}{\partial t} + u_j \frac{\partial Y_m}{\partial x_i} \right) = \frac{\partial}{\partial x_j} \left(\rho D_m \frac{\partial Y_m}{\partial x_i} \right) + \dot{\omega}_m \tag{4.6}$$

$$\text{Equation of state}: P = \frac{\rho R T}{M} \tag{4.7}$$

The Navier-Stokes (NS) equations remain analytically unsolved and thus need to be discretized and solved iteratively. Since the solver interpolates between computational grid points to approximate the continuous flow field, which is defined on the implemented computational mesh and thus does not contain exact flow field information at every geometric position, the mesh must be refined sufficiently to capture all turbulent scales. This means, however, that the mesh must be refined down to at least the Kolmogorov scale, defined as the scale of the smallest turbulent structure in the entire domain. This logic makes DNS cost, measured in the product of the number of grid points N_{GP} and the number of iteration $N_{iterations}$ scale exceedingly rapidly with Re^3 (Equation 4.8), and for a typical gas turbine combustor this type of scale could imply having to solve this equation iteratively for billions of grid points, far exceeding the budget of current most expensive CFD computations [60].

$$N_{GP} \cdot N_{iterations} \sim Re^3 \tag{4.8}$$

This project makes use of model and mesh adaptivity strategies [97], which refer to modifications of the governing equations and modifications of the mesh, respectively, in order to reduce the error of a solution that is obtained with a coarser mesh compared to a DNS mesh.

4.3.1. RANS modelling of fluid flow field

The Reynolds Averaged Navier-Stokes modelling approach to fluid field modelling is a model adaptivity strategy that reduces the requirement of mesh refinement by expressing the flow field as a sum of an ensemble averaged term $\bar{u}$ and a fluctuating term u':

$$u = \bar{u} + u' \tag{4.9}$$

It is important to note that since this flow is to be modelled as a compressible flow, ρ varies spatially and in time, resulting in additional terms that need to be modelled [98]. To avoid modelling these additional terms on every equation, the Favre averaging method is used to average the NS equations, resulting in $\tilde{X}$ terms obtained through Equation 4.20.

$$\tilde{X} = \frac{\bar{\rho}\bar{X}}{\bar{\rho}} \tag{4.10}$$

The Navier-Stokes equations are then averaged in order to separate the average field quantities from the fluctuating quantities, leading to Equation 4.11 through Equation 4.15. Note that in the deduction of these equations, the relation $\overline{u_i u_j} = \bar{u}_i \bar{u}_j + \overline{u_i' u_j'}$ is used.

$$\text{Mass transport : } \frac{\partial\bar{\rho}}{\partial t} + \frac{\partial(\bar{\rho}\tilde{u}_i)}{\partial x_i} = 0 \tag{4.11}$$

$$\text{Momentum transport : } \bar{\rho}\left(\frac{\partial\tilde{u}_i}{\partial t} + \frac{\partial\,\tilde{u}_j\tilde{u}_i}{\partial x_i}\right) = -\frac{\partial\bar{p}}{\partial x_i} + \frac{\partial\bar{\tau}_{ij}}{\partial x_i} - \frac{\partial}{\partial x_i}\left(\bar{\rho}\widetilde{u_i' u_j'}\right) + \bar{\rho}\sum_{m=1}^{M}\widetilde{Y_m f_{m,i}} \tag{4.12}$$

$$\text{Energy transport : } \bar{\rho}\left(\frac{\partial\tilde{e}}{\partial t} + \tilde{u}_j\frac{\partial\tilde{e}}{\partial x_i}\right) = -\frac{\partial\bar{q}_i}{\partial x_i} - \frac{\partial}{\partial x_i}\left(\bar{\rho}\widetilde{e' u_i'}\right) - \bar{p}\frac{\partial\tilde{u}_i}{\partial x_i} + \bar{\boldsymbol{\tau}}_{ij}\frac{\partial\tilde{u}_i}{\partial x_j} \tag{4.13}$$

$$+\frac{\partial}{\partial x_i}\left(\bar{\rho}\sum_{m=1}^{M}\widetilde{D_m h_m\frac{\partial Y_m}{\partial x_i}}\right) + \bar{S} \tag{4.14}$$

$$\text{Species transport : } \bar{\rho}\left(\frac{\partial\tilde{Y}_m}{\partial t} + \tilde{u}_j\frac{\partial\tilde{Y}_m}{\partial x_i}\right) = \frac{\partial}{\partial x_j}\bar{\rho}\left(\widetilde{D_m\frac{\partial Y_m}{\partial x_i}}\right) - \frac{\partial}{\partial x_i}\left(\bar{\rho}\widetilde{Y_m' u_i'}\right) + \bar{\dot{\omega}}_m \tag{4.15}$$

$$\text{Equation of state : } \bar{P} = \frac{\bar{\rho}R\bar{T}}{\bar{M}} \tag{4.16}$$

It is important to understand the shift from the original Navier-Stokes to the Averaged Navier-Stokes equations as the additional terms that originated from the fluctuating terms, that is the Reynolds stress tensor $\tau_{ij} = -\left(\bar{\rho}\widetilde{u_i' u_j'}\right)$ and the Reynolds fluxes $-\left(\bar{\rho}\widetilde{e' u_i'}\right)$ and $-\left(\bar{\rho}\widetilde{Y_m' u_i'}\right)$, make this model unclosed. These terms are often treated as turbulent diffusion terms and consequently solved with gradient models, which themselves remain unclosed but can be closed with physical descriptions of the diffusion of each of the scalars transported (i.e. Fick's law) [97], [98].

4.3.2. Model Closure/Reynolds stress tensor modelling

In order to model the unclosed Reynolds stress term, the Realizable k-ϵ model as implemented in CONVERGE CFD [88] is used. The base k-ϵ model is part of the Eddy Diffusion models [98] which use the Boussinesq assumption to model the deviator part of the Reynolds stress tensor τ_{ij}' as being proportional to the eddy viscosity ν_t as seen in Equation 4.17.

$$\tau_{ij}' \approx 2\nu_t S_{ij} - \frac{2}{3}\delta_{ij}k \tag{4.17}$$

Where $S_{i,j}$ is the strain tensor, δ_{ij} is the Kronecker delta and k is the specific turbulent kinetic energy. Replacing Equation 4.17 in the averaged Navier-Stokes reduces the number of unknown independent variables from the Reynolds Stress tensor term down to just one independent variable, the Eddy Viscosity ν_t. The k-ϵ model attempts to compute the value of ν_t by introducing transport equations for the turbulent kinetic energy k and for the dissipation rate ϵ, which can be used to compute the ν_t in the Eddy Dissipation Concept as seen in Equation 4.18. By setting other independent variables as constants for most general cases, such as C_D (typically set at 0.09), the turbulence model is fully closed.

$$\nu_t = C_D\frac{k^2}{\epsilon} \tag{4.18}$$

4.3.3. LES modelling of fluid flow field

The Large Eddy simulation modelling approach to fluid field modelling is a model adaptivity strategy that aims to reduce the size of the required mesh by partially modelling turbulent scales. The model is supported by the energy cascade theory [98], which states eddy energy predominately follows a main path from creation to dissipation, that is the predominately energy is transferred from large scale turbulent structures (high energy) to small scale turbulent structures (low energy) before inevitability dissipating the small enough scale turbulent scales, as lustrated in Figure 4.2. It is important to note that this is an approximation as energy can dissipate at any scale, however, it can be approximated that scales of turbulent structures in the ”inertial range” only transfer the eddy energy.

It is also important to note that the turbulent scales associated with energy production and transfer are mostly anisotropic, have relatively larger timescales and are normally a product of the geometry and boundary conditions, which makes finding a model to accurately and universally capture these scales quite hard. In contrast, the smaller scales associated with energy dissipation are mostly isotropic, have shorter timescales and are normally a product of the large scale turbulent structures by the energy cascade phenomena discussed previously, making them far easier to model if the information on large scales is available. Additionally, it can also be argued that smaller scales consistently dissipate according to their rate of turbulent energy dissipation and kinematic viscosity, independently of any other problem variables, allowing for the abstract modelling of these scales [98].

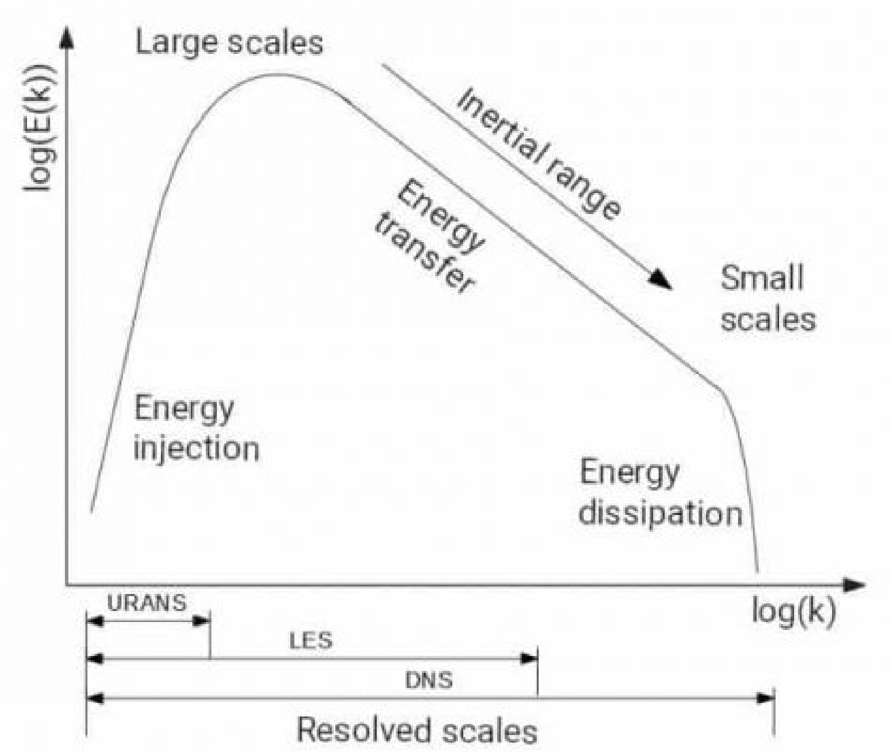

Figure 4.2: Illustration of the energy distribution by turbulent scales, as well as ranges of resolved scales for each type of model. Sourced from [99].

The LES model framework draws from these concepts to resolve only large scale structures in the inertial range, leaving the smaller scales to be modelled by eddy diffusion, effectively increasing the smallest cell size to the size of the lowest turbulent scale in the inertial range. In order to do so, the Navier-Stokes equations (Equation 4.2 through Equation 4.6) are filtered using a filter width $\bar{\Delta}$[1] that roughly defines the separation between the inertial scales to be resolved and the sub grid scales (SGS) to be modelled, which is implemented as a function of the local cell size. It is then important to note that the mesh should not be too coarse, as this can lead to over-filtering of scales and over-estimating

---

[1] The LES $\bar{\phi}$ is not the same as the RANS $\bar{\phi}$ and as such these notations should be treated differently according to each section.

turbulent kinetic energy dissipation. This observation also applies to when the mesh is too fine, where the dissipation is underestimated, however, the error in this case tends to shrink with the reduction in cell size. The filtering allows the flow field to be described as a sum of a resolved component $\bar{u}_i$ and a filtered out SGS component $u_{i,SGS}$ as described in Equation 4.19. The filtering of 3 or more multiplied variables also requires further attention that will not be covered in this explanation.

$$u_i = \bar{u}_i + u_{i,SGS} \leftrightarrow \bar{u}_i = u_i - u_{i,SGS} \tag{4.19}$$

Note that similarly to the RANS formulation, due to how ρ varies in space and time, filtering the LES equations will lead to far more additional terms to be modelled, and to solve this issue, the Favre Filtering is used to filter the NS equations, giving the Favre filtered $\tilde{X}$ terms obtained by Equation 4.20.

$$\tilde{X} = \frac{\bar{\rho}\bar{X}}{\bar{\rho}} \tag{4.20}$$

The Navier-Stokes are then filtered in such a way to solve only for the scales that were retained after the Favre filtering process, yielding Equation 4.21 through Equation 4.25. Note that in these deductions, the relation $\nabla \cdot (\overline{XX}) = \nabla \cdot (\bar{X}\bar{X}) + \nabla \cdot (\overline{XX} - \bar{X}\bar{X})$ is used.

$$\text{Mass transport} : \frac{\partial \bar{\rho}}{\partial t} + \frac{\partial (\bar{\rho}\tilde{u}_i)}{\partial x_i} = 0 \tag{4.21}$$

$$\text{Momentum transport} : \bar{\rho}\left(\frac{\partial \tilde{u}_i}{\partial t} + \frac{\partial\, \tilde{u}_j \tilde{u}_i}{\partial x_i}\right) = -\frac{\partial \bar{p}}{\partial x_i} + \frac{\partial \bar{\tau}_{ij}}{\partial x_i} - \frac{\partial \boldsymbol{\tau}_{ij,SGS}}{\partial x_i} + \bar{\rho} \sum_{m=1}^{M} \widetilde{Y_m f_{m,i}} \tag{4.22}$$

$$\text{Energy transport} : \bar{\rho}\left(\frac{\partial \tilde{e}}{\partial t} + \tilde{u_j}\frac{\partial \tilde{e}}{\partial x_i}\right) = -\frac{\partial \bar{q_i}}{\partial x_i} - \frac{\partial}{\partial x_i}\left(\bar{\rho}\widetilde{u_i e} - \bar{\rho}\tilde{u}_i\tilde{e}\right) - \bar{p}\frac{\partial \tilde{u}_i}{\partial x_i} + \bar{\boldsymbol{\tau}}_{ij}\frac{\partial \tilde{u}_i}{\partial x_j} \tag{4.23}$$

$$+ \frac{\partial}{\partial x_i}\left(\bar{\rho}\sum_{m=1}^{M} \widetilde{D_m h_m \frac{\partial Y_m}{\partial x_i}}\right) + \bar{S} \tag{4.24}$$

$$\text{Species transport} : \bar{\rho}\left(\frac{\partial \tilde{Y}_m}{\partial t} + \tilde{u_j}\frac{\partial \tilde{Y}_m}{\partial x_i}\right) = \frac{\partial}{\partial x_j}\bar{\rho}\left(\widetilde{D_m \frac{\partial Y_m}{\partial x_i}}\right) - \frac{\partial}{\partial x_i}\left(\bar{\rho}\widetilde{u_i Y_m} - \bar{\rho}\tilde{u}_i\tilde{Y_m}\right) + \bar{\dot{\omega}}_m \tag{4.25}$$

$$\text{Equation of state} : \bar{P} = \frac{\bar{\rho}R\tilde{T}}{\tilde{M}} \tag{4.26}$$

The workout of the filtered Navier-Stokes equations is necessary to understand the equations implemented in the following models discussed in this report. It is also important to understand why using this model adaptivity strategy leaves the LES model unclosed, that is, there are SGS specific terms that cannot be solved and need to be modelled in some way [97]. The most relevant and complicated one to model is the SGS stress tensor $\tau_{SGS} = \bar{\rho}(\tilde{u}_j\tilde{u}_i - \widetilde{u_j u_i})$, which requires specific SGS models to be closed. Other terms such as $-(\bar{\rho}\widetilde{u_i e} - \bar{\rho}\tilde{u}_i\tilde{e})$ and $-(\bar{\rho}\widetilde{u_i Y_m} - \bar{\rho}\tilde{u}_i\tilde{Y_m})$, identified as species and energy fluxes respectively, are also unclosed and need to be modelled accordingly.

4.3.4. Model Closure/SGS turbulence modelling

The τ_{SGS} term can be interpreted as a combination of the Leonard stress tensor L_{ij} (representing the effects from larger resolved scales), the Cross Stress Tensor C_{ij} (representing the effects from interactions between SGS and resolved scales) and the LES Reynolds Stress Tensor R_{ij} (representing the effects of momentum transfer between SGS scales), as seen in Equation 4.27. While the Leonard stress tensor term can be computed exactly, the other terms depend on the non-reconstructable SGS scales and thus need to be modelled.

$$\tau_{SGS} = L_{ij} + C_{ij} + R_{ij} \tag{4.27}$$

Typical research projects in kerosene, hydrogen and air combustion suggest that the Smagorinsky-Lilly's SGS model and the dynamic Smagorinsky-Lilly's SGS model seem to be well suited for typical combustion simulations [69], [100]. Since neither model computes for the transport of any quantity, these are some of the least resource intensive models that can be used for LES. Models that solve for the transported kinetic turbulence energy such as dynamic structural [88], [101] could theoretically be more accurate, however these are more resource intensive and previous studies have found that the difference between zero equation and one equation models[2] is negligible [102]. The choice of SGS turbulence models seems to have a significantly smaller impact on the final solution compared to turbulent combustion closure models, however, this depends on the models chosen, as the EDC will model the chemical reaction rate (at subgrid scale) based on the turbulent mixing and dissipation rate, requiring correct modelling of this quantity [103].

In this work, in order to model τ_{SGS} term, a modification of the original Smagorinsky [104] model called Dynamic Smagorinsky-Lilly model is used according to the implementation used in CONVERGE CFD [88]. The original Smagorinsky model is a zero equation model that uses the Boussinessq hypothesis to assume that the effects of R_{ij} can be taken as proportional to the local rate of strain of the resolved turbulent scales [98] $\bar{S}_{ij} = \frac{1}{2}\left(\frac{\partial \bar{u}_i}{\partial x_j} + \frac{\partial \bar{u}_j}{\partial x_i}\right)$. Although only R_{ij} is modelled, later reviews of this method have found that the effects of the other terms also end up being computed by this approximation. The final formula for the unclosed term is given by Equation 4.28, where $\tau_{isotropic}$ is the trace of τ_{ij} and $\tau_{deviatoric}$, modelled by Smagorinsky, is the trace free version of τ_{ij}.

$$\tau_{SGS} = \tau_{isotropic} + \tau_{deviatoric} \approx \frac{1}{3}\tau_{kk}\delta_{ij} - 2C_2^2\Delta^2\sqrt{S_{ij}S_{ij}}\bar{S}_{ij} \tag{4.28}$$

The C_s constant is in fact not constant on a case by case bias and needs to be carefully chosen for each specific condition, normally requiring experimental data of similar cases to obtain a ballpark value for this term. It's possible to compute C_s in space and time ($C_s(x,t)$ by first defining a second larger test filter of width $\check{\Delta} > \bar{\Delta}$ (typically $\check{\Delta} \approx 2\bar{\Delta}$) and then using the information on the resolved scales captured by $\check{\Delta}$, which are assumed to behave similarly to the SGS scales (can be modelled in a similar way according to Equation 4.28), to compute a value for $C_s(x,t)$. Note that the test filtered scales can still be interpreted as a combination of the terms in Equation 4.27, except the SGS scales are now just the scales smaller than $\check{\Delta}$. The Germano Identity is used to relate the stress tensors of both sensors to the filtered Leonard stress tensor $\check{L}_{ij}$ as described in Equation 4.29.

$$\tau_{SGS} = \check{\tau}_{SGS} - \check{L}_{ij} \qquad\qquad \check{L}_{ij} = \check{\overline{u_i u_j}} - \check{\bar{u}}_i\check{\bar{u}}_j \tag{4.29}$$

The optimization problem can then be formed by replacing the relations for both stress tensors in the Germano identity and assuming spatial variations of C_s can be neglected. This formulation leads to an overdetermined system of equations that must be solved using error minimization. The Lilly's Least squares error minimization technique can be used to obtain a solution for $C_s(x,t)$ from the system of equations.

This choice of the dynamic Smagorinsky model reflects the general success shown in correctly modelling the bidirectional scale energy transfer between modelled and resolved scales. In their review, Pope [61] outlined that even when the notion of scale similarity does not accurately describe the sub grid physics, the use of the dynamic Smagorinsky model can still provide a good approximation to the $C_s(x,t)$. For this work, this model's robustness is highly valued and relevant in order to model a combustion for which there is not enough data to model this coefficient any other way.

---

[2] zero equation models do not require any additional transported quantities to be solved, n equation models solve n additional transport equations.

4.3.5. Wall model

The model from Werner and Wengle [105], recommended for use in typical LES simulations[88], is used to preserve the necessary accuracy on the injector tube walls whilst also reducing the cell count. The model simplifies the standard law of the wall's logarithm profile down to a power law profile in order to eliminate the need for an iterative solver, resulting in the simplified description of the boundary layer shown in Equation 4.30.

$$\begin{cases} u^+ = z^+ & \text{if} \quad y^+ \leq 11.81 \\ u^+ = 8.3 \cdot (z^+)^{\frac{1}{7}} & \text{if} \quad y^+ > 11.81 \end{cases} \tag{4.30}$$

The wall profile is also simplified by neglecting the buffer layer, defining the viscous sublayer from the wall up to $y^+ = 11.81$. Knowing that the shear velocity u^*, the non dimensional wall velocity u^+ and the non dimensional wall distance y^+ can be given by Equation 4.31 through Equation 4.33, the boundary layer velocity profile equation defined by Werner and Wengler can be manipulated to solve for u^*, and consequently the wall shear stress, resulting in the final equation given by Equation 4.34 as implemented in CONVERGE CFD [88].

$$u^* = \sqrt{\frac{\tau_w}{\rho}} \tag{4.31}$$

$$u^+ = \frac{u}{u^*} \tag{4.32}$$

$$y^* = \frac{y \rho u^*}{\mu} \tag{4.33}$$

$$u^* = \begin{cases} \sqrt{\left[\frac{1-B}{2} A^{\frac{1+B}{1-B}} \left(\frac{\mu}{\rho y}\right)^{1+B} + \frac{1+B}{A} \left(\frac{\mu}{\rho y}\right)^{B} |U_{i,\mathrm{tang}}|\right]^{\frac{2}{1+B}}} & \text{if} \quad |U_{i,\mathrm{tang}}| \leq \frac{\mu}{2\rho y} A^{\frac{2}{1-B}} \\ \sqrt{\frac{\mu |U_{i,\mathrm{tang}}|}{\rho y}} & \text{if} \quad |U_{i,\mathrm{tang}}| > \frac{\mu}{2\rho y} A^{\frac{2}{1-B}} \end{cases} \tag{4.34}$$

The choice of this wall model in particular reflects the intent of reducing the computational cost of the near wall computations, since the choice of a law of the wall model in CONVERGE CFD requires an additional set of iterations for each time step, which is bypassed by the use of an exponential profile in the Werner and Wengle model. The model also shows reasonably accurate prediction of friction factor against more detailed models [106] and of boundary layer profiles when the wall grid y^+ is refined within $25 < y^+ < 40$ and for a sufficiently high Re [107]. A *a posteri* analysis is made to ensure that the Re is within the typical ranges validated for this model, that is $Re \sim \mathcal{O}(10^4) - \mathcal{O}(10^5)$. Following previous studies on this model [107], it is chosen to set $y^+ = 25$ in order to reduce the error in viscous sublayer thickness estimation.

4.4. Multiphase Modelling

The LES combustion setup requires modelling of jet fuel particles to accurately capture spray penetration and droplet evaporation. The parcels injected are expected to behave as a dilute spray for an overwhelming majority of the spray cone, with the exception of the limit near the injection point, which means the particles can be considered not to collide with each other. Based on previous similar studies [46] and on reviews of dilute spray modelling studies [108] and other reviews on particle modelling techniques [65], the Discrete Phase Modelling (DPM) approach was implemented.

The DPM approach uses the Lagrangian frame of reference to model each particle's property according to its current state (position, velocity, temperature,...) and time, as opposed to the Eulerian frame of reference that models a flow volume according to the changes in flow properties (pressure, velocity, temperature,...) in pre-positioned points in space and time. This change in reference allows for the solver to compute the exact particle position and trajectory in space, where the motion of each particle is deduced from Newton's second law, yielding Equation 4.35 for each parcel p and each cardinal direction i.

In CONVERGE [88], the Lagrangian solver solves for a group of particles called parcels, instead of each particle. Parcels are composed of packed particles with identical properties (velocity, temperature, etc.) and are used to statistically describe a cloud of particles, rather than modelling every individual particle, thereby enabling efficient modelling of sprays. The changes in material properties of the parcels are balanced against the changes in flow properties in the Eulerian solver with the addition of source and dissipation terms to the Filtered Navier-stokes transport equations (Equation 4.21 to Equation 4.25), which allows for the correct interaction between gas field and liquid particulates for the correct prediction of spray penetration and particle evaporation modelling.

$$\text{Parcel motion: } \rho_p V_p \frac{dv_i}{dt} = F_{p,i} \tag{4.35}$$

$$\text{Forces: } F_{p,i} = F_{drag,i} + F_{gravity,i} = C_D \pi r_p^2 \frac{\rho_p |u_{r,i}|}{2} + \rho_p V_p g_i \tag{4.36}$$

Where V_p is the parcel volume, $F_{p,i}$ is any force applied on the parcel, C_D is the drag coefficient, r_p is the parcel radius and $u_{r,i}$ is the parcel velocity in the cardinal direction i. Each parcel is modelled as a 0D system, which means that the equations for the energy of the entire parcel are described by the first law of thermodynamics without the need to model the heat transfer inside the parcel. The heat transfer at the interface of each parcel, however, needs to be modelled using heat convection models. Similarly, since there's just one species and the density of the particle is constant inside the parcel, the change in species (and total) mass is only evaluated according to changes in total parcel volume and known overall material properties. In Equation 4.35, the motion of liquid particles is influenced by the forces applied to each parcel, which is given by a combination of gravitational forces and drag forces Equation 4.36. Note that the simulation does not include any gravitational acceleration for either Eulerian or Lagrangian fields, that drag forces are computed in terms of the parcel properties and that $u_{r,i}$ is the parcel-fluid relative velocity in the flow direction i.

4.4.1. Particle interaction models

Relevant fluid-particle and particle-particle phenomena, such as particle evaporation, particle breakup, and particle coalescence, among other phenomena, need to be evaluated according to their relevance towards achieving the research goals. For the breakup process, it is important to distinguish between the primary breakup of droplets from a liquid sheet and the secondary breakup between droplets, the latter of which is characteristic of atomization. The primary breakup of particles is rarely modelled, with authors often choosing to define the droplet distribution directly at the injector. Palanti et al. [46] used a Stochastic Secondary Droplet (SSD) model for the secondary breakup mechanism, and the model from [109] for the evaporation of droplets. One other study [110] modelled the evaporation using the Frossling correlation from [111] and argued that the secondary breakup was irrelevant considering the Weber number of the injected liquid. Additionally, both studies have opted to simplify the spray simulation and model the spray at the injector outlet with a Rosin-Rammler distribution instead of solving for the injection process, in which case the particle data must be obtained from the most appropriate literature case. CONVERGE also offers the option to model both these regimes using a coupling between the Kelvin-Helmholtz and the Reyleigh-Taylor surface instability model, which has also used previously in kerosene sprays [76]. Palanti et al. [46] modelled the injection and evaporation of kerosene droplets and consequent combustion of kerosene with gaseous hydrogen injection and underlined the importance of droplet wall interaction towards the simulation

In this work, the collision between parcels is considered negligible, and a rebound/slide model is used to model particles that collide with the walls of the combustor. Both choices are made because the impact of modelling either phenomenon on the actual spray and, consequently, on combustion is negligible, since very few particles will collide with each other or with the wall. The former choice is consistent with a collection of studies on dilute sprays [108], however, similar studies often differ in choice of wall modelling, with some modelling wall film formation [46] and other studies choosing to use a rebound/slide model[110]. It is acknowledged that there predictably could be the formation of wall film near areas such as outer recirculation zones, however, it is assumed that, the simulation time of $\Delta t = 0.125\,\text{s}$ should not allow for formation of a significant wall film surface and that the particle collisions with the walls happen so irregularly in this time frame that the slide/rebound model should appropriately model the interaction.

The evaporation of the particles is modelled using a Frossling correlation as introduced by Amsden et al. [111] and implemented by CONVERGE CFD [88]. This model empirically correlates the change in particle radius of a 0-D parcel to relevant parcel properties as seen in Equation 4.37. The evaporation rate of the particle can thus be modelled as a function of the liquid and gaseous kerosene density, the diffusivity constant of the kerosene liquid vapour D, the particle dimensions, the Spalding mass transfer number B_d and the Sherwood number Sh_d. The B_d number is used to model the phenomena of diminishing rate of heat transfer to the liquid drop as liquid vapour forms and dissipates near the surface of the droplet [112], and by consequence how the droplet should evaporate when it is surrounded by vapour, whilst the Sh_d is use to model how the particle motion affects the heat diffusivity to convection ratio and consequently what heat transfer phenomena is most relevant.

$$\frac{dr_0}{dt} = -\frac{\alpha_{spray}\rho_g D}{2\rho_p r_0} B_d Sh_d \tag{4.37}$$

This model avoids having to compute the spatially discretized temperature in a (at least) 1-D domain for every parcel, which would significantly scale the computational cost of the simulation. The assumptions made for this model, such as the assumption of perfectly spherical particles with uniform properties are hypothesized to be accurate enough. This model has been used in studies of diesel-reacting sprays, using the same chemistry solver as in this project [113][76]. Additionally, it is considered sufficient and no boiling models were used as it is assumed that particles are small enough to evaporate most of their volume away by the mass transfer mechanisms modelled by the Frossling correlation before reaching the boiling temperature. The breakup of the particles is modelled using a coupled Kelvin-Helmholtz and Rayleigh-Taylor model.

4.4.2. Spray description

The injection of liquid kerosene into the domain is modelled as an initial distribution of moving particles using the Rosin-Rammler statistical distribution with a defined Sauter mean Diameter (SMD). This distribution is preferred over other implementations such as the Chi-Squared distribution and Blob injection (uniform) distribution due to its simplistic implementation, good correlation with experimental results and the fact that it is the most widely used method for spray injection [112], with existing values for this particular setup. The Rosin-Rammler distribution describes a cloud of particles statistically with Equation 4.38.

$$R = 1 - exp\left[\left(\frac{D}{X}^{q}\right)\right] \tag{4.38}$$

The cumulative probability function of the Rosin-Rammler distribution for all particles of diameter lower than a given D depends on the q and X constants. The constant q can be used to adjust the variance in particle size in a cloud of particles, with a higher q representing a cloud of more uniformly sized particles, as seen in Figure 4.3. In CONVERGE CFD, the X term is linked to the Sauter Mean Diameter (SMD) using Equation 4.39, where Γ is the gamma function. This allows for the distribution to yield the correct SMD independently of the chosen q.

$$X = \Gamma(1 - q^{-1}) \cdot SMD \tag{4.39}$$

The kerosene stream is thus entirely modelled using the SMD and q constants, which are known *a priori* from the study on the same combustor using the same injector configuration from Dave et al. [44], where for a liquid mass flow of roughly $10\,g/min$ and a pressure drop $\Delta P = 3.2\,bar$ the SMD is observed to be roughly SMD$=25\,\mu m$ and q is set to $q = 3.1$. This approach avoids the modelling of primary and most of the secondary breakup of the real kerosene stream, a decision based on the design of the SIMPLEX atomizer for high efficiency atomization. It is important to state that the given SMD$=25\,\mu m$ was computed for a plane ahead of the injector. It is known that, with a small ΔP an increase of measured SMD with distance from the injector can be observed with the described numerical implementation, which means the computed value can not be used to define a spray distribution at the injection point. This phenomenon is not necessarily numerical and could be attributed to the sudden imbalance between droplet surface vapour pressure and ambient pressure due to the significant injection

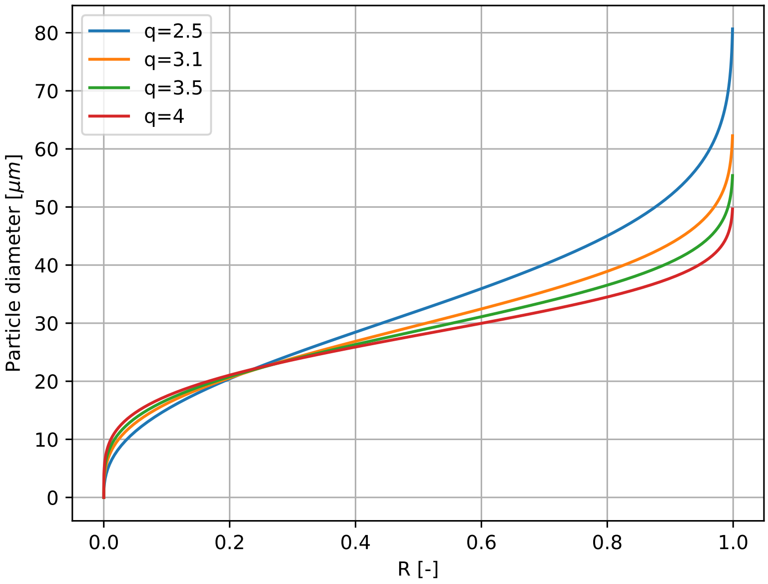

Figure 4.3: Cumulative distribution function of a Rosin-Rammler particle distribution as a function of particle diameter and q.

pressure drop ($\Delta P \approx 3.2\, P_{amb}$), which drives evaporation rates up momentarily until a new equilibrium is reached. This phenomenon should not only reduce the size of all the injected droplets after injection but also disproportionally causes smaller particles to reduce in size more rapidly or completely evaporate, thanks to their smaller radius, potentially leading to an increase in measured SMD. To obtain a downstream distribution that is equivalent to the one observed in previous studies, the injection SMD is instead chosen such that the measured SMD downstream is closest to $25\,\mu$m, which results in the injection SMD of $14.5\,\mu$m.

4.5. Solvers

4.5.1. Iterative algorithm for solution procedure

In the compressible form of the Navier-Stokes equations, the momentum, pressure, and energy are all coupled, which implies that when one of these variables changes, the others have to be recomputed according to the new value. Since this work includes combustion and species modelling, the previously mentioned variables are also coupled with species concentration. In order to solve these variables, an outer algorithm has to be implemented to compute a first guess for some of the flow field variables and then solve all the equations in the correct order, such that convergence for all coupled variables is possible. In this work, the CONVERGE CFD's implementation of the Pressure Implicit with Splitting of Operator (PISO) method [88]. This method first approximates and corrects the momentum and pressure values by using approximate relations for these quantities, a process that can be repeated several times until these variables converge. After this, the remaining equations are solved in series, including the velocity and pressure equations, in order to update the initial values for the next iteration loop. This process loops until the difference in density ρ between the last and current iterations falls below a specified tolerance. This process is described in Figure 4.4.

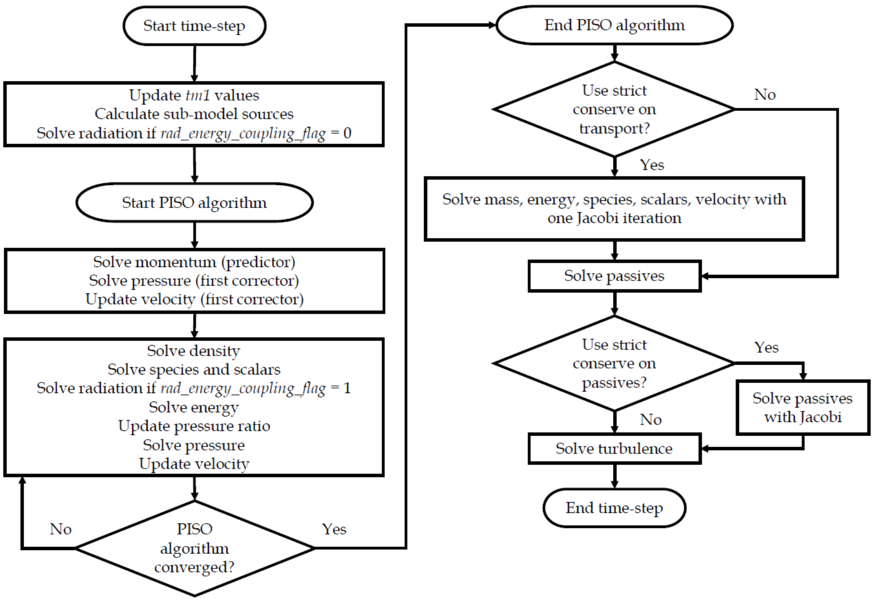

Figure 4.4: Flowchart of the PISO algorithm implementation. From [88].

This algorithm is typically chosen for its efficiency in transient calculations, as compared to other available Pressure-velocity coupling models such as Semi-Implicit Method for Pressure-Linked Equations (SIMPLE), since it typically allows for higher time steps and a more efficient computation loop for transient simulations [114], [115].

4.5.2. Iterative linear solvers

In order to solve the flow field, each equation needs to be solved for a global time step, every time step and for all cells. In order to implement this in a computational environment, for each cell, the equations for the boundaries of that cell are grouped into several system of equations in a time discretized form and then, for each system, the relevant terms are organized into a matrix A as a function of the unknowns' vector x, as seen in Equation 4.40. This system could be simply solved by computing the inverse of A^{-1}, however, A^{-1} will often not be sparse and will contain $\mathcal{O}(N_{grid}^2)$ entries, requiring excessive amounts of computational resources to solve. Instead, the system of equations can be solved iteratively and the residual computed until a certain tolerance is met, which is the preferred method implemented in CONVERGE CFD [88]. In iterative methods, Equation 4.40 is altered in order to achieve an approximate result of the solution at iteration $n+1$ by using the solution from iteration n with far less computational cost, depending on the total number of iterations.

$$Ax = b \tag{4.40}$$

In this project, a combination of the Successive over-relaxation (SOR) and the CONVERGE biconjugate gradient stabilized (CONVERGE-BiCGSTAB) solvers is used to solve different equations, according to how different solvers handle the different structures of each A matrix.

Successive over-relaxation

The Successive Over-Relaxation (SOR) solver is an implicit algorithm that attempts to approximate the solution x with the use of a relaxation factor ω, which in practise dampens or intensifies the change in the solution vector Δx from one iteration to another for $\omega < 1$, allowing for the overall increase in convergence speed. The modified version of Equation 4.40 for this iterative method is replaced by Equation 4.41 for each variable i.

$$x_i^{k+1} = (1-\omega_i)x_i^k + \frac{\omega_i}{a_{ii}}\left(b_i - \sum_{j<i} a_{ij}x_j^{k+1} - \sum_{j>i} a_{ij}x_j^k\right) \tag{4.41}$$

Where a_{ij} is an entry of the A matrix. After so, each element of the solution vector x is under-relaxed using a user-defined and static $\omega_{under\_relax,i}$ factor, a process which is referred to as under-relaxing. The ω_i is automatically computed for each transport equation and controls the convergence speed of each variable, ensuring solver stability. Note additionally that in this implementation, it is ruled in that $\omega_{under\_relax,i} > \omega$ [88]. The optimal value of ω_i is computed from the fraction of the a_{ii} entry in the A matrix against the remaining entries in that discretized transport equation $a_{i=i,j}$, as seen in Equation 4.43.

$$x^{n+1,*} = x^n \cdot \omega_{under\_relax}(x^{n+1} - x^n) \tag{4.42}$$

$$\omega_i = \frac{|a_{ii}|}{\sum_{j,j\neq i}^{J} |a_{ij}|} \tag{4.43}$$

The ω_{under_relax} (and thus the max value of ω_i) needs to be selected and computed with care so as not to achieve far too high values of ω that will destabilize the solution. Kahan [116] proved that for a symmetric and positive-definitive[3] A matrix, a choice of ω between 0 and 2 always allows for the stable convergence. It is then important to underline that when this is not the case, such as in a significantly non-linear system of equations, there are no "safe" values of ω and a $\omega = 1.5$ can lead to instability in the residual convergence. The current combustion simulation is guaranteed to always generate non-symmetrical A matrices for almost all systems, as such, the choice of maximum ω is not straightforward and depends instead on how diagonally dominant the A matrix is [117]. In this project, the coupling between 2 different phase flow equations and the inclusion of species transport breaks the symmetry of the A matrix in some system of equations, which means ω is set close to 1, making this method highly inefficient as it approximates the (relaxed) Gauss-Seidel method. The SOR solver is then chosen for more linear systems of equations, and, if SOR is used, ω is typically set closer to 1. Systems of equations that are expected to behave highly linearly and also obey the stability criterion for SOR (i.e. momentum[4], passives,...) are solved used SOR for efficiency in computation.

Note additionally that pressure is not a transported variable and is not described with a partial differential equation, instead it is often coupled with energy and density which makes the system of equations fairly non-linear. The A matrix in this case will not obey the criterion for stability, and as such SOR is an inefficient (and possibly unstable) solver for this system of equations.

---

[3] A matrix can be said positive-definitive if all its eigenvalues are positive

[4] The effect of the external forces (in general and those acting on the individual species term) is considered negligible and as such the system of equations for momentum is roughly linear

CONVERGE BiCGStab

The CONVERGE CFD Biconjugate Gradient Stabilized Method (BiCGStab), based on the Biconjugent Gradient Method (BiGC), presents itself as a good alternative to SOR for more computationally expensive systems of equations. chapter 4 shows how either of these methods can yield significant increases in simulation performance in cases where SOR reduces down to the Gaus-Seidel method.

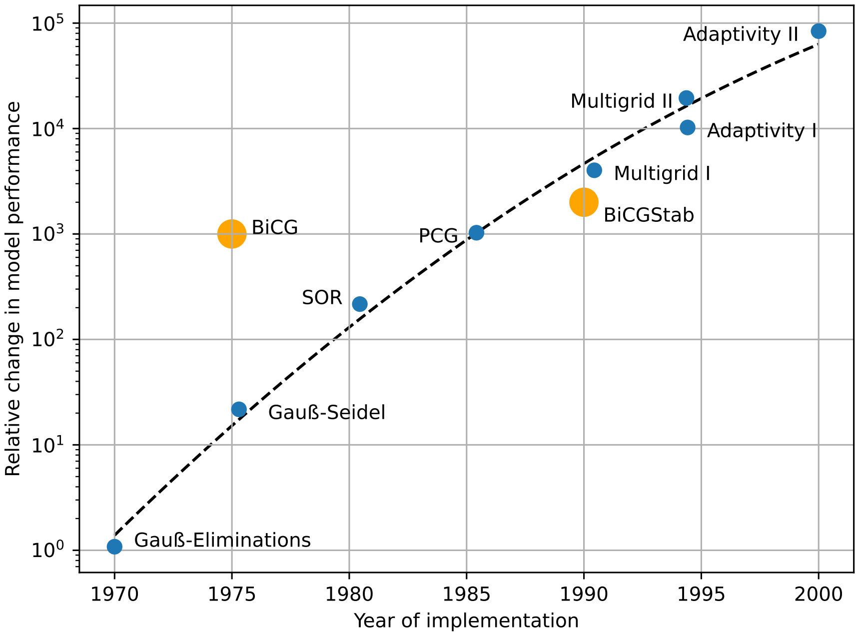

Figure 4.5: Change in developed linear solver computational performance over the years. Change computed in reference to the Gauß-Eliminations method. Quadratic fitting line is plotted as a dashed line (–). Data extracted from [118] plotted in blue. Additional educated estimates for relevant models plotted in orange based on [119], [120].

The BiCGStab method attempts to obtain a approximate solution of the current time step x solution vector computing the search gradient towards the minimization of the residual in a Krylov subspace generated by the A matrix and the initial solution vector r_0, mathematically defined as $\mathcal{K}_r(A, r^0) = span\left\{r_0, Ar_0, A^2r_0, , A^{k1}r_0\right\}$. In the $\mathcal{K}_r(A, r^0)$ subspace, there exists a linear combination of the $A^{k1}r_0$ terms that allows the most optimal correction of the initial x_0 for reducing the residual associated with x. The approach improves on the previously developed BiCG method by computing two vectors in this subspace (s_j and p_j) in order to stabilize convergence[121]. The iteration algorithm is illustrated from Equation 4.44 to Equation 4.50 (in this order), with additional checks in each iteration to verify that the solution has converged within the tolerance. In this sense, Equation 4.40 is replaced by the gradient search described in Equation 4.47.

$$\alpha^n = \frac{r^n r^{n\prime}}{(A\,p^n) r^{0\prime}} \tag{4.44}$$

$$s^n = r^n - \alpha^n (A\,p^n) \tag{4.45}$$

$$\omega^n = \frac{(A\,s^n)\cdot s^n}{(A\,s^n)\cdot(A\,s^n)} \tag{4.46}$$

$$x_j^{n+1} = x_j^n + \alpha_j p_j + \omega_j s_j \tag{4.47}$$

$$r^{n+1} = s^n - \omega_j A s^n \tag{4.48}$$

$$\beta^n = \frac{\alpha^n}{\omega^n}\left(\frac{r^{n+1} r^{0\prime}}{r^n r^{0\prime}}\right) \tag{4.49}$$

$$p^{n+1} = r^{n+1} + \beta^n (p^n - \omega_j A p_j) \tag{4.50}$$

This solver can be accelerated with the use of a preconditioner, which tries to find a matrix M^{-1} to modify Equation 4.40 in order to reduce the number of iterations required for convergence, with the final system being described by Equation 4.51 . It is further noted that this method, unlike SOR, does not depend on the A matrix being symmetric and positive definite, or mostly diagonally dominant, for a stable convergence and has been proven to converge within N iterations, where N is the dimension of A [88], as such this solver is theoretically better applicable for solving the species and energy system of equations. Note additionally that CONVERGE CFD recommends using the BiCGStab algorithm for pressure instead of SOR as the former solver does not suffer from the same limitations in the lack of linearity in the system [88] and as such this solver was chosen for Pressure.

$$M^{-1}Ax = M^{-1}b \tag{4.51}$$

Case specific solver choice for species and energy

From the breakdown of both models, the sensible choice of solver for species and energy is CONVERGE BiCGStab, since the max relaxation factor must be set to a potentially too low value to ensure stability. Furthermore, initial test runs showed that the maximum relaxation factor for both equations must be 1 or lower to avoid stabilization issues. The SOR algorithm with no over-relaxation ((relaxed) Gauss-seidel) is a particularly inefficient algorithm in part due to its simplicity, and the reduction in iterations per time step is expected from the change to BiGCStab. A study of the behaviour of these solvers for this combustor and conditions shows that the SOR solver requires more iterations and the iteration count is less consistent when solving the energy and species equations when compared to BiGCStab, as seen in Figure 4.6. However, particularly to this work and in part due to the small time step and fine mesh approach in areas where species and energy fluctuate the most, both energy and species usually iterate within 1-3 iterations for both solvers and consequently, the BiCGStab solver only manages to reduce the number of iterations by 1-2 in some of the PISO loops for some of the species. Because BiCGStab is significantly more expensive than SOR per iteration, the benefit of cutting down the number of iterations on these systems of equations does not translate into an improvement in simulation speed, and as such, SOR ends up solving the simulation fractionally faster than BiCGStab. On the other hand, this simplistic analysis of the convergence behaviour is not absolutely translatable to the real behaviour of the solver, as the number of SOR iterations is noticeably less consistent than the number of BiCGStab iterations as seen in Figure 4.6, a behaviour likely associated with small peaks in reaction rates and energy release rates. For this reason, BiCGStab is used for the iterations of the energy and species systems. The tolerances used for the SOR iterated systems and BiCGStab iterated systems are given in Table 4.1 and Table 4.2, respectively.

Table 4.1: Tolerances used for each system solved using SOR.

System of equations	Absolute Tolerance
Momentum	$1 \cdot 10^{-5}$
Density	$1 \cdot 10^{-5}$
Passive	$1 \cdot 10^{-5}$
Scalar	$1 \cdot 10^{-5}$

Table 4.2: Tolerances used for each system solved using BICGSTAB.

System of equations	Absolute Tolerance
Pressure	$1 \cdot 10^{-8}$
Energy	$1 \cdot 10^{-4}$
Species	$5 \cdot 10^{-4}$

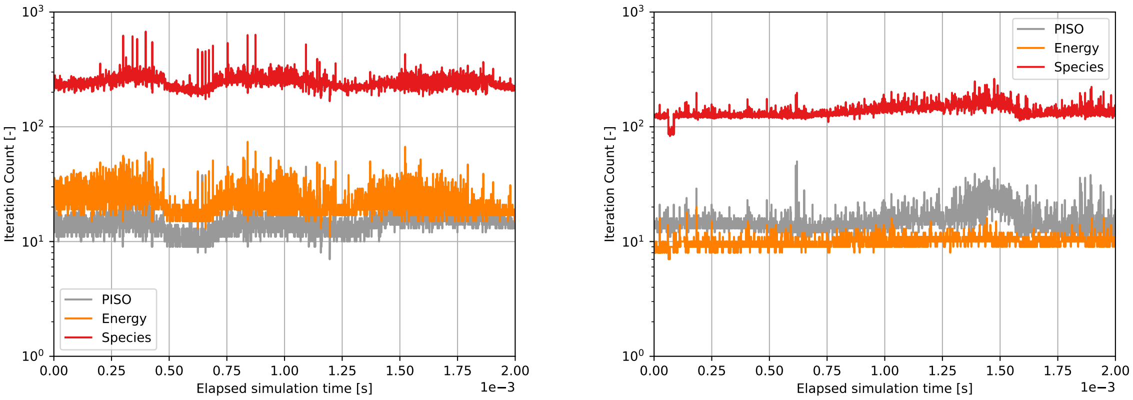

(a) Iteration behaviour for the SOR solver.

(b) Iteration behaviour for the BiGCStab solver.

Figure 4.6: Iterations per time step plotted over elapsed time since change in solver. Relevant metrics are plotted and labelled accordingly. Both solvers were used to simulate the same physical phenomena.

5

Methodology of Combustion modelling

There is a need to correctly capture the relevant combustion phenomena and, as such, further combustion related modelling needs to be incorporated into the solution procedure. In order to model the combustion of kerosene, including the reaction kinetics inside the flame front and to model the reduction/oxidation of modelled species anywhere in the domain, the solver needs to correctly account for the local temperature, pressure and species concentration in order to compute the local source and sink terms for both the species and energy transport equations. Additionally, the combustion model needs to account for the changes in flame characteristics due to turbulent structures, which may induce flame stretching.

Further implementations need to be taken into consideration and this chapter discusses how the reactions are modelled, how the flame front is properly resolved and how emissions how modelled, among other relevant points in modelling the combustion of kerosene and hydrogen in the APPU combustor.

5.1. Detailed chemistry modelling

In this project, the detailed transient chemistry solver (SAGE), implemented by [76], is used to compute the reactions among the several species described in the chosen reaction kinetics mechanism. Contrary to many other models that attempt to simplify the combustion mechanism (i.e. EDM [75], CMC [122][60]) or models that attempt to use pre-computed lookup tables to model source and sink terms (i.e. FGM [68]), SAGE models chemistry without significant simplifications in parallel with the flow solver. The source and sink terms for species m are computed from the sum of the reaction rates for that species $\dot{\omega}_{i,m}$ for all the reactions in the mechanism (reaction i through I), as seen in Equation 5.1.

$$\dot{\omega}_m = \sum_{i=1}^{I} \nu_{mi}\, \dot{\omega}_{i,m} \tag{5.1}$$

$$\sum_{m=1}^{M} \nu'_{m,i}\, \chi_m \leftrightarrow \sum_{m=1}^{M} \nu''_{m,i}\, \chi_m \tag{5.2}$$

The $\dot{\omega}_m$ term depends on the overall stoichiometric coefficient $\nu_{m,i}$, which is the difference between the reactant's side and the product's side stoichiometric coefficients $\nu_{m,i} = \nu'_{m,i} - \nu''_{m,i}$. These coefficients determine the relative mole count for each m species that describes an i reaction necessary to attain a chemical balance in that reaction. ν_m can be used to symbolically represent each reaction (using the species chemical symbol χ_m) as seen in Equation 5.2. The elemental quantities of the reactants and products all react at the same rate $\dot{\omega}_i$ characteristic of each i reaction at a certain set of conditions, however the change in each species concentration scales with their respective $\nu_{i,m}$.

The reaction rate $\dot{\omega}_i$ for the reaction i can be obtained from the law of mass action, which states that the $\dot{\omega}_i$ is proportional to the product of the participating species, in this case the molar concentration of a species $[\chi_m]$ times the forward/backwards rate coefficient k_1/k_2, raised to the power of the stoichiometric coefficient of each species, as described in Equation 5.3. This product defines the affinity of reactants or products, that is, the chemical "force" between species to react with each other, the result of which is the rate at which the reaction occurs in one direction (or the other if the species on the opposite side are considered). The total overall reaction ratio is then defined as the difference between these two.

$$\dot{\omega}_i = k_1 \prod_{m=1}^{M} [\chi_m]^{\nu''_{im}} - k_2 \prod_{m=1}^{M} [\chi_m]^{\nu'_{im}} \tag{5.3}$$

The k coefficient can then be obtained by the Arrhenius equation or, by knowing one of the coefficients, by the equilibrium coefficient k_c as described in Equation 5.4 and Equation 5.5. The pre-exponential factor A_i, temperature exponential factor b_i and the activation energy E_i are previously tuned and can be looked up in the z77 mechanism file (section A.1). These relations include the effect of temperature on the reaction rates, further effects, such as the effect of pressure, were implicitly accounted for in the development of the model. The standard molar entropy S_0^i and the standard molar enthalpy H_0^i for species i is used to compute the equilibrium rate constant k_c.

$$\begin{cases} k_1 = A_i\, T^{b_i}\, exp\left[-\frac{E_i}{RT}\right] \\ k_2 = \frac{k_1}{k_c} \end{cases} \tag{5.4}$$

$$k_c = exp\left[\sum_{m=1}^{M} \nu_{im} \frac{S_i^0}{R} - \sum_{i=1}^{I} \nu_{im} \frac{H_i^0}{RT}\right] \left(\frac{P_{atm}}{RT}\right)^{\sum_{m=1}^{M} \nu_{im}} \tag{5.5}$$

With the model closed and the species source/sink terms obtained, the energy equation source/sink terms can be obtained trivially by working out the 1st law of thermodynamics for a constant pressure, closed system and adiabatic cell as described in Equation 5.6.

$$\frac{dT}{dt} = \frac{V \frac{dP}{dT} - \sum_{m=1}^{M} \dot{\omega}_m\, h_m}{\sum_{m=1}^{M} \chi_m\, C_{p,m}} \tag{5.6}$$

The series of relations described so far presents a model close to what the current accurate understanding of chemical kinetics is. The implementation of SAGE does not assume any flame regime. It does not rely on any assumptions about which species react, making the model applicable in almost every case. The model solves for a predefined, previously validated set of reactions to compute the concentrations of species and the energy consumed for each reaction. The absence of any significant assumptions beyond the chosen reaction mechanism ensures that relevant phenomena such as auto-ignition and flame stretching are inevitably captured by the solver if the chosen chemical mechanism is sufficiently complex. Additionally, this model works for multiple fuels, including hydrocarbons from secondary reactions, so the solver accurately accounts for the exact species and temperature concentrations in every cell and how these affect the local reaction rate and energy release [88]. Consequently, previous research has also demonstrated that this model is well suited for an accurate description of pollutant species distribution for complex combustion descriptions, allowing for the accurate analysis of small but significant changes in emission profiles for species that are included in the chemical mechanism, albeit most research is conducted for internal combustion engines [76], [123], [124].

Note additionally that SAGE is prone to commutation errors when computing the chemical source term due to the effect of temperature fluctuations and of fluctuations in the species concentrations [88]. In LES, this error is expected to converge to zero with the correct refinement of regions of high reaction rate, and, in this work, the ARM algorithm is used to refine areas of high temperature SGS values and high $C_{12}H_{23}$ reaction rate in order to ensure this error goes to zero.

5.1.1. Reaction mechanism

In order to model the correct combustion of kerosene, including correctly computing every species according to the correct pathway activation, the solver must be informed of a reaction kinetics mechanism with all the data on the reactions, elements, species and their respective thermodynamic and transport data. Since the combustion mechanism effectively limits the accuracy of the final results according to its complexity and how well tuned it is against real experimental data, the priority is finding a mechanism that is both accurate and does not exceed the computational cost by modelling all conceivable reaction pathways that a real combustion might entail.

For this project, the Z77 mechanism from Zettervall et al. [78] is implemented. The mechanism is based on their previously developed Z65 mechanism [125] by merging in new reaction mechanisms to better model the auto-ignition behaviour of known paraffin species[1] for a wider range of temperatures. It's important to note that real jet fuel is a combination of several hydrocarbons, a review by Xu et al. [126] noted that Jet A can be described by an average chemical formula of $C_{11.4}H_{21.7}$, however this is still a ideal representation of this type of fuel between all the refinery pathways and sources. In the implemented Z77 mechanism, $C_{12}H_{23}$ is used as a means of representing the Jet A-1 surrogate and any references to $C_{12}H_{23}$ in this report refer to this representative species. The rate constants in Equation 5.4 are tuned in order to correct the new model against experimental data. The resulting Z77 mechanism is larger than the Z65 mechanism, specifically, the number of reactions is up from 65 to 77 reactions, and the number of species of the new mechanism is set to 33.

The chain of past mechanisms that Z77 is built upon and, by consequence, the Z77 mechanism is a result of a skeletal reduction of more detailed mechanisms, that is a reduction in the size of the mechanism by the strategic elimination of less relevant species and reactions that does not impact the final results significantly across a certain range of conditions [127]. As such, it is expected that the mechanism has a higher relative error compared to the original mechanism, however, the computational cost is also greatly reduced, allowing for skeletal mechanisms to better fit in the budget for this project. As noted by [78], the studied freely propagating laminar flame simulations were solved 2-3 orders of magnitude faster when compared to reference highly detailed mechanisms while maintaining good agreement with experimental data. This was also verified by Zettervall [128].

Given the temperature conditions at air/hydrogen inlets, it is important that the mechanism is correctly tuned to handle the combustion of both fuels at the expected lean and low temperature conditions. The mechanism was previously validated for ϕ ranges of 0.5 to 1.7, Pressure ranges of 1 atm to 51 atm and temperatures from 400 K to 1600 K against other mechanisms and experimental data. The first important point to underline is that the Z77 model was validated for a 100% kerosene fuelled flame, and there are no validated laminar flame cases of the same conditions simulated in this project. At $T = 400$ K and $P = 1$ atm, the results of the Z77 match closely the experimental results down until $\phi = 0.7$, and from $\phi = 0.5 - 0.7$ the results also match those of competing and more detailed models closely. There is no data for lower values of ϕ, including values close to predicted overall equivalence ratio ($\phi \approx 0.4$), however the flame is not expected to react at this ϕ as fuel concentration pools in specific zones of the combustor, making it such that most of the reaction zones are likely within the validated ϕ range. Additionally, to the best of the knowledge of the author, there are no current experimental studies that look into the validation of the Z77 mechanism or similar mechanisms under these conditions.

Despite the lack of validation data, reasonable arguments can be made in favour of using the Z77 mechanism. Firstly, at $P = 1$ atm the laminar flame speed studied in [78] and the adiabatic flame temperature studied in [128] show that these characteristics can be approximated to a linear trend for $\phi < 0.9$, with the same slope between the several studied models, which suggests that for $\phi < 0.5$ the behaviour of these models can be extrapolated linearly up to a lower limit ϕ. This could ensure that the Z77 mechanism maintains the same relative error margin against other models until a lower ϕ, likely close to the flammability limits, at which point the mechanisms will model the flame extinction behaviour differently. When plotting S_l against ϕ for a pure jet fuel flame, as shown in Figure 5.1, it can be seen that the model's computed laminar flame speed can be approximated to a linear trend from $\phi = 0.4 - 0.9$. This can also be seen with the relatively more detailed HyChem A2 chemical mechanism from Wang et al. [83][84], which also includes a low temperature chemistry modelling approach. Additionally, both aforementioned validation studies also show that the models converge to the same

---

[1] Paraffin defines species whose average chemical formula is described by C_nH_{2n+2}

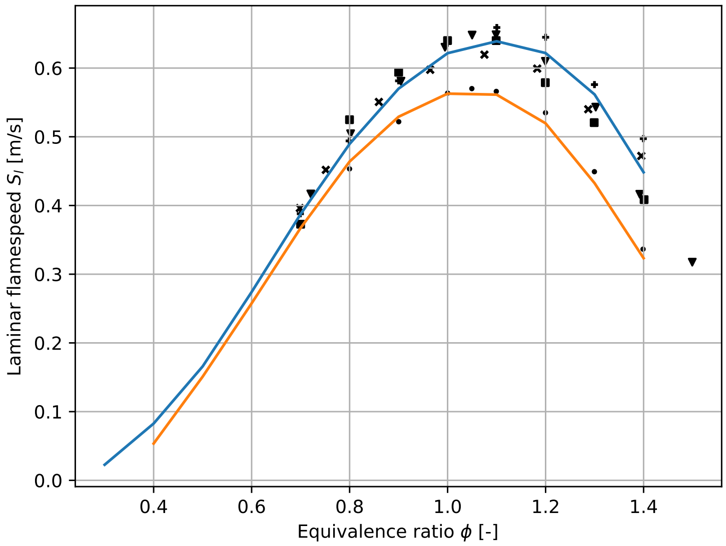

Figure 5.1: Laminar flame speed plotted against equivalence ratio for $T = 400$ K,$P = 1$ atm, modelled using CONVERGE CFD's chemical model. Continuous lines indicate modelled data using the Z77 mechanism (blue) and the HyChem A2 mechanism (orange). Scattered symbols represent experimental data, "●" from [84], "▼" from [129], "+" from [130], "x" from [131] and "■" from [132].

values at leaner conditions, with flame adiabatic temperatures, laminar flame speeds and CO_2 / CO molar concentrations computed to be much more similar between models at $\phi = 0.6$ compared to richer conditions. This remark likely indicates that, for either detailed or skeletal models, the sensitivity of flame characteristics to each chemical pathway is reduced, making differences in tunable parameters and in chemistry pathway complexity between models less relevant to the final flame structure. One possible explanation for this is the lower adiabatic flame temperature of leaner flames that leads to a decrease in the reaction rate of reduction reaction and oxidation reactions, which are the ones tuned most uniquely between each model. Finally, while the model was not tuned for hydrogen combustion, it was adapted from the methane-air model Z42 from Larsson et al. [133], which does include the hydrogen oxidation pathways and thus can be used to model the hydrogen flame, although likely not as accurately as with a model specifically tuned for hydrogen flames. This observation is shared by [46], [84], [128], [134], the latter study additionally pointing out that higher hydrogen concentrations in the fuel might require additional tuning.

On the other hand, the heterogenous distribution of fuel species over the combustor brings forward concerns over the modelled flammability and extinction[2] limits and their impact over the creation and destruction of reaction zones characterized by conditions close to the extinction limits of the local kerosene hydrogen mixture. As pointed out by the original study [78], the extinction limit is limited (not exclusively) by fuel chemical composition and by the species that the main jet fuel species breaks down into, which varies between mechanisms, as different authors can represent jet A surrogates with different chemical formulas. Furthermore, this study also points out that Z77 does not agree with the more detailed HyChem A2 mechanism, which has been successfully validated against experimental data [83], [84], on extinction limits. The authors of the original study [78] hypothesize that the mechanism reduction strategy likely resulted in the modelled flames being more resistant to strain compared to mechanisms such as the HyChem A2 mechanism. The real impact of this observation in this study is ambiguous, not only because the aforementioned results apply to diffusion flames, but also because the predicted flame regime in this combustor is likely partially premixed with possible diffusive reaction zones. It is then worth casting some doubt over the results herein obtained for equivalence ratios close to the

---

[2] While flammability limits account for the local fuel concentration ranges at which the flame can be self-sustaining, extinction limits account for the limits in boundary conditions where the flame can be self-sustaining, effectively capturing the effect of flame stretch

flammability limits of more complex mechanisms if the flame is under the effect of significant stretch.

The Z77 mechanism lacks some accuracy in modelling the flame under very lean and low-temperature conditions, compared to other more detailed mechanisms and to the ideal conditions it was initially validated for. However, there is good evidence that the discrepancy between this and more detailed mechanisms under these conditions remains low and that near extinction phenomena are still modelled reasonably well. Furthermore, the paper on the development of the Z77 model [78] points out that for their simulations, the choice of the next most complex reaction kinetic mechanism, the HyChem A2 mechanism, increases the simulation time by more than twofold, and preliminary tests done in the present work showed that the the LES combustion simulations in the APPU using the HyChem A2 mechanism lead to an increase of the simulation time by close to 50%. It stands to reason that, on an accuracy per computational resources expended analysis, the Z77 mechanism can lead to very acceptable results for a study on the important mechanisms that are affected by the change in inlet air and hydrogen temperature, but cannot lead to high fidelity results on the intricate kinetics of this type of combustion. Just as importantly, however, is that this mechanism is chosen to allow for the study of this phenomenon within the allotted budget for this LES project.

5.2. TFM model

Premixed flames inherently have a flame front region positioned roughly where the mixed reactants achieve enough energy to trigger the combustion reaction, which depends on the local velocity of the reactants. Due to the complex dispersion of local turbulent structures, the shape of the flame front is geometrically rugged and imperfect, varying significantly with local equivalence ratio and flame temperature. For jet fuel, it can be said that the thin reaction region of the flame front, where almost all the combustion of kerosene/hydrogen occurs, is almost always too thin to be accurately captured using the current mesh width of $0.25mm$. One 1989 study [135] noted that the laminar flame front thickness for kerosene should roughly be $0.2mm$-$0.3mm$ for atmospheric pressure and temperature. This value however is obtained for stoichiometric conditions, in reality it varies significantly according to the local equivalence ratio and unburned mixture temperature, the latter of which was also verified by the referred study. The CONVERGE studio chemical module was used to obtain the characteristics of a $C_{12}H_{23}$ flame fronts using the Z77 model. The results plotted in Figure 5.2 show good agreement with the previous study [135] and illustrate that for most cases about $T = 1000K - 1200K$ the entire flame front can only be resolved with 1 to 2 full cells at most, which is predictably not sufficient to capture the significant species and energy gradients across the flame front. Furthermore, according to Damköhler's theory for small scale turbulence, turbulent scales of the same scale as the flame front and smaller need to be modelled or resolved alongside the flame front in order to correctly capture their impact on the flame structure, as seen in previous studies [136].

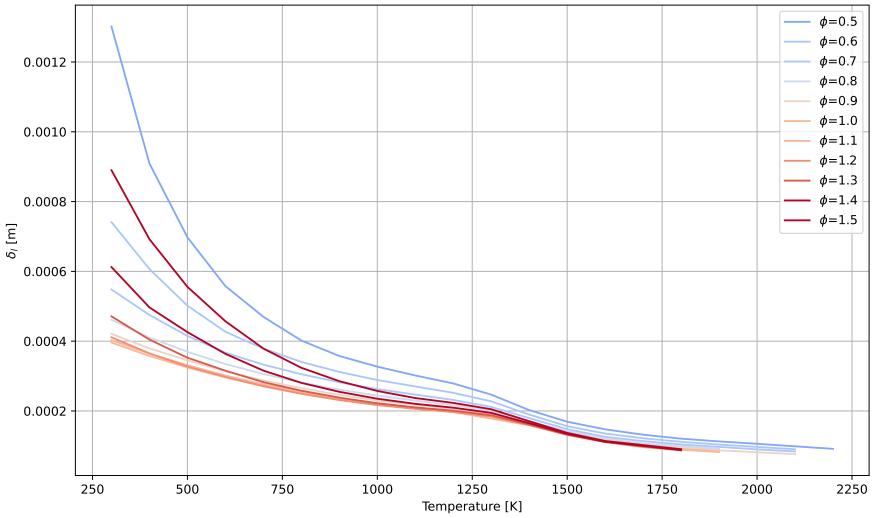

Figure 5.2: $C_{12}H_{23}$ and air fuelled laminar flame thickness plotted against unburned reactant temperatures, computed using the HyChem A2 mechanism to illustrate the behaviour of flame fronts more accurately.

In order to correctly resolve the flame front, this project makes use of the dynamically thickened flame model for LES (DTFLES) [137][88], which is a modification of the previous statically thickened flame model for LES (TFLES). In order to correctly capture the flame front, this model proposes artificially altering the timescales associated with species and energy diffusion by a factor $\mathcal{F}$, effectively expanding the flame front so it can be resolved on a coarser grid. Critically, however, the flame front laminar speed S_l cannot be altered by this thickening, else the reaction mechanism is conditioned by the thickening.

The intended purpose of the model is to increase the turbulent flame thickness by scaling the laminar flame thickness by $\mathcal{F}$, resulting in $\mathcal{F}\delta_l$ as seen in Figure 5.3. The δ_l and S_l can be proportionally correlated to the thermal diffusivity D_{th} (and species diffusivity through the Lewis number) and the specific reaction rate $\dot{\omega}$ through the relations illustrated in Equation 5.7. With these relations, Butler and O'Rourke [138] originally proposed that by increasing the D_{th} and decreasing $\dot{\omega}$ by the same $\mathcal{F}$ factor, the laminar flame thickness can be expanded by $\mathcal{F}$ whilst the flame speed can be maintained constant, as worked out in Equation 5.8. Interpreting this result practically, an equivalent thickened laminar flame front can be created from the original by ensuring that the time taken for the (mean) energy to diffuse through the flame front does not change, and the (mean) amount of species reacted in that same time frame for that section of the flame front also does not change.

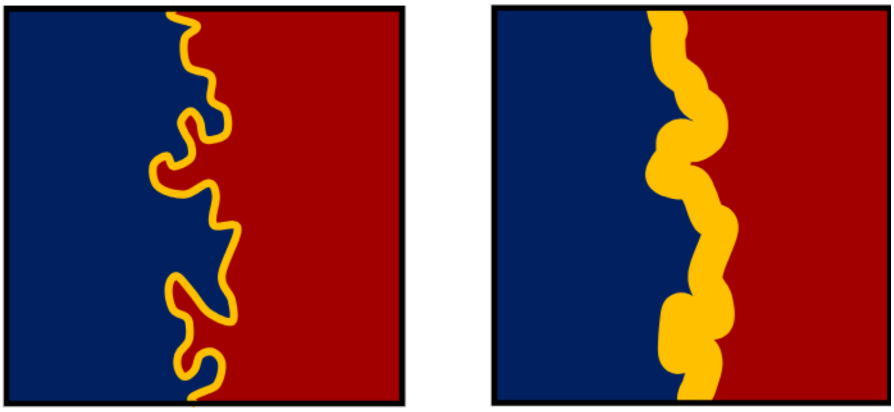

Figure 5.3: Illustration of the thickened flame front (right figure) compared to the original flame front (left figure). Illustration from Convergent Science [88][139].

$$\delta_l \propto \sqrt{\frac{D_{th}}{\dot{\omega}}} \qquad S_l \propto \sqrt{D_{th}\dot{\omega}} \tag{5.7}$$

$$\mathcal{F}\cdot\delta_l \propto \sqrt{\frac{\mathcal{F}\,D_{th}}{\frac{\dot{\omega}}{\mathcal{F}}}} \qquad S_l \propto \sqrt{D_{th}\,\dot{\omega}\,\frac{\mathcal{F}}{\mathcal{F}}} \tag{5.8}$$

In order to implement this model, the scaling is applied to the 2 relevant parameters in the species and energy transport equation, for each of the species involved in the combustion process, resulting in Equation 5.9 for a given species m and in Equation 5.10[3]. Note that both thermal diffusivities and species diffusivities are altered in the same way to preserve the Lewis number, and Equation 5.8 is similar for the species diffusivity.

$$\rho\left(\frac{\partial Y_m}{\partial t}+\frac{\partial u_k Y_m}{\partial x_k}\right)=\frac{\partial}{\partial x_k}\left(\mathcal{F}\,D\,\rho\frac{\partial Y_m}{\partial x_k}\right)+\frac{1}{\mathcal{F}}\,\dot{\omega}_m \tag{5.9}$$

$$\rho\left(\frac{\partial e}{\partial t}+u_j\frac{\partial e}{\partial x_i}\right)=-\frac{\partial \mathcal{F}q_i}{\partial x_i}-p\frac{\partial u_i}{\partial x_i}+\tau_{ij}\frac{\partial u_i}{\partial x_j}+\frac{\partial}{\partial x_i}\left(\rho\sum_{m=1}^{M}\mathcal{F}D_m h_m\frac{\partial Y_m}{\partial x_i}\right)+\frac{1}{\mathcal{F}}S_m \tag{5.10}$$

This implementation is effective in ensuring the flame front is modelled with a sufficient number of grid points to capture the thin reaction kinetics profile.

5.2.1. Dynamic thickening using DTFLES

As mentioned, the DTFLES is a modification of the previous TFLES. With TFLES, the species and energy transport equations are scaled by $\mathcal{F}$ throughout the entire domain, which helps resolve the flame but fundamentally changes the mixing process outside the flame as species will artificially diffuse faster over the original domain, effectively reducing the accuracy of the fields outside the flame front. The implemented solution for this issue uses a sensor model from Jaravel [140] that thickens only the cells enclosing the flame front and leaves the rest unthickened, as illustrated in Figure 5.4.

According to the CONVERGE CFD documentation [88], the description of this model deviates slightly from the method proposed by Jaravel. Here, the model first detects the flame front through areas of high $C_{12}H_{23}$ reaction rate $\dot{\omega}_{C_{12}H_{23}}$ and labels it using the sensor S variable, which can vary between 1 and 0 according to Equation 5.11.

---

[3] The equations are in the unfiltered form for illustration purposes

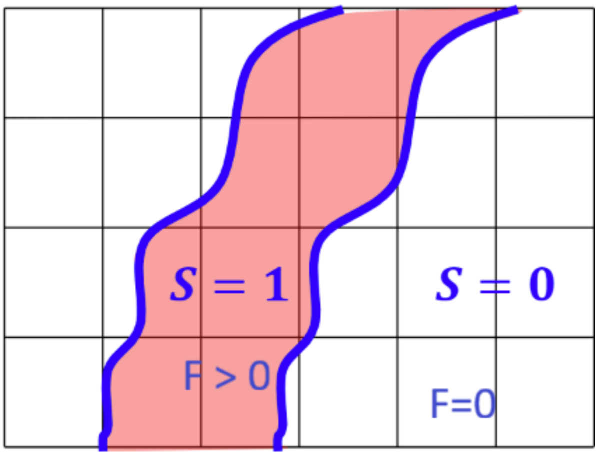

Figure 5.4: Illustration of the flame sensor and its impact on the applied thickening factor $\mathcal{F}$. Red regions represent a (thickened) flame front, and the background grid identifies the mesh cells. Values of Sensor S and thickening factor ($\mathcal{F}$, F in the original illustration) shown for regions outside and inside the flame front. Illustration extracted and edited from Convergent Science [88][141].

$$S = \max\left[\min\left(\beta\,\frac{|\dot{\omega}_{C_{12}H_{23}}|}{\left|\dot{\Omega}_{C_{12}H_{23},max}\right|} - 1,\, 1\right),\, 0\right] \tag{5.11}$$

Where $\dot{\Omega}_{C_{12}H_{23},max}$ is the reference laminar flame reaction rate, $\dot{\omega}_{C_{12}H_{23}}$ is the turbulent reaction rate and β is a constant. The S variable is further modified in order to correctly capture the diffusiveness of species and their respective reactions before and after the flame front using an additional transported scalar Ψ, which diffuses through the flame front. This scalar can be practically interpreted as a pseudo-species that is created in areas where $C_{12}H_{23}$ reacts the fastest, diffuses through the domain much like other chemical species and is destroyed[4] in areas where $C_{12}H_{23}$ is sparse or not significantly reacting. The transport equation of Ψ is given by Equation 5.12.

$$\frac{\partial \rho\,\psi}{\partial t} + \frac{\partial \rho\,u_i \psi}{\partial x_i} = \frac{\partial}{\partial x_i}\left(F\,\rho\,D_\psi \frac{\partial \psi}{\partial x_i}\right) + \frac{1}{F}\,\dot{\omega}_\psi \tag{5.12}$$

$$\dot{\omega}_\psi = \begin{cases} -\frac{-\Psi}{\alpha_h \tau_c} & \textbf{if } S < 0.05,\, T > T_{S=1} \\ -\frac{-\Psi}{\alpha_c \tau_c} & \textbf{if } S < 0.05,\, T \leq T_{S=1} \\ 0 & \textbf{if } 0.8 > S > 0.05 \\ \frac{\Psi_0 - \Psi}{\tau_0} & \textbf{if } 0.8 > S > 0.05 \end{cases} \tag{5.13}$$

Where D_Ψ is equivalent to the thermal diffusivity that drives the diffusion of normal species, although arbitrarily scaled in order to control the width of the sensor ($D_\Psi = a\,D_{th}$). The timescale τ_c is a characteristic flame timescale, while the τ_0, α_h, and α_c timescales control the production and destruction of the flame front, thereby determining the width of the sensor. This filtering effectively expands the sensor as illustrated in Figure 5.5. Unfortunately, there are no standard values for the newly defined variables, and they must be tuned for each specific case, a process covered in subsection 5.2.2. The final filtered sensor $\hat{S}$ is given by

$$\hat{S} = \max\left[\min\left[\Psi, 1\right], 1\right] \tag{5.14}$$

Since the sensor tracks the flame front, in order to implement the dynamic thickening procedure, the $\mathcal{F}$ needs to be modified to be a function of $\hat{S}$ ($\mathcal{F}(\hat{S})$, shortened to $\mathcal{F}$), thus varying spacially as described in Equation 5.15. This coupling ensures that only the flame is thickened as shown in Figure 5.4. The

---

[4] Here it is correct to say *destroyed* as opposed to consumed as Ψ is not a real species, it does not necessarily need to be converted into something else

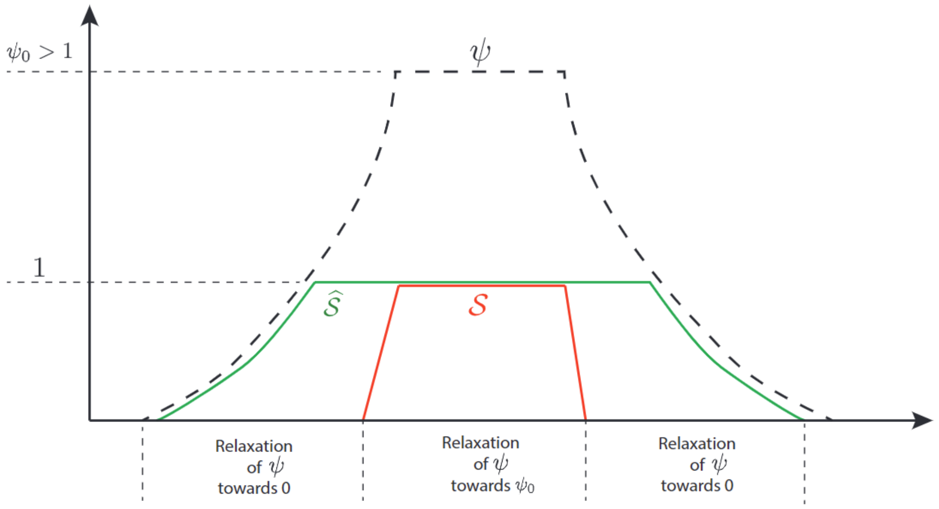

Figure 5.5: Unfiltered sensor S and filtered Jaravel sensor $\hat{S}$ representatively plotted across a flame front. The S is displayed in red and is shown to precisely delimit the high reaction area, $\hat{S}$ is shown to be influenced by Ψ and extend away from the flame front. On the x axis, the relaxation behaviour of the $\hat{S}$ according to the value of Ψ is also represented. Illustration from Jaravel [140].

$\mathcal{F}_{max}$ is the thickening factor used for the centre regions of the identified flame front, which can either be arbitrarily defined or can be computed as a function of the intended number of cell centred grid points N_{GP} across the thickened flame front as a function of local grid width Δ_x and laminar flame front width δ_l as stated in Equation 5.16.

$$\mathcal{F} = 1 + (\mathcal{F}_{max} - 1)\,\hat{S} \tag{5.15}$$

$$\mathcal{F}_{max} = \frac{N_{GP}\,\Delta_x}{\delta_l} \tag{5.16}$$

Thickening the flame alone is insufficient to correctly model the flame dynamics, as the previously unresolved turbulent structures are much smaller than the new thickened flame width and thus reduce the impact of turbulence on the flame structure. This effect is also illustrated in Figure 5.3, where thickening the flame front will lead to a decrease in flame surface area as areas that would be originally wrinkled by small scale turbulent structures are now less impacted by the same structures. This is especially problematic as the stretching due to these flame structures also affects the flame speed, an incorrect modelling of which will lead to different flame temperatures, among other concerns.

To account for the impact of the modelled turbulent scales on the new flame front, the modelling approach by Colin and Ducros [142] is implemented. In this model, a newly introduced wrinkling factor Ξ is precisely defined as the SGS flame surface divided by the projection of the flame surface in the propagating direction, and it computes the effect of the SGS turbulent scales on the wrinkling of the flame front. The Ξ for an unthickened or thickened flame front thickness δ_k is given by Equation 5.17.

$$\Xi_{\delta_k} = 1 + \beta\,_{textColin} \frac{2\ln(2)}{0.84\left[\sqrt{Re_t}^{\,1/2} - 1\right]} \Gamma_{\text{Colin}}\left(\frac{\delta_k}{\delta_l}, \frac{u'_{\delta_k}}{s_l}\right) \frac{u'_{\delta_k}}{s_l} \tag{5.17}$$

Attending to the original definition of this variable, the Ξ directly correlated the laminar flame speed to the local wrinkled flame speed. The model, however, proposes that the DTFLES model introduces additional underestimation of the flame front wrinkling, which is solved by defining the efficiency factor E, defined as the ratio of the Ξ of the unthickened flame and the Ξ of the thickened flame, as described in Equation 5.18.

$$E = \frac{\Xi_{\delta_l}}{\Xi_{\mathcal{F}\delta_l}} \tag{5.18}$$

To implement this, note that the efficiency factor is not intended to directly alter the flame thickness, as it is only used to compute changes in the reaction rate due to unresolved flame wrinkling. As such, additional care is needed to ensure this fact. According to Equation 5.7 and Equation 5.8, this change can be implemented by multiplying both D_{th} and $\dot{\omega}$ by E as seen in Equation 5.19. The DTFLES coupling with the Colin and Ducros model is then implemented by substituting the original species and energy transport equations with Equation 5.20 and Equation 5.21, respectively. Note additionally that, according to the theoretical basis of the Jaravel sensor model, the transported scalar Ψ needs to be transported the same way as the chemical species and thus its transport mechanism must be modified also to include the modelling of SGS turbulent interactions. the new transport equation is given by Equation 5.22.

$$F \cdot \delta_l \propto \sqrt{F \, \frac{D_{th}}{\frac{\dot{\omega}}{F}} \frac{E}{E}} \qquad\qquad E \cdot S_l \propto \sqrt{D_{th}\dot{\omega}\, E^2 \, \frac{F}{F}} \tag{5.19}$$

$$\rho \left(\frac{\partial Y_m}{\partial t} + \frac{\partial u_k Y_m}{\partial x_k} \right) = \frac{\partial}{\partial x_k} \left(\mathcal{F}\, E\, D\, \rho \frac{\partial Y_m}{\partial x_k} \right) + \frac{E}{\mathcal{F}}\, \dot{\omega}_m \tag{5.20}$$

$$\rho \left(\frac{\partial e}{\partial t} + u_j \frac{\partial e}{\partial x_i} \right) = -\frac{\partial \left(\mathcal{F} E q_i \right)}{\partial x_i} - p \frac{\partial u_i}{\partial x_i} + \tau_{ij} \frac{\partial u_i}{\partial x_j} + \frac{\partial}{\partial x_i} \left(\rho \sum_{m=1}^{M} \mathcal{F} E D_m h_m \frac{\partial Y_m}{\partial x_i} \right) + \frac{E}{\mathcal{F}} S_m \tag{5.21}$$

$$\frac{\partial \rho\, \psi}{\partial t} + \frac{\partial \rho\, u_i \psi}{\partial x_i} = \frac{\partial}{\partial x_i} \left(F\, \rho\, E\, D_\psi \frac{\partial \psi}{\partial x_i} \right) + \frac{E}{F}\, \dot{\omega}_\psi \tag{5.22}$$

The DTFLES is then chosen as it potentially allows for the correct resolution of characteristically thin flame fronts whilst still utilizing the detailed combustion model. There are drawbacks to this approach, especially as $\mathcal{F}$ increases, however, the use of additional models, such as the efficiency model, help correct for changes in the flame front and fluid flow interactions. Rochette et al. [143] studied the use of DTFLES with a constant number of grid points N_{GP} and found that the model was able to correctly capture and track the flame front and was shown to improve the prediction of large scale phenomena such as local extinction of the flame front. Colin et al. [142] and Charlette et al. [144] further observed that the use of efficiency models allows for the accurate description of turbulent scale interaction with the flame front independently of the thickening factor, with good agreement between LES and DNS results. One highlighted issue, however, is that the efficiency function often needs to be calibrated against DNS data, a procedure that is outside the scope of this project. Furthermore, both studies defend that there is a need for further validation of both DTFLES and the efficiency models. Internal studies from Convergent Science [88][141] show that the use of DTFLES can significantly increase the accuracy of the resolved flame front up to at least $N_{GP} = 7$ for a propane and air fuelled flame, with further thickening of the flame front yielding worse results.

The lack of studies on the use of this modelling approach for multiphase combustion of kerosene/hydrogen flames further highlights the need to validate this model for future use, however existing research suggests that the model is likely adequate for the intent of correctly resolving the flame front using a low cell count.

5.2.2. TFM sensor tuning

Due to a lack of studies on sensor value tuning, the process described in this section is a result of a feedback loop of initial simulations using the conditions for case A. Tuning of the sensor follows the principles defined by Jaravel [140] listed below.

- The sensor must encompass the source terms of the reaction zone.
- The sensor must extend to the ”cold”[5] side to capture relevant temperature and density gradients before the flame front.
- The sensor must not extend too far towards the ”hot” side to avoid thickening non reacting areas.

In the process of tuning the TFM sensor, it was found that the most relevant parameters towards the control of sensor dimensions are the number of grid points N_{GP} used to define $\mathcal{F}$, the reference reaction rate of jet fuel $\omega_{C_{12}H_{23},ref}$, the sink timescale of the Jaravel transported quantity on the ”cold” side $\alpha_{c,\Psi}$, the sink timescale of the Jaravel transported quantity on the ”hot” side $\alpha_{h,\Psi}$ and the source timescale in $S = 1$ regions τ_{Ψ}. The value of Ψ_{ref} was kept constant at $\Psi_{ref} = 20$ as no significant impact was reported by Jaravel.

Number of grid points

It is of interest to correctly capture the temperature and species inside the flame front, given that the accuracy of the SAGE model is dependent on the number of points used. The recommended range for this quantity is anywhere between 5 and 10 grid points [88]. It is trivial that, for a 1D case, a higher number of grid points would directly lead to an increase in accuracy in the final flame solution up until grid convergence is achieved. This observation is valid because the flame is only allowed to propagate and expand in one direction. In a 2D or 3D flame, the same observation does not hold, as increasing the flame size can lead to secondary phenomena, as the spatial distribution of the flame front is significantly altered, leading to changes in how the flame interacts with the flow field and with itself (i.e. wrinkling, merging of flame fronts).

While tuning the sensor, it was found that when using $N_{GP} = 12$ the flame would artificially extinguish on account of the reduced volume of the high temperature region in which droplets could evaporate, and the folding of surface wrinkles that effectively lead to the ”pinching” of the flame surface. Some studies have also found that increasing the N_{GP} close to the suggested upper limit can also reduce the accuracy of the simulation [88][141]. For this study, and in order to preserve some of the turbulent interactions with the flame front whilst preserving the correct discretization of the flame front, it was chosen to keep $N_{GP} = 6$

Reference reaction rate

To capture the flame front, a reference reaction rate needs to be selected such that the sensor can accurately track the flame front in space. According to jaravel, the sensor should encompass the source terms of the reaction zones but not extend too far into either side of the flame front. In theory, according to Equation 5.11, this value should reflect the maximum expected $C_{12}H_{23}$ reaction rate. In the process of tuning the sensor, however, it was found that selecting the maximum reaction rate that matched the theoretical conditions of the setup resulted almost always in a sensor that exceeded the flame front width two or threefold in some specific areas. The characteristic poor mixing quality of this combustor geometry causes fuel to pool in certain zones before reacting, resulting in a flame that is often poorly premixed. Furthermore, due to the strong turbulent interactions with the flame, the laminar reaction rate is expected to be an underestimate of the turbulent reaction rate.

No guidelines were found in picking an actual value for the maximum expected $C_{12}H_{23}$ reaction rate. In the process of tuning the sensor, it was found that the sensor encompassed most of the flame front without significant over thickening when $10^7 < C_{12}H_{23} < 10^8$, with effects of over thickening becoming relevant for $C_{12}H_{23} < 10^6$. Looking at Figure 5.6, these ranges of reaction rate match the laminar values for highly heated and close to stoichiometric condition laminar flames. The mismatch between the real flow in the complex geometry of the combustor and the perfect 1D laminar free flame could be cause for additional assessment over what value of $\dot{\omega}_{C_{12}H_{23}}$ to use. There is no explicit relationship that captures the heating of the reactants and the pooling of fuel species prior to reaction, and allows for the

---

[5] ”cold” and ”hot” refer to the unburned and burned regions before and after the reaction zones, respectively

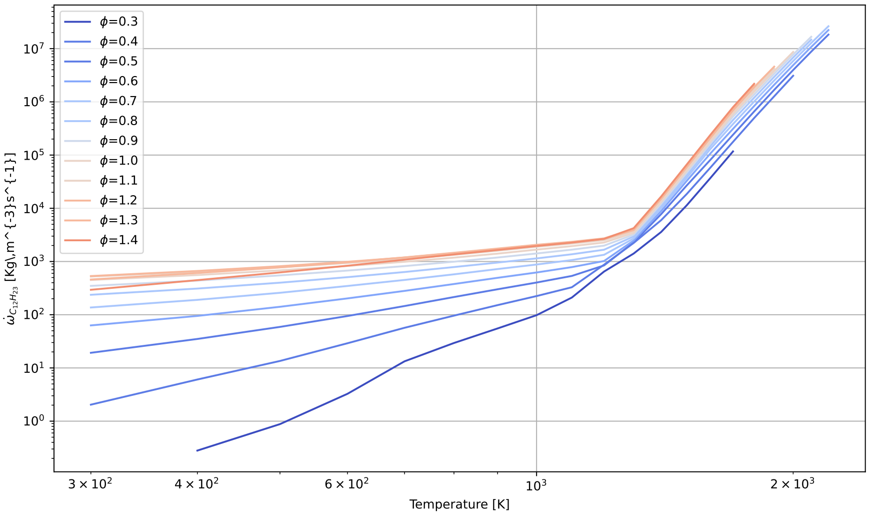

Figure 5.6: Reaction rate of fuel $\dot{\omega}_{C_{12}H_{23}}$ plotted against reactant temperature for several equivalence ratios ϕ. A natural logarithmic scale is used for the y axis scale, and the Z77 mechanism is used.

a priori assessment of a value. This analysis suggests that the lack of guidelines is a consequence of the specific simulation case, and this value will more often than not need to be studied for each specific case.

Sensor timescales

The practical effects of the timescales can be deduced from the transport equation of Ψ itself (Equation 5.12). In essence, it's reasoned that the sink time scales effectively control how the sensor is ”smudged” or tightened into or away from either side of flame fronts, thereby controlling the thickening of the flame front in just one direction. In a 1D domain, Jaravel found that the filtered sensor width can be directly proportional to these timescales (Equation 5.23, where p is a constant, α and β define the chemical timescale and the diffusivity scaling, and δ_T is the turbulent flame width). Although the source timescale can also be interpreted as a way to preserve the $S > 0.8$ regions in time, effectively thickening a flame front for a fast fluctuating flame front, it can also be interpreted as a way to control the ”refresh” rate of the sensor, effectively allowing for a more responsive control over how the sensor moves with the flame.

$$\Delta_{sensor,filtered} \propto p\,\alpha\,\beta\,\mathcal{F}\delta_T \tag{5.23}$$

In the tuning process of the sensor, it was found that changes in the source timescales often need to follow changes in the sink timescales. Significantly increasing the source timescales but keeping the sink timescales constant can lead to over thickening of the flame front, as mentioned previously. Significantly decreasing the source timescale while keeping the sink timescales constant has the opposite effect, where the sensor becomes thinner around flame fronts that are rapidly changing in time. Additionally, since these timescales work to change Ψ in time, the effect of changing either of these timescales is not fully realized until a few time steps ahead of the implementation. For this work, the source timescale was fixed at a standard value of 10, and the sink timescales were tuned around this value until satisfactory results were obtained. It was found that the flame front was accurately captured with sink timescales in the order of 10^{-3}, and the cold/hot sink timescales were chosen according to the principles proposed by Jaravel. The final values of the used timescales are presented in Table 5.1.

Table 5.1: Timescale values used for the Jaravel filtered TFM sensor model.

α_c	α_h	τ_c
$0.005\,s$	$0.001\,s$	$10\,s$

5.3. Emissions

In order to measure relevant polluting species, it is important to establish that the chemical reaction mechanism only includes information to solve for the list of species identified in section A.1, which includes CO$_2$, CO, H$_2O$, and CH$_4$, among other species. The combustion model as described does not include information on the reaction pathways or solve any transport equations for NO$_x$, nor does it solve for soot particulate. Since the study of these pollutants is of interest in this work, a series of models is used to estimate them.

5.3.1. Soot modelling

To model Soot, CONVERGE [88] offers Empirical, Phenomenological (Semi-empirical), and Detailed soot modelling strategies. These types of models attempt to estimate Soot formation from simple empirical correlations or from modelling descriptions of the phenomena responsible for the formation and growth of soot particulates. The more detailed models often estimate specific Soot quantities far more accurately than empirical models, as soot emission strongly depends on the type of fuel and how soot precursor species, also known as polycyclic aromatic hydrocarbons (PAH), are formed, which often goes unmodelled using empirical strategies [145].

In this work, the choice of a skeletal chemical reaction mechanism results in the lack of soot precursor species being solved for in the domain, making it impossible to use models that rely on data for these species. As such, in CONVERGE [88], the only feasible modelling strategy is an Empirical modelling of the Soot production using the Hiroyasu soot model from Hiroyaso et al. [146] coupled with the Nagle and Strickland-Constable (NSC) formulation for oxidation parameters [147]. The original empirical model describes the source of soot particulate only as a balance between formation and oxidation mechanisms as seen in Equation 5.24. Each soot source term is modelled using the Arrhenius equation for a pair of simplified chemical reactions that represent the general formation and oxidation of soot particles. The NSC model is introduced to improve the oxidation modelling by describing soot particles as having two distinct surface areas of different reactivity rates, which results in 2 different mechanisms for the oxidation of soot particles. The soot source term is described as the difference between Equation 5.25 and Equation 5.26, where E_{sf} is the soot formation activation energy, A_{sf} is the Arrhenius pre-exponential factor, a_{so} is a scaling factor for the soot oxidation mechanism, d_s is the diameter of a soot particle and R_{total} is the total oxidation rate.

$$\frac{dm_s}{st} = \dot{m}_{formation} - \dot{m}_{oxidation} \tag{5.24}$$

$$\dot{m}_{formation} = SF\, m_s = A_{sf} P^{0.5} exp\left(\frac{-E_{sf}}{RT}\right) \tag{5.25}$$

$$\dot{m}_{formation} = SO\, m_s = 12.011 \cdot a_{so} \frac{6}{\rho_s d_s} R_{total} \tag{5.26}$$

The NSC model computes the proportion of zones with a distinct reaction rate X_{react} (in this case, between zone 1 and 2) as a function of oxygen partial pressure P_{0_a} and the reaction rates k, yielding Equation 5.28. This proportion is then used to compute the total soot oxidation rate R_{total} according to Equation 5.27.

$$R_{total} = \left(\frac{k_1 P_{0_a}}{1 + k_Z P_{0_a}}\right) X_{react} + k_2 P_{0_a}(1 - X_{react}) \tag{5.27}$$

$$X_{react} = \frac{P_{0_a}}{P_{0_a} + \frac{k_T}{k_2}} \tag{5.28}$$

As mentioned, this model significantly simplifies soot modelling and only allows for the computation of an average cell value of soot mass density. This means that the results cannot be directly correlated with experimental data on soot number density

Furthermore, it does not consider fuel composition or the species present in the cell in its estimates of soot production, nor does it account for additional phenomena such as soot particle nucleation and coagulation. Additionally, since it is an empirical model, the most correct way of implementing it would be to sample data on emissions and conditions in and around the flame for this geometry and combustor and tune several of the empirical variables in order to match the data better on subsequent simulations, which is not possible for this study. The choice of this model is a consequence of the measures undertaken to reduce computational resources and, thus, predictably does not yield accurate results.

On the other hand, the choice of this model is not unprecedented as it is still one of the most widely used empirical models[145]. Despite the lack of accuracy, the Hiroyasu-NSC soot model can still accurately describe trends in soot formation even when the flame is not perfectly mixed[148]. In this sense, understanding the limitations of this model, the soot emission results will need to be analysed carefully to determine whether the change between case A and case B is sufficient to justify a correlation.

5.3.2. NOx modelling

Some of the relevant emissions studied in this work are nitrogen oxides such as NO_2 and NO, and nitrous oxide N_2O. The predicted changes in fuel premixing should, in theory, lead to a change in the concentration of NO_x emissions in the far field of the flame. To model these mechanisms, it's important to understand how these species are typically formed.

The current understanding of NO_x formation pathways is described using a combination of several mechanisms, including but not limited to the thermal NO_x, Prompt (Fenimore) NO_x, Fuel NO_x, N_2O, NO_2 and NNH mechanisms [149][150]. Detailed studies on NO_x emissions attempt to model most if not all of these mechanisms by using chemical kinetic mechanisms tuned specifically to account for the formation of NO_x through the several mechanisms [82][151][45]. Due to the use of the Z77 skeletal mechanism, however, no nitrogen or nitrous oxides are transported and solved for in the domain.

In order to compute the NO_x emissions, some of the mechanisms have to be manually introduced using additional models. In this work, the extended Zel'dovich mechanism for modelling thermal NO_x production is used to introduce 3 reactions and one species the existing chemical kinetics mechanism, as seen in Equation 5.29. The reaction rates of these quantities are computed from the Arrhenius equation (Equation 5.4) using pre-defined parameters. Since SAGE is used, the concentration of all the species (except NO) is obtained using the SAGE combustion modelling approach.

$$O + N_2 \rightleftharpoons NO + N \tag{5.29}$$

$$N + O_2 \rightleftharpoons NO + O \tag{5.30}$$

$$N + OH \rightleftharpoons NO + H \tag{5.31}$$

This model includes the modelling of NO_2, although using an empirical ”converting” factor between NO and NO_2 set to the ratio of molecular weights between both species ($W_{NO_2}/W_{NO} = 1.533$). CONVERGE [88] mentions that this value should be adjusted using experimental data for the estimation of more appropriate values, no experimental case for the exact conditions of case A and case B exists, and as such, this value is kept at the standard value.

This choice of modelling is quite restrictive compared to the more detailed NO_x studies mentioned. Firstly, out of the presented mechanisms, only one is introduced and modelled using a model that has not been tuned with the Z77 mechanism. Additionally, not only is N_2O not modelled by any other model, but NO_2 is also crudely modelled and the concentration equilibrium ratio between NO and NO_2 is debatably at odds with what would truly be observed in experimental simulation of this setup, as seen in the work of Dave et al. [44] where the ”converting” factor could vary anywhere between 0.5 and 5 for this equivalence ratio. Finally, the rate constants used are those originally suggested by Heywood [152], which do not accurately reflect the rate values in this combustion setup.

However, it has been previously observed that, in similar combustion setups, the thermal, fuel (Fernimore) and prompt mechanisms are responsible for a majority of the NO_x production[57]. In this particular case, the thermal mechanism is more likely to have a far more significant impact on the final NO_x concentration as no nitrogen-based fuels are used and the combustor is predominantly operating at close to lean blowout limits, making the fuel (Fernimore) and prompt mechanisms arguably much less significant. The same study also noted that one of the effects of partially premixed hydrogen injection is the increase of flame temperature far beyond the flame temperature attained with other fuels, further elevating the thermal mechanism as the dominant mechanism behind NO$_x$ formation.

With the use of this modelling approach, it is recognised that the chemical kinetics mechanism and reaction rate parameters used will not yield accurate values of NO$_x$ emissions, however, since the main mechanism is captured in the same way between both simulations, it is understood that a trend between case A and case B can be extracted from these simulations.

6

Data treatment

The results are directly extracted in the $.h5$ format and require further processing to evaluate the changes between case A and case B on phenomena relevant to the research questions. In order to evaluate emissions, flame stretch, species distribution and mixing quality, among other parameters, an appropriate analysis plan is required. The following sections describe the methodology behind the post-processing methods.

6.0.1. Measuring mixing quality

In order to evaluate changes in fuel premixing, it is important to understand how the flame structure changes with poor premixing. As [39], [40] have noted, partially premixed flames have a tendency to form secondary flame fronts upstream of the jet fuel flame, which does not happen in fully premixed cases, as the hydrogen is too diluted to sustain a pure hydrogen flame. Although the injected hydrogen flow rate for the conditions used in this work (Table 3.2) is unlikely to allow for a consistent pure hydrogen flame structure to be formed, it's likely that in areas where the dilute hydrogen meets some of the evaporated jet fuel, there is a secondary flame front. Taking into account these observations and given that the mass flow rate of injected hydrogen is constant between cases, it is then proposed that the mixing quality should be evaluated through the identification and analysis of these independent reaction zones.

To do this analysis, the equivalence ratio of the hydrogen species in a pure hydrogen combustion, ϕ_{H_2}, is defined as the ratio of cell wise fuel species to air ratio ψ_{H_2} to the stoichiometric ratio of fuel species to air ratio $\psi_{H_2,stoic}$ as defined in Equation 6.1. The $\psi_{m,stoic}$ is computed for a irreversible and complete reaction described in Equation 6.2 yields $\phi_{H_2,stoich} = 0.02777$.

$$\phi_{H_2} = \frac{\psi_{H_2}}{\psi_{H_2,stoic}} \tag{6.1}$$

$$2\,H_2 + (O_2 + 4\,N_2) \rightarrow 2\,H_2O + 4\,N_2 \tag{6.2}$$

Additionally, the overall equivalence ratio ϕ_O is defined as the ratio of overall fuel to air ratios ψ_o between the reaction at a given cell and a stoichiometric reaction of both fuels. This variable is computed inside CONVERGE CFD [88] based on the original implementation by Mueller [153], presented in mathematical form in Equation 6.3 using the ratio between the sum of carbon atoms N_C and hydrogen atoms N_H and the sum of all oxygen atoms N_O in the cell of an Eulerian field. Although the estimate is less accurate for a jet fuel/hydrogen blend [154] compared to a single fuel simulation, this relation is still more accurate for measuring the instantaneous amount of fuel and oxidizer available, as it accounts for the secondary hydrocarbons at any given cell, which can themselves react [153]. This description would not be possible if ψ_o were defined using just jet fuel and hydrogen. Lastly, the Heat Release Rate (HRR), defined as the sum of the instantaneous heat release rates of the reacting species, is computed by CONVERGE, normalized by the cell mass and volume, and extracted in the $.h5$ output.

$$\phi_o = \frac{2N_C + \frac{1}{2}N_H}{N_O} \tag{6.3}$$

To evaluate mixing quality between the two fuels, the HRR cell data is extracted from a control volume and plotted against each cell's ϕ_{H_2} and ϕ_O, enabling categorization of each flame front according to the fuel mixture. A fully premixed mixture will ideally yield a single HRR peak for a given combination of ϕ_{H_2} and $\phi_{C_{12}H_{23}}$. However, the simulation results should predictably yield at least 2 HRR peaks, with additional peaks likely representing the heterogeneous distribution of fuel within any given combustor section. The difference in the distribution of the HRR peaks in the ϕ_{H_2},ϕ_O plane can be used to qualitatively assess how the two fuels mix.

6.0.2. Measuring emissions

Due to the lack of computational resources to simulate until full statistical convergence, the species are expected not to have sufficient time to reach the outlet boundary and thus cannot be measured by using a mass-weighted averaging of the mass flow through the outlet. Additionally, given that the high reaction rate regions shift spatially in a chaotic manner within the lower section of the combustion chamber, it is also arguably difficult to define a plane that can capture the flow of recently created species without also intersecting these areas, which would result in readings that do not match the actual far field emissions. A plane that is too close to the flame also suffers from skewed measurements as outer recirculation zones and flow field oscillations cause the net mass flow rate to be positive or negative, depending on the time picked or the spatial location.

To circumvent this limitation, a mass-weighted integral of the species mass fraction is performed around a cylindrical control volume that encapsulates a portion of the combustion chamber volume at a given x value. This value will need to be determined *a posteriori* as a suitable location with relatively low measured reaction rate should be found. In order to make this analysis, a series of small volumes along the axial direction of the combustor is used in order to measure how the measured data changes with axial position. For these volumes and the emissions, the standard deviation is also evaluated to assess whether the averages are representative of the entire set of points used. The Std. deviation is obtained using Equation 6.4, where N is the number of samples and a is the individual sample value.

$$\text{Std. deviation} = \sqrt{\frac{\sum_i (a_i - \bar{a})^2}{N}} \tag{6.4}$$

6.0.3. Progress Variable and flame-front description

In the interest of analysing the progress of the main reaction between jet fuel/air and oxidizer inside the flame front, a Progress Variable (PV) should be defined as a variable used to identify the extent of the chemical reaction at a given point inside the flame front and consequently label that point according to how much fuel has reacted with the oxidizer. A general value of the progress variable is hard to determine and depends on the specific case. A general definition based on research from Akkurt [155][156] for diffusion flames defines the PV obtained from an optimal combination of species. For premixed flames outside the stoichiometric range, Chen et al. [157] argue for the use of a dynamically computed value of the PV based on the local Bilger's formulation for the mixture fraction to account for the heterogeneous distribution of fuel. Since the PV needs to be normalized so that it equals 0 in the far field before the flame front and equals 1 in the far field after the flame front, this approach ensures correct normalization, accounting for local species concentrations.

In this work, the flame regimes are expected to range from almost entirely diffusive to well premixed, and a general definition of PV is expensive to study and implement, meaning it falls out of the scope of this project. Furthermore, the flow in the combustor leads to complex flame geometries, and it is not feasible to measure any local mixture fraction without first knowing the position of the flame front, which itself is identified by the PV. As such, the PV is normalized to that of a laminar jet fuel/hydrogen flame under stoichiometric conditions. Note that this is an aggressive approach to modelling a PV, and it is likely that this variable will not be monotonic, that $PV = 0.5$ will not match the point at which 50% of reactants have reacted and that the PV definition does not apply to the entire flame front. For this reason, this report uses the definition of Pseudo Progress variable (pPV) in order to identify the rough region where the flame front is located, but not the progress of the reaction itself. The pPV uses the water mass fraction Y_{H_20} as a common product of both jet fuel and hydrogen and is normalized by the computed equilibrium Y_{H_2O} in the far field of a reaction characterized by the Z77 mechanism with the same boundary conditions as the ones set for each case. Using the Cantera tool[80] for the aforementioned computation yields that for case A $Y_{H_2O,\infty} \approx 0.1049$ and for case B $Y_{H_2O,\infty} \approx 0.1036$. The PV is then computed according to Equation 6.5

$$pPV = \frac{Y_{H_2O}}{Y_{H_2O,\infty}} \tag{6.5}$$

In order to identify the flame front for the analysis of the flame stretch factor, the pPV is used. It follows that the result of the pPV is not restricted to $[0, 1]$ but instead can be bigger or smaller than 1, meaning no information about the real reaction progress can be extracted. However, it is known *a priori* that the flame in this combustor is primarily diffusive, meaning the zones identified by pPV might actually correctly delimit the reaction zone. If this is the case then the flame front can be roughly identified by analysing the $pPV = 0.5$ surface, which corresponds to the rough geometric mean point of the flame front. This analysis is only valid if the flame front is predominantly diffusive and if pPV is close to 1 near the products region.

6.0.4. Measure global consumption speed and flame stretch factor

To assess the effect of proper fuel mixing on the Global Consumption Speed GCS, this quantity is calculated for the flames for each of the studied cases. The formula for the GCS is given in Equation 6.6 and is defined by reference quantities that characterize the reaction. Note that this formulation of the GCS allows for the computation of a normalized, representative GCS and not a physical GCS, the latter of which would require the precise definition of the entire flame front, the volume integral of the reaction terms over this flame front and the careful computation of, ρ_u, $Y_{f,u}$ and A_f. For this setup, $\dot{\omega}_f$ should be the accumulated reaction rate of both H_2 and $C_{12}H_{23}$, and it should be integrated over the flame area A, which itself is chosen to be defined by $pPV = 0.5$. Note additionally that due to the use of a TFM model, the computed reaction rate needs to be multiplied by $\mathcal{F}$ and E^{-1} to obtain the actual reaction rate, given in Equation 6.7. This choice in computing GCS is made as the flame front is resolved with an insufficient number of grid points for a smooth description of species and energy gradients, making it such that most of the fuel consumption rate is computed within 1-2 cells perpendicular to the flame front, which should be captured by a single pPV isosurface instead of the flame front volume. The reference ρ_u of the unburned mixture is captured using a mass-weighted average of the density at the injection port (at $x = -0.025$ m, where $x = 0$ is the start of the combustion chamber). The $Y_{f,u}$ is obtained from the ratio of the injected reactant mass flow rates, corrected by the number of particles that do not evaporate. The reference area A_{ref} is set to $1\,m^2$ for both laminar and turbulent computations.

$$GCS = \frac{-\int_A \dot{\omega}_f \, dA}{\rho_u Y_{f,u} A_{ref}} \tag{6.6}$$

$$\dot{\omega}_f = \frac{\mathcal{F}}{E} \dot{\omega}_{f,LES} \tag{6.7}$$

As reported by Dave et al. [44], the introduction of hydrogen to the combustor significantly changes the structure of the flame. In order to study whether there is significant change in stretch of the flame front, the stretch factor I_0 is computed according to Equation 6.8, where GCS_0 and A_0 is the laminar global consumption speed and laminar flame surface area of a identical perfectly premixed flame in this combustor, as computed by Cantera [80].

$$I_0 = \frac{GCS}{GCS_0} \frac{A_0}{A} \tag{6.8}$$

Note that $A_0 = 0.074^2 \pi \, m^2$, where 0.074 is the radius of the combustion chamber. This value, however, does not serve as a good reference for the calculation of the I_0 as it does not represent the same turbulent flame simulated in this combustor. Ideally, an equivalent, wrinkle free laminar flame would be created that closely matched the geometry of the real flame, allowing for the calculation of a representative laminar flame area and laminar flame consumption speed. This analysis is out of the scope of this project, and the values of I_0 should not be taken at face value but should instead be used as a metric to evaluate the change in flame stretch between cases.

Additionally, because of the simplistic choice of definition of pPV, defining the flame front with $pPV = 0.5$ does not exactly mean the values are obtained when 50% of the reactants have reacted, however due to the low resolution of the flame front, it can be said that this lack of monotony still allows the total consumption rate over the flame surface to be captured this way. Nevertheless, this is still a point to consider alongside the results.

6.1. Measure Reynolds number

It was noted that the applicability of the Werner and Wengle wall model is dependent on the Reynolds number Re. Breuer et al. [107] validated the model and found a good agreement in results for $Re = 10935$, with deteriorating results for lower values of Re. This observation is also backed by similar studies [106]. To evaluate the current regime, a representative Re number based on the velocity magnitude and the injection tube diameter is computed. Note that it was chosen to use the magnitude velocity instead of the bulk velocity to account for the swirl component of the velocity, which is the effective velocity that the near wall stream is subject to. The final relation is given in Equation 6.9

$$Re = \frac{\rho \, D_{tube}}{\mu} \sqrt{U_x^2 + U_y^2 + U_z^2} \tag{6.9}$$

7

Results

In this section, several of the studied metrics are presented and commented on to provide a basis for answering the main research questions. When explicitly mentioned, the data is averaged in time between $t = 0.1$ s and $t = 0.125$ s using 25 solution points equally spaced in time. Any other changes to the data points presented are mentioned in the respective section.

7.1. Convergence behaviour and allotted computational budget

In order to properly ignite the flame and achieve a self sustained combustion, the boundary conditions of the simulation, specifically the injected droplet temperature, are changed in a discrete manner from 450 K at ignition until 300 K, at roughly $t = 0.05$ s. These steps in injected droplet temperature are done at approximately the same time for both cases, however, some care is taken to ensure each simulation has achieved some convergence in the liquid evaporation rate before changing the droplet temperature. In order to do so, the spray penetration, measured as the distance between the furthest parcel and the injector, and the parcel count are monitored at each time step. The second derivative in time of the parcel count is computed to assess whether the evaporation rate has stabilized, since this metric can reliably indicate whether the drop count reaches a $plateau$ or increases monotonically, both of which may indicate convergence in the evaporation rate. The monitored quantities for case A are shown in Figure 7.1 and for case B are shown in Figure 7.2.

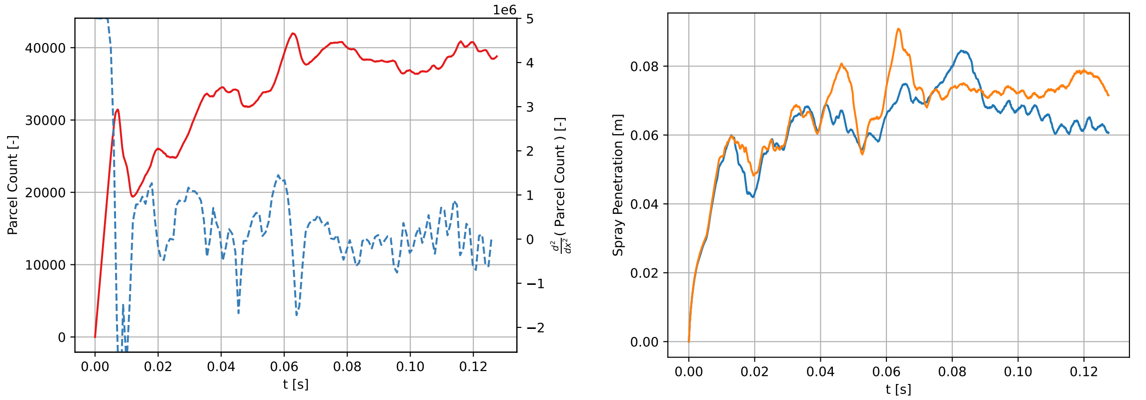

(a) Total Parcel Count (red) and second derivative of Parcel count with respect to time (blue) plotted over simulation time t.

(b) Spray penetration of each injector plotted over simulation time t. Line colours identify the source of the parcel; the orange line matches the positive y-positioned injector, and the blue line matches the negative y-positioned injector.

Figure 7.1: Convergence data on droplet evaporation and spray penetration development, case A.

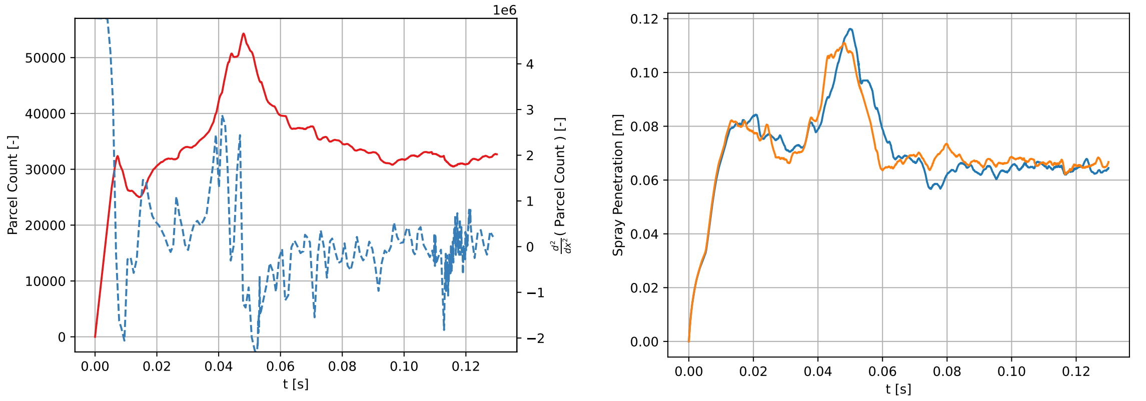

(a) Parcel Count (red) and second derivative of Parcel count with respect to time (blue) plotted over simulation time t.

(b) Spray penetration of each injector plotted over simulation time t. Line colours identify the source of the parcel; the orange line matches the positive y-positioned injector, and the blue line matches the negative y-positioned injector.

Figure 7.2: Convergence data on droplet evaporation and spray cone development, case B.

The monitored spray parcel count shows that for both case A and case B, convergence on spray droplet evaporation and penetration is achieved at $t = 0.08$ s. Figure 7.2 shows the spray penetration is almost constant after $t = 0.08$ s, which is also reflected in a parcel count that stays relatively constant in time. On the other hand, Figure 7.1 also does exhibit some convergence in spray penetration and parcel count over time after $t = 0.09$ s, however a noticeable difference in spray penetration between both injectors reveals some of the effects of the small total simulation time and the effect that the cold flow transient can have on the initial stages of this simulation. This is not to say that the flame has become fully developed, and it likely has not. This verification shows that the spray cone and droplet evaporation behaviour from $t = 0.1$ s to $t = 0.125$ s is stable and does not change significantly over the time frame in which the solutions are extracted.

Due to limitations in the shared computational resources used for the simulations, both case A and case B were run over a period of several days at the High Powered Computational Center nmr. 12 (HPC12) [85] and the DelftBlue Computational Center [86], according to available resources. The simulation was either partially run on the Delftblue Computational Center, where a total of 960, 2x Intel XEON E5-6448Y 32C 2.1GHz CPU cores were used for the computations, or was partially run on the HPC12, where an average of 700 cores AMD EPYC 9354P CPU cores were used for the computations. The active runtime, not accounting for node-availability waiting periods, is computed from the computational statistics. The estimated core hours assume that the simulations were executed on HPC12 using the average number of cores. The total runtime is apportioned between the two computational centres according to a representative time ratio, defined by the ratio of CPUs used at each centre. The core hours are accumulated as this analysis is more valid over the total set of simulations and are rounded to the nearest unit. Both metrics are given in Table 7.1.

Table 7.1: Accumulated simulation time for each case and estimated core hours. Each case is broken down into the respective RANS and LES simulations and the cold flow and combustion simulations.

	Case A		Case B	
Simulations	Total Time	Core hours	Total Time	Core hours
RANS ColdFlow	3D:15hr:45min	322403	0D:17hr:28min	550574
LES ColdFlow	2D:0hr:20min		7D:8h:23min	
LES Combustion	11D:18hr:24min		15D:19hr:41min	

Note that the times in Table 7.1 are indicative of the computational resources used and not of the simulation complexity, as both computational centres used have different processor speeds and available shared memory for the computations.

7.2. Mesh quality

To evaluate mesh quality, Pope [61] proposed a conceptual measure of turbulence resolution based on the relative weight of the SGS kinetic energy with respect to the total kinetic energy, the M criterion. This value is computed using Equation 7.1 and plotted for every cell in the mesh, resulting in the surfaces seen in Equation 7.1. Additionally, the Courant–Friedrichs–Lewy(CFL) number, computed by CONVERGE as the maximum velocity CFL in any of the three orthogonal directions calculated for all the cells in the mesh, is presented as a $z = 0$ slice contour of the combustor in Figure 7.3.

$$M(x,t) \equiv \frac{k_r(x,t)}{k_r(x,t) + K(x,t)} \tag{7.1}$$

$$K(x,t) = \frac{1}{2}\left((u-\bar{u})^2 + (v-\bar{v})^2 + (w-\bar{w})^2\right) \tag{7.2}$$

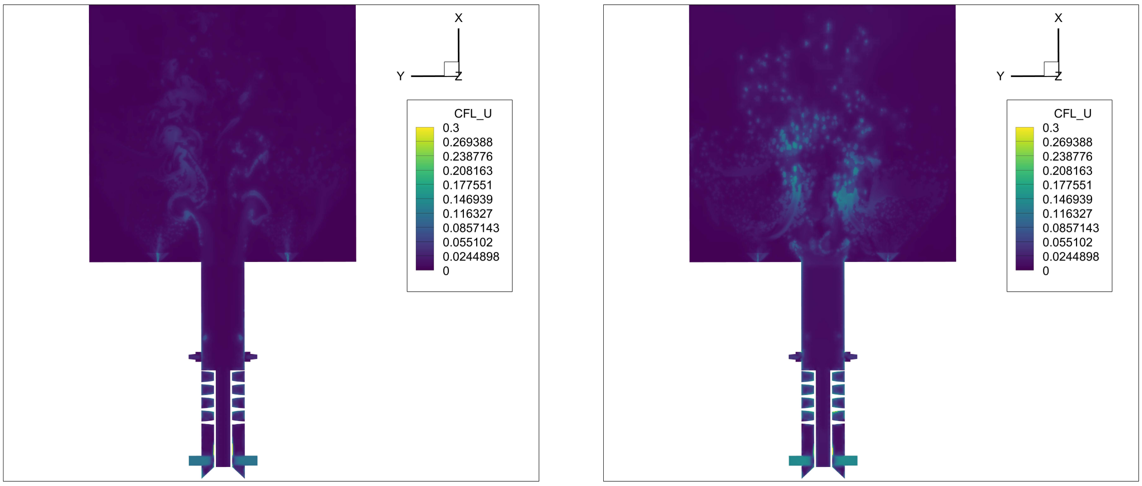

(a) case A.

(b) case B.

Figure 7.3: Z=0, CFL value contour on a xy slice plane for both cases, $t = 0.125$ s. Contour scale is limited to 0 to 0.3 to aid in the visualization of the value distribution.

The CFL distribution shows that, for most cells, the CFL value remains low in these simulations relative to other similar simulations reported in the current literature. Peaks in CFL are seen near the flame front and near the air injection tube, although even in these regions the CFL does not exceed 0.3. The sharp angles of this combustor result in cells that have CFL close to or equal to unity, however, these cells are located near the air injection port and represent an insignificant portion of the total cell count, making it such that the CFL condition for accurate description of fluid flow between cells is preserved with good certainty.

In the original paper, Pope [61] defined that the turbulence resolution tolerance ϵ_m should equal 20% (or $M = 0.2$) or less for an accurate description of the turbulent structures in LES. The analysis is analogous for both cases and Figure 7.4 shows that most of the main combustion area[1] has a M criterion far below 0.2, not only satisfying the requirement for mesh resolution but also making it such that the turbulent scales around the flame structures are being resolved for smaller scales than needed to achieve ”physical” LES.

It can be noted in Figure 7.4a that the injector column, more specifically the swirler and the AAI tube, is characterized by zones of high M,as higher and higher energy turbulent structures get modelled incorrectly using information about scales above a filter that is too big. These areas are characterized by a large mesh size that is not corrected by any of the AMR refinement measures undertaken, resulting in an overly smoothed flow field. However, it can be observed that this holds only up to the end of the

---

[1] refer to section 4.1 for definition of imposed mesh areas

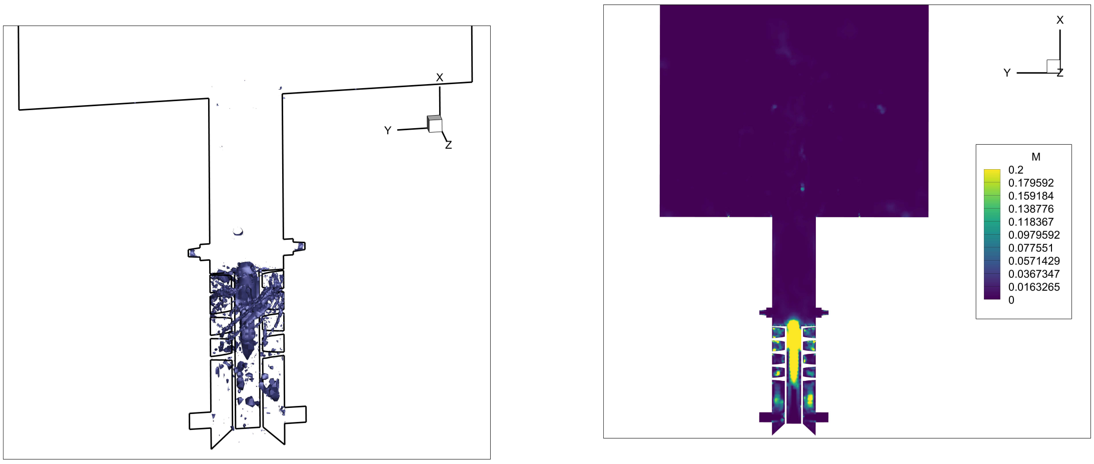

(a) Iso surface for $M = 0.2$

(b) Z=0, xy plane slice of the combustor and the M value for each cell. Scale limited from $M = 0$ to $M = 0.2$

Figure 7.4: Pope's M criterion distribution over the mesh, $t = 0.125$ s.

swirler and before the H_2 injection port, and thus the correct modelling of the scales is compromised only up to this point. It is recognised that the accuracy of this analysis for each case against its respective experimental counterparts is compromised by the improper modelling of the sub-grid scale fluxes in certain sections of the swirler and the AAI injection tube, which will predictably affect the accuracy of the mixing quality between air and hydrogen. However, since the correct modelling of the sub-grid scales past the swirler is ensured in the remaining main combustion area, it is argued that the simulation of the relevant phenomena studied from this point onwards is preserved, and that the study of the mixing quality between the two fuels should not be significantly impacted.

Finally, the Reynolds number is computed using Equation 6.9 at the injection tube and is used to evaluate the applicability of the Werner and Wengle model. The analysis in Figure 7.5 shows that the walls of the injection tube are subject to $Re \sim \mathcal{O}(10^4)$, which is within the validated ranges for this model.

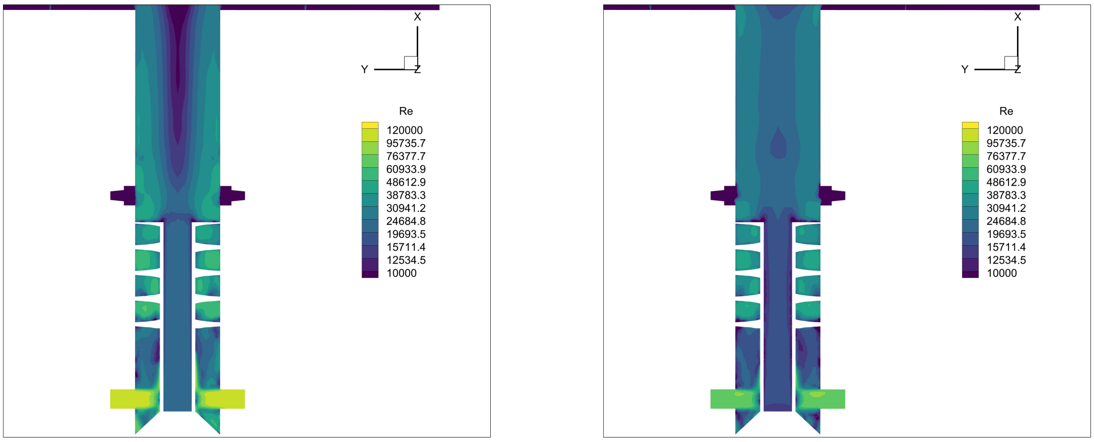

(a) case A, $t = 0.125\,s$

(b) case B, $t = 0.125\,s$

Figure 7.5: $z = 0$ slice of the computed Re variable. Discrete contour uses a logarithmic scale and values are limited from $Re = 1000$ to $Re = 120000$.

7.3. Analysis of pollutant emissions

In this section, the distribution of species in the combustor is studied along x in order to capture and understand any differences in how these species are formed and transformed. For the computation of end of flame emissions, an analysis of the averaged mass-weighted mass fraction of each species is performed for several values of x, relevant observations are drawn, and a location for the final measurement of the pollutant species is chosen. For the analysis of the distribution of reaction zones and how the species mass fraction changes in a plane that intersects the $C_{12}H_{23}$ injectors ($z = 0$), the cross-sectional analysis of the distribution of species is performed over four relevant x values.

7.3.1. Axial trend of species' mass fractions

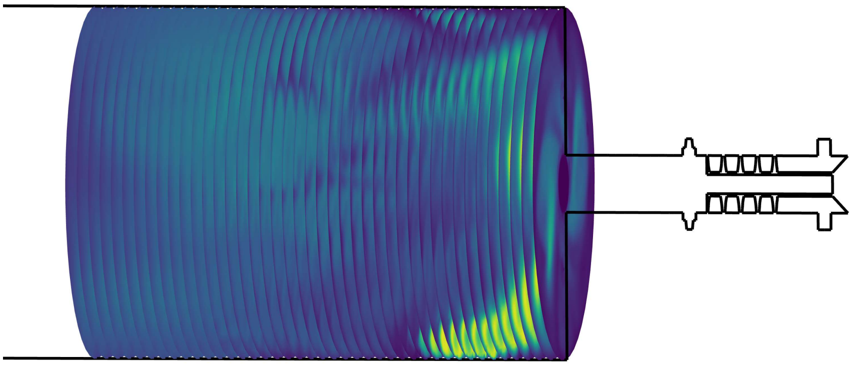

Figure 7.6: Representation of the distribution of slicing x planes across the domain.

The relevant emissions studied here, H_2O, soot, NO_X, and fast chemistry species such as CO and OH are plotted along the axis of the combustor. In this analysis, 40 small volumes of dx created around plane slices are spaced equally from $x = 0.01$ m to $x = 0.2$ m (as visualized in Figure 7.6) and the mass-weighted mass fraction average for each species is plotted along x. Since the lack of sufficient computational resources does not allow for the simulation of a sufficiently long period of simulation time, and consequentially, does allow for the species to traverse the entire combustor length, the data cannot be measured at the outlet and needs to be filtered in order to exclude the analysis of emissions not characteristic of the final flame structure. In order to satisfy this requirement, the data is cropped up to $x = 0.125$ m and the results shown in Figure 7.7, Figure 7.8, Figure 7.9, Figure 7.10 and Figure 7.11 capture the mass fraction of each species as if they were completely mixed in each of the volumes.

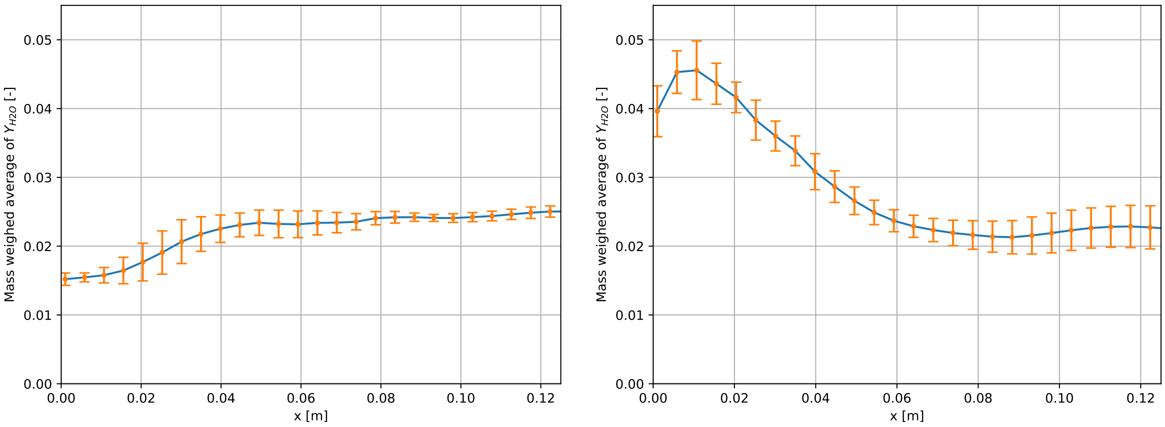

(a) Case A.

(b) Case B.

Figure 7.7: mass-weighted averaged of Y_{H_2O} over equidistant planes from $x = 0.001$ m to $x = 0.125$ m for both cases plotted in blue. The standard deviation (from time averaging) for each plane is plotted in orange for each data point.

As seen in Figure 7.7, the behaviour of the measured quantities over x is quite different, as Y_{H_2O} in case A increases with x until reaching a plateau, and in case B, Y_{H_2O} decreases with x until reaching another plateau. While this would suggest a completely different and contradictory behaviour between the reaction kinetics of both cases, in actuality, it is most likely explained by the differences in the flow field and in the measurement method used. Emissions are measured using mass fraction as a way to quantify the pollutant concentration relative to the amount of reactants injected and products produced. The analysis performed by placing a dx volume and computing the mass-weighted average of any species' mass fraction is roughly analogous to obtaining the value of that species' mass fraction if it were well stirred in that same volume. Since this volume captures recirculation zones and zones far away from the reaction zone, the measurements are influenced by how much of the volume probed is characterised by reaction, product rich and reactant rich zones. A *a priori* study of the flame structure and relevant reaction zones (see section 7.6) reveals that in case A, the first few volumes close to the injector capture far more of the reactant rich zones than product rich zones, leading to a Y_{H_2O} measurement that increases in x as volumes placed further downstream intersect larger reaction zones and eventually account for the combustion of all the fuel. In contrast, case B shows a flame that is shorter and wider, with significant recirculation zones close to the injector, making it such that the same first few volumes close to the injector capture far more of the product rich zones than reactant rich zones, leading to a Y_{H_2O} measurement that decreases in x as volumes placed further downstream take into account the mixing of unreacted air. Note however that despite this behaviour, a correct placement of the measuring volume such that it equally weighs all the reacted fuel against all the injected reactants and produced products between both reactions should predictably yield the same measurements of primary reaction products between both cases as the fuel mass flow rates are the same, which is also what is observed in Figure 7.7 as the Y_{H_2O} value at $x = 0.11$ m is roughly the same.

This analysis is relevant for the remaining figures (Figure 7.8, Figure 7.9, Figure 7.10, and Figure 7.11) as the measurement strategy is the same for all of them. It is then important to highlight that the values of measured Y_m for any species m for the points preceding each respective *plateau* in the data are not independent from the aforementioned phenomena that may skew results. As such, only the final value of Y_m after the *plateau* of the line plot and the Y_m trend in x can be used for any relevant analysis.

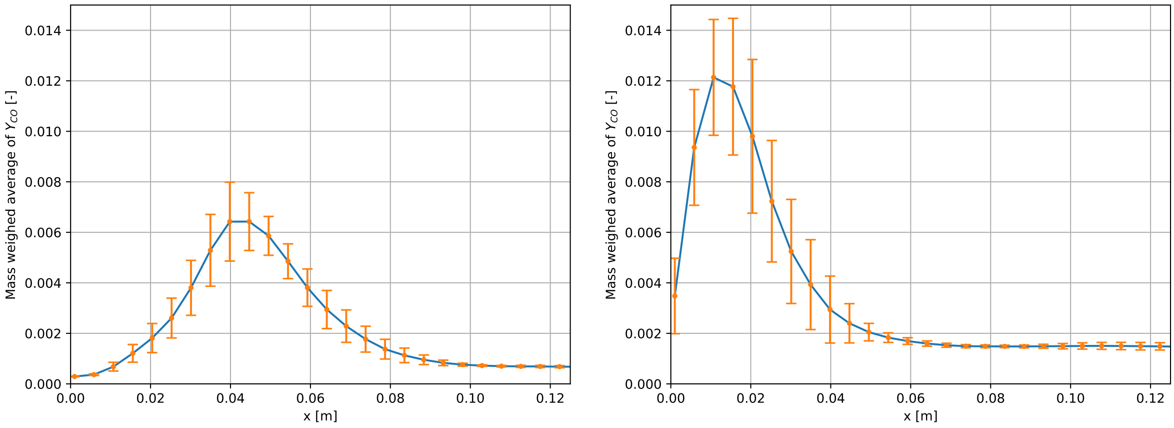

(a) Case A.

(b) Case B.

Figure 7.8: mass-weighted averaged of Y_{CO} over equidistant planes from $x = 0.001$ m to $x = 0.125$ m for both cases plotted in blue. The standard deviation (from time averaging) for each plane is plotted in orange.

From the analysis of fast chemistry species in Figure 7.8 and Figure 7.9, it can be seen that the high reaction zones can be found anywhere as early as between $x = 0.01$ m and $x = 0.05$ m in either flame. The difference in the location of species mass fraction maxima, with steep increases in concentrations of both OH and CO for the spatial and time average at $x \approx 0.025$ m for case A and at $x \approx 0.01$ m for case B, is indicative of significant differences in the flame structure but not conclusive of the flame anchoring distance, as the measurements close to the flame are still influenced by the existence of recirculation zones.

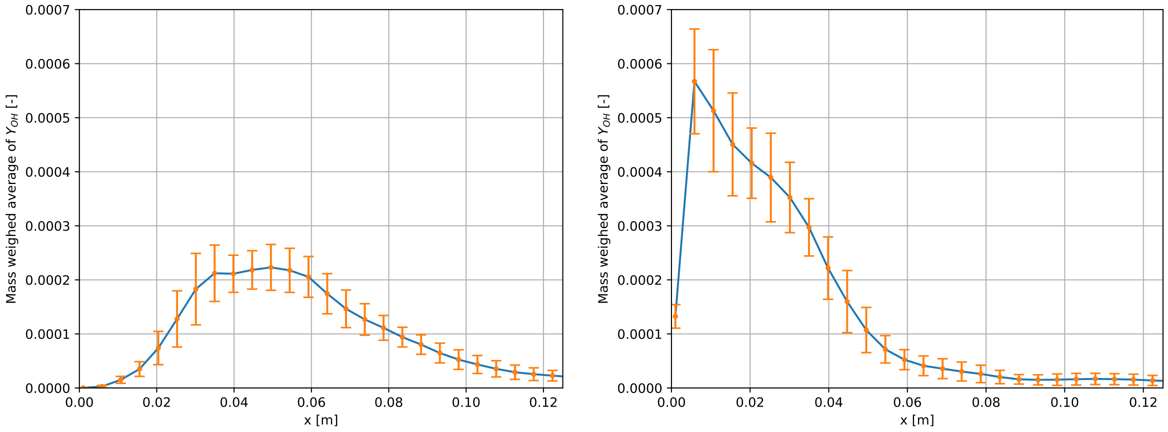

(a) Case A.

(b) Case B.

Figure 7.9: mass-weighted averaged of Y_{OH} over equidistant planes from $x = 0.001$ m to $x = 0.125$ m for both cases plotted in blue. The standard deviation (from time averaging) for each plane is plotted in orange.

Further downstream of the flame, it can be seen that both secondary species rapidly converge to a *plateau* up to $x = 0.125$ m, which is also characteristic and expected as these species are unstable and react back into more stable species right after the local temperature drops. Additionally, OH appears to converge more slowly towards this equilibrium than CO, despite similar standard deviations relative to their values. It could be reasoned that the value of the mass fraction of OH, which is ten times lower than that of CO in this analysis, makes this species much more susceptible to variations from the reaction of other more concentrated species, making OH a more sensitive metric for the existence of reaction zones.

Furthermore, Figure 7.9 and Figure 7.8 show that the standard deviation in the time averaging remains significantly high until each of the species in each of the cases plateaus (in general, roughly after $x = 0.1$ m). This behaviour can be attributed to the combined effects of recirculation zones and reaction zones. Unfortunately, due to the presence of both phenomena and the aforementioned issue with the unreliability of Ym values obtained before $x = 0.11$ m, further observations on the formation mechanisms for each case and each species cannot be extracted from this analysis alone.

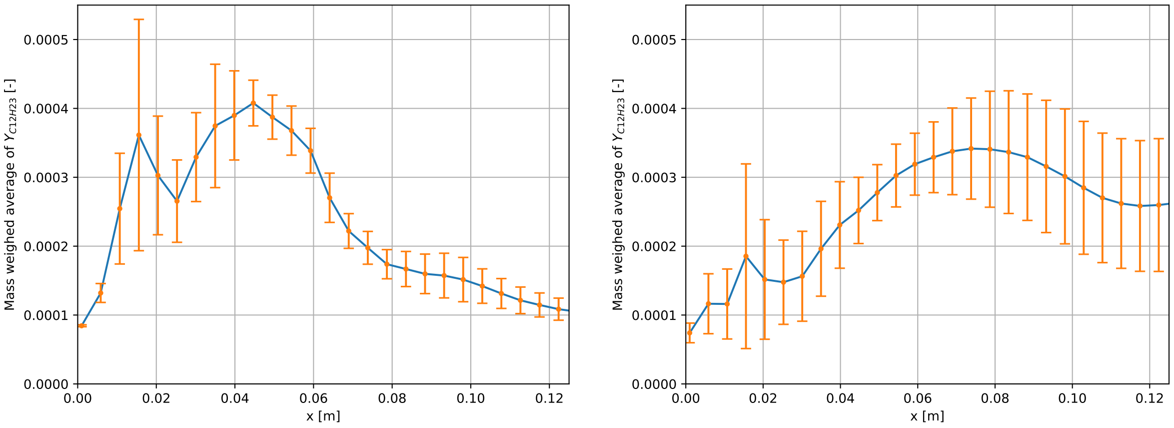

(a) Case A.

(b) Case B.

Figure 7.10: mass-weighted averaged of $Y_{C_{12}H_{23}}$ over equidistant planes from $x = 0.001$ m to $x = 0.125$ m for both cases plotted in blue. The standard deviation (from time averaging) for each plane is plotted in orange.

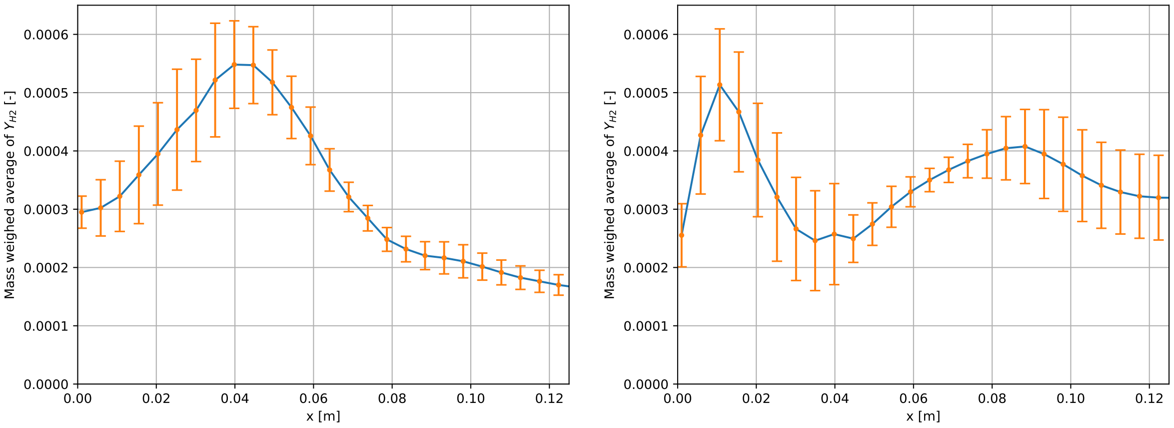

(a) Case A.

(b) Case B.

Figure 7.11: mass-weighted averaged of Y_{H_2} over equidistant planes from $x = 0.001$ m to $x = 0.125$ m for both cases plotted in blue. The standard deviation (from time averaging) for each plane is plotted in orange.

Finally, it can also be seen in Figure 7.10 that the averaged $C_{12}H_{23}$ mass fractions follow roughly the same trend in x between both cases. The first local maxima at $x \approx 0.015$ m in both cases likely corresponds to an increase in local temperature, as the evaporation rate of $C_{12}H_{23}$ droplets spikes. The similarity of the location of these two local maxima suggests that the distance at which the flame anchors does not significantly change between simulations, as the aforementioned recirculation zones are not rich in reactants to significantly impact these measurements. The behaviour of this species after $x \approx 0.02$ m is notably different, however, and reveals how the flame structure might affect the reaction efficiency. Whereas in case A, the $C_{12}H_{23}$ seems to evaporate and react well within the previously observed reaction zones, leading to most of the fuel reacting or dissociating into other species, in case B, the evaporation of $C_{12}H_{23}$ is not followed by the appropriate reaction rate of this species, leading to the downstream accumulation of $C_{12}H_{23}$ as $Y_{C_{12}H_{23}}$ at $x = 0.11$ m in case A is almost three times as lower than the $Y_{C_{12}H_{23}}$ in case B. It could be that the effect of higher inlet temperatures on the flame structure and the subsequent concentration of high temperature zones close to the injector might inadvertently reduce the combustion efficiency and increase UHC emissions. However, once more, it is ambiguous whether this is merely due to the effect of changes in fuel mixing quality or also a direct consequence of different inlet bulk velocities, and whether $Y_{C_{12}H_{23}}$ can accurately represent Y_{UHC}, requiring further studies for a definite conclusion.

Contrary to $C_{12}H_{23}$, H_2 is injected in a gaseous state and also gets produced at a comparable rate through $C_{12}H_{23}$ dissociation reactions. The counter-intuitive initial rise in H_2 seen in Figure 7.11 can be interpreted as a result of dissociation and consequent oxidation of H atoms from the unburned hydrocarbons. Predictably, with the increase in axial distance, this produced H_2, alongside some of the injected H_2, mix and significantly reacts with $C_{12}H_{23}$. The steep climb in H_2 mass fraction that follows the accumulation of $C_{12}H_{23}$ past $x = 0.04$ m in case B has been observed to be a result from both the accumulation of unreacted injected H_2 and the oxidation of H atoms after the flame front, and as such, the different behaviour between case A and case B can be strongly linked to the different behaviour of $Y_{C_{12}H_{23}}$ between both cases and the attributed explanation. That is, the lack of the same rise in H_2 mass fraction over the same range of axial coordinates in case A can also be attributed to more of the injected $C_{12}H_{23}$ burning along side the H_2.

Finally, it was discussed in chapter 5 that the modelling of NO_x and soot made it such that the spatial distribution of these species might not be physical and only the far field results should be evaluated. However, a short analysis of the mass-weighted distribution of these species with x presented in Figure B.1 and Figure B.2 (Appendix B) allows for the changes of final emissions measurement location to be evaluated, where it is seen that soot mass fraction does not significantly change with x near $x = 0.11$ m and NO_x only weakly changes with x near $x = 0.11$ m.

7.3.2. End of flame emissions

Based on the infinitesimal volume analysis done in subsection 7.3.1, it can be understood that measuring the emissions within the refined main combustion area (up until $x = 0.15$m) is not straightforward. Fast reacting species reach a *plateau* at $x \approx 0.11$ m, and a control volume after this point could capture a portion of the flow representative of the far field flow resulting from this flame. In order to measure emissions that are representative of the far field emissions for both cases, a volume is picked that is close enough to the flame but does not intersect any significantly high reaction zones, nor is positioned too far away from the flame. Additionally, it is chosen to use a $\Delta x = 0.02$ m for the volume in order to obtain a less flow field dependent averaging of the mass fractions. The final volume is centred at $x = 0.12$ m and the results on species mass fraction are mass-weighted averaged in order to measure a well mixed volume. The final results are time averaged between $t = 0.1$ s and $t = 0.125$ s and are given in Table 7.2.

Table 7.2: Results from mass-weighted averaging of volume from $x = 0.1$ m to $X = 0.13$, Y is the average of the mass-weighted mass fraction average, and ”Std. deviation” is the standard deviation of the time averaging.

	Case A		Case B	
Species	Y	Std. deviation	Y	Std. deviation
H_2O	$2.2581 \cdot 10^{-2}$	$9.6719 \cdot 10^{-4}$	$2.1023 \cdot 10^{-2}$	$2.7751 \cdot 10^{-3}$
CO_2	$3.4619 \cdot 10^{-2}$	$2.3772 \cdot 10^{-3}$	$2.7293 \cdot 10^{-2}$	$5.1655 \cdot 10^{-3}$
NOx	$8.8068 \cdot 10^{-4}$	$2.0931 \cdot 10^{-5}$	$6.3861 \cdot 10^{-4}$	$4.5428 \cdot 10^{-5}$
Soot	$3.0204 \cdot 10^{-5}$	$4.5446 \cdot 10^{-6}$	$3.4535 \cdot 10^{-5}$	$1.3272 \cdot 10^{-5}$
CO	$6.4071 \cdot 10^{-4}$	$4.6510 \cdot 10^{-5}$	$1.3074 \cdot 10^{-3}$	$1.6328 \cdot 10^{-4}$
OH	$2.8056 \cdot 10^{-5}$	$1.3341 \cdot 10^{-5}$	$1.7493 \cdot 10^{-5}$	$1.0281 \cdot 10^{-5}$

It is immediate that the expected consistency between both cases on emissions is met. The measured mass-weighted mass fractions of CO_2 and H_2O are similar between both cases, with an overlap between the average plus the standard deviation range for case A and case B. Differences in averages are likely attributed to the difference in unreacted fuel quantities, to differences in flow fields that may slightly condition the measurements and due to time fluctuations and insufficient number of solution points used to compute the average. This observation is expected but important to note on the consistency between the studied cases.

An analysis in terms of secondary emissions reveals relevant emission phenomena that closely relate to previous works on hydrogen and $C_{12}H_{23}$ mixing. It can be observed that a significant and definite drop in CO species concentration can be seen from case B to case A, or in other words, with the drop in inlet temperature. This observation is consistent with the existing literature on the mixing of these 2 fuels, which corroborates the improved mixing quality of both fuels with a reduction in inlet temperature. The trend in emissions of OH, soot and NO$_X$, however, is much more ambiguous and hard to draw a definite conclusion on. If changing inlet temperature has any significant impact on fuel mixing quality, then the increase of mean soot mass fraction from case A to case B is consistent with literature studies on fuel mixing quality, however the standard deviation of these measurements are of the same order as the measurements themselves and create overlapping value ranges between both cases, meaning the observed trend might not be representative of the actual far field emissions. Additionally, the trend observed for OH and NO$_x$ emissions contradicts all the previous observations and the observations from previous literature, since it would be expected that, if changing inlet temperature had any significant impact on fuel mixing quality, then Y_{OH} and Y_{NO_x} should decrease from case B to case A. However, it is reinforced here that, just like soot, the standard deviation associated with the Y_{OH} and with the Y_{NO_x} data from case B is of the same magnitude as the average itself, and it is not conclusive if this trend would hold for the far field emissions. As such, the analysis of any secondary pollutants other than CO is deemed not reliable.

The measurements are likely conditioned by the measurement location and the total simulation time. For case A, it seems that soot, NO$_X$ and OH have quite acceptable standard deviations in time, meaning the measurements are consistent between solution points, however, the opposite is argued for case B, where the data presented for these 3 species cannot be used in any conclusive manner. It is likely that the final emissions need to be measured further downstream, and the simulation needs to be run for longer to achieve more consistent and precise measurements of these pollutants. The measurements of CO are consistent in time, present a clear trend between both cases and serve as a moderate argument for the improvement of fuel mixing quality. However, for the aforementioned reasons, it’s possible that the magnitude by which CO changes with inlet temperature is not as significant as the values in Table 7.2.

7.4. Cross-sectional analysis of the distribution of species

With the intention of further analysing the distribution of species along the length of the combustor, data on the species mass fraction was probed along several y lines at $z = 0$ for $x = 0.005\,\text{m}$, $x = 0.025\,\text{m}$, $x = 0.05\,\text{m}$ and $x = 0.075\,\text{m}$ as illustrated in Figure 7.12. The positioning of these lines is purposefully done such that data before, around, and after the primary reaction zone of the flame structure can be captured. The data is time averaged for the obtained solution points and the results are plotted for H_2 fast chemistry species in Figure 7.13, Figure 7.14 and Figure 7.15, respectively.

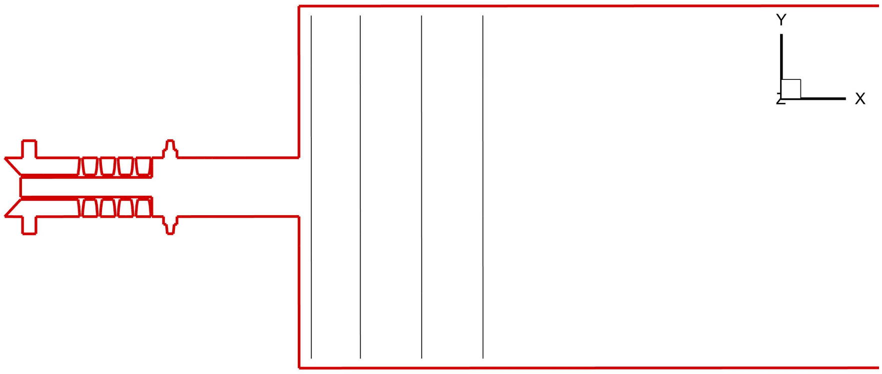

Figure 7.12: Illustration of the positioning of the $z = 0$ lines for the cross-sectional analysis of the distribution of species. The lines are identified in black and the combustor outline is identified in red.

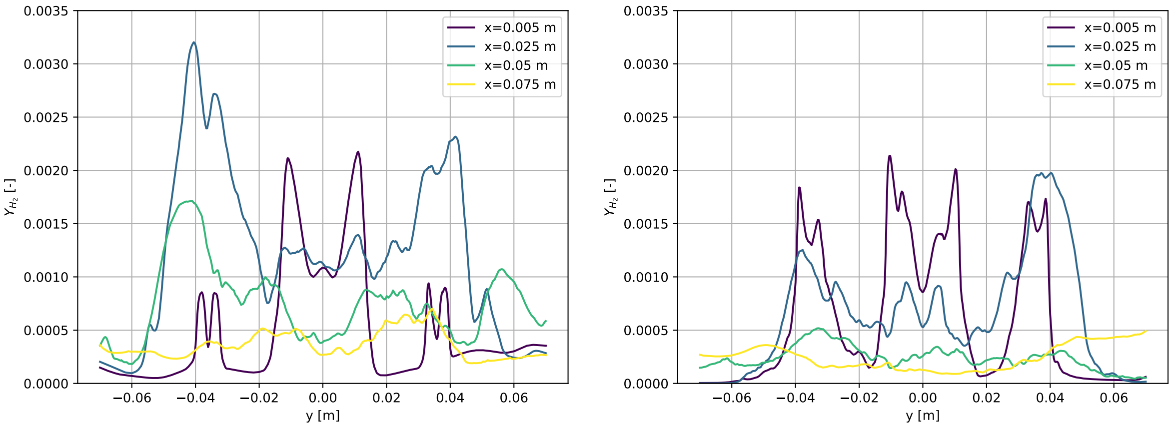

(a) Mass fraction of H_2 plotted for 4 $z = 0$ lines over y, case A.

(b) Mass fraction of H_2 plotted for 4 $z = 0$ lines over y, case B.

Figure 7.13: Y_{H_2} plotted for several precise lines in $z = 0$.

The Y_{H_2} over y is plotted in Figure 7.13, where it can be seen that a peak in Y_{H_2} between $y = \pm 0.01\,\text{m}$ at $x = 0.005\,\text{m}$, associated logically with the injected hydrogen, rapidly decreases with x as H_2 either burns by itself or mixes with the surrounding flame. It can be distinctly observed that the peaks at $x = 0.025\,\text{m}$ and $y = \pm 0.04\,\text{m}$ are of greater magnitude than the Y_{H_2} peaks of injected hydrogen close at the injection port, which confirms the previously expected comparable emissions from the dissociation of $C_{12}H_{23}$ and from direct injection of H_2. The original hypothesis stipulates that the injection of cooled hydrogen/air allows hydrogen to diffuse further downstream before reacting with air or trace amounts of hydrocarbons and, in Figure 7.13, it can be seen that the centre peak of Y_{H_2} between $y = \pm 0.01\,\text{m}$ is characterized by a steeper reduction with x in case B compared to case A. Furthermore, in case B, the overall Y_{H_2} centre peak shrinks in y with x, as opposed to case A where the same centre peak does not significantly shrink in y for the same x lines. Although not definitely conclusive, these two observations strongly suggest that the injected hydrogen flow in case A reacts slower in space than in case B and diffuses further in y and x, allowing for injected hydrogen to potentially reach the primary reaction zones and properly mix with $C_{12}H_{23}$.

On an additional note, the fast decay of Y_{H_2} anywhere between $x = 0.025$ m and $x = 0.05$ m for $y = 0$ indicates the likely existence of a (almost) pure hydrogen reaction zone, which further elaborates the conclusion that the poor fuel mixing in this combustor leads to the formation of a third smaller and less intense reaction zones in the centre of the core flow.

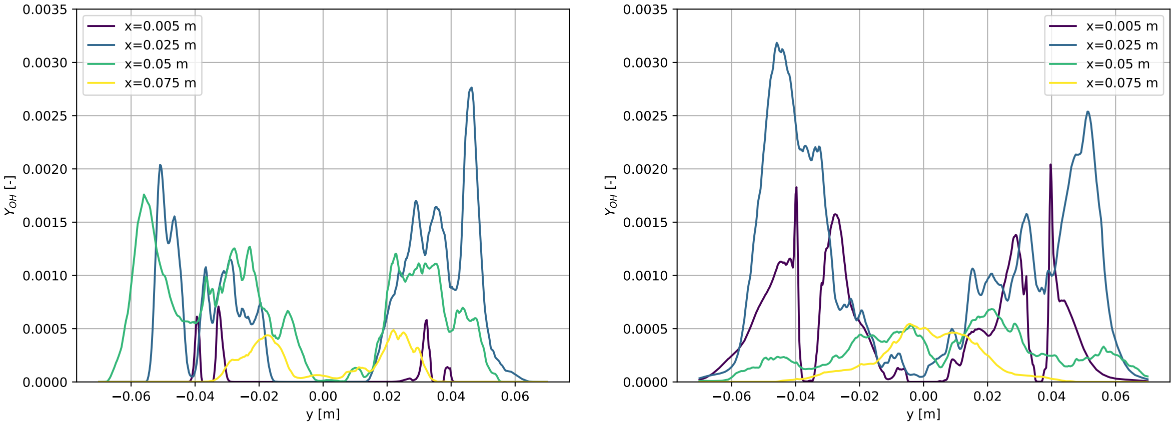

(a) Mass fraction of OH plotted for 4 $z = 0$ lines over y, case A.

(b) Mass fraction of OH plotted for 4 $z = 0$ lines over y, case B.

Figure 7.14: Y_{OH} plotted for several precise lines in $z = 0$.

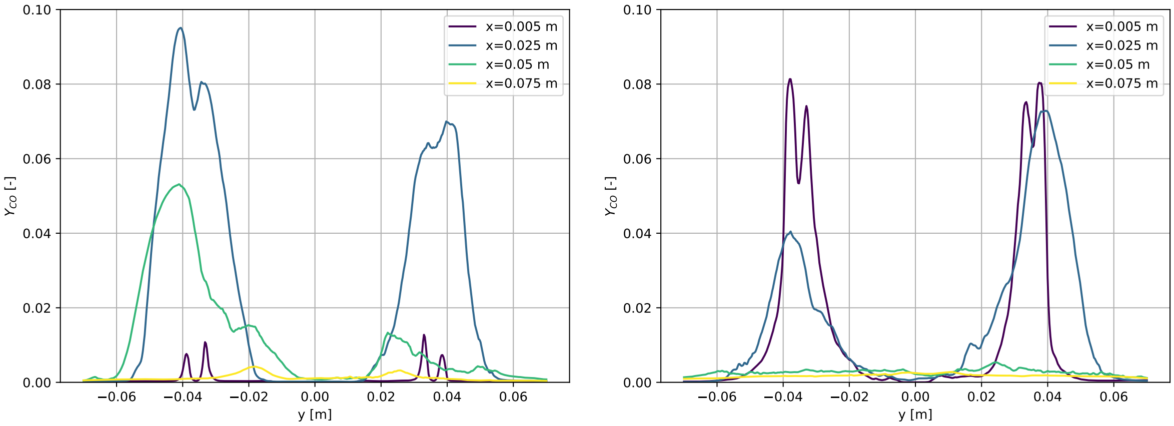

(a) Mass fraction of CO plotted for 4 $z = 0$ lines over y, case A.

(b) Mass fraction of CO plotted for 4 $z = 0$ lines over y, case B.

Figure 7.15: Y_{CO} plotted for several precise lines in $z = 0$.

Fast chemistry species such as OH and CO have their mass fraction distributions plotted in Figure 7.14 and Figure 7.15. It can be observed that the reaction mechanism correctly captures the predicted formation behaviours of CO and OH, whereas the former tends to form at higher rates near the centre of the flame structures where there is a depletion of O atoms and significant dissociation of hydrocarbons can be expected, while the latter tends to form close to the flame front where the temperature is highest and quickly breaks down or gets transformed into other species. The existence of a small and isolated Y_{OH} peak near $y = 0$ shortly after a dip in Y_{H_2} in the same position further corroborates not only the observation that the aforementioned (almost) pure hydrogen reaction zone exists, resulting from the poor fuel premixing, but also that the increase in inlet temperature leads to the rise in the amount of hydrogen that reacts into Y_{OH}, further supporting the hypothesis that the decrease in inlet temperature allows for hydrogen to properly diffuse and mix with $C_{12}H_{23}$. Between both cases, OH and CO data exhibit roughly the same behaviour, with the notable observation that case A shows more spatially distributed species formation zones compared to case B. This supports the plausible observation that, in case B, there might be an over-production of secondary species due to the concentration of most of the reaction zones near the injection area, forming a region of higher temperature when compared to case A. This plausible observation is supported by studies on the axial temperature of shorter and wider swirl flames [91] and the effect of temperature on secondary species formation rate is a well studied phenomena, however this analysis is also limited in the spacing and number of lines used and in the fact that the lines only study the distribution in $z = 0$, which, for instance, does not account for the reaction zones at $y = 0$. It is then suggested that, to draw any conclusions from this observation, further studies are needed.

7.5. Mixing quality

The cell HRR values are extracted and plotted over a [ϕ_{H_2},ϕ_O] grid. The data is limited to equivalence ratios between 0 to 1.5 for ϕ_O and 0 to 0.2 for ϕ_{H_2}. Additionally, zero or negative values of HRR are omitted from this analysis not only as the dispersion of these points do not allow for the creation of a surface along the given grid due to a lack of any grid structure formed by the negative HRR cell value points at higher equivalence ratios, but also because these points are not relevant as they do not characterize heat releasing reaction zones.

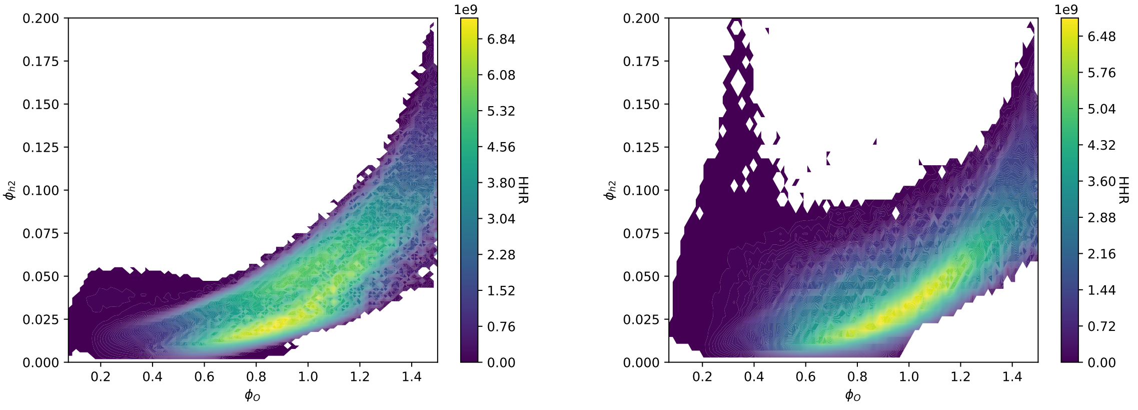

(a) case A.

(b) case B.

Figure 7.16: HRR contour plotted against ϕ_{H_2} and ϕ_O for both studies cases. The contour scale is limited to positive values, and contour regions without data (white) represent values below 0 or missing data.

The HRR contours in Figure 7.16 that is there is a scattering of more than one peak throughout a region between $\phi_O = 0.8$ and $\phi_O = 1.2$, with additional smaller peaks within the same range at higher values of ϕ_{H_2} and other less significant peaks in the remaining regions. It is first important to note that ϕ_O does not match the computed fuel to air equivalence ratio of 0.4, which is expected, as this value is a global metric. One of the additional reasons for this discrepancy is that the definition used for the ϕ_O measures all local carbon and hydrogen atoms to quantify the amount of hydrocarbons and other species that could react exothermally with the existing oxygen, which means that species such as CH_4 and C_2H_4 are also counted as fuel. Additionally, and more relevant to note is that due to the poor mixing of this combustor, the flame is significantly diffusive and there are regions where the flame front forms in the intersection between a fuel rich zone and an oxygen rich zone. The contour of the Takeno index [158] in Figure B.6 (Appendix B), outputted by CONVERGE to measure the flame regime further supports this observation by showing that the primary reaction zones after the injection of $C_{12}H_{23}$ are predominantly diffusive for both cases.

The distribution of positive HRR values follows a "bow" shape, where at low ϕ_O there's a small increase in maximum ϕ_{H_2} regions characterised by exothermic reactions. As ϕ_O increases, the maximum ϕ_{H_2} first until $\phi_O \approx 0.5$ until starting to rise consistently thereafter. Referring to the analysis performed in section 7.4, it is known that a significant amount of H_2 is produced from the dissociation of hydrocarbons in the primary reaction zone when compared to the injected amount of H_2, which makes it difficult to identify the source of the H_2 for a given ϕ_{H_2}. Unfortunately, it is not possible with the current setup to accurately separate the injected H_2 from the H_2 from dissociation reactions. An additional small region of $\phi_O \approx 0.1$ and high ϕ_{H_2} is also present in the graph and although the origin of the hydrogen participating in this reaction also cannot be pinpointed with certainty, it's reasonable to assume it likely is hydrogen concentrated close to the core of the injected air flow that reacts further away from the flame structures formed, as seen the increase in OH following a dip in local hydrogen concentration near $y = 0$ in Figure 7.14.

However, a relevant analysis can be made from the distribution and intensity of HRR peaks. Figure 7.16b shows a concentration of peaks of higher magnitude centred roughly at $\phi_o = 1$ and $\phi_{H_2} = 0.025$. With the injection of colder air and hydrogen in case A, the more intense peaks in Figure 7.16a become significantly more dispersed, but the positive HRR band becomes significantly narrower around

$\phi_{H_2} = 0.025$. The higher magnitude peaks in case A are more closely centred at $\phi_o \approx 0.85$ and are of lower magnitude than the highest magnitude peaks of Figure 7.16b. For case A, the distribution of additional high magnitude peaks extends further into higher ϕ_{H_2} values, but the high ϕ_{H_2}, low ϕ_O HRR peaks are completely eliminated, resulting in the mentioned ”narrowing” of the high HRR ”bow” band. This series of observations strongly suggests that the zones of high ϕ_{H_2}, low ϕ_O and areas of high ϕ_O, low ϕ_{H_2} converge together and form reaction zones that are more well mixed in H_2 and $C_{12}H_{23}$.

7.6. Stretch factor and turbulent structure interactions

The normalised global consumption speed is computed from the time-averaged values obtained from the 25 solution snapshots between $t = 0.1$ s and $t = 0.125$ s for both cases. The results obtained for each of the cases studied are shown in Table 7.3.

Table 7.3: Stretch factor, GCS, and flame area for each of the studied cases. Average and standard deviation obtained from the analysis of 25 consecutive solution points from $t = 0.1$ s to $t = 0.125$ s.

	Case A		Case B	
Variable	Average	Std. deviation	Average	Std. deviation
GCS $[m/s]$	9.5586	2.3790	6.5986	3.3788
A $[m^2]$	0.0419	0.0037	0.0440	0.0055
I_0 $[-]$	70.2468	14.8772	46.6067	21.3595

The analysis of the stretch factor shows that there is an indicative increase in I_0 from case B to case A, although the range of measured I_0 created by the standard deviations makes this analysis uncertain. A plausible increase in stretch factor, however, could be fundamented by the existence of large scale structures and their effect on the local curvature of the flame front associated with the primary reaction zone, a phenomenon that can be seen clearly from the contours of Temperature and H_2 in Figure 7.18 and Figure B.4(Appendix B), respectively. The difference in the formation of these turbulent structures can be partially traced to the lower axial velocity of the air/hydrogen stream when the same mass flow rate of reactants is injected at lower temperatures. The contour of axial velocity in Figure 7.19 shows that in case A, after the injection port, there’s the formation of a more coherent jet structure with lower effective swirl intensity when compared to case B, despite the lower injection velocity, indicating that the stream in case A exhibits a higher axial-to-radial momentum ratio that allows for the formation of large scale structures with a more evident effect on flame curvature. Additionally, from an analysis of the HRR contours in Figure B.5(Appendix B), higher HRR zones can be identified in and around the core air/hydrogen stream right after the injection port, which results in the fast deterioration of the jet structure of the injected air/hydrogen stream and can consequently disturb the formation of these turbulent structures. Since the injection of higher temperature hydrogen can allow the formation of H_2 pilot flames at higher flow-field speeds, and thus closer to the injection port, the formation of turbulent structures is likely partially affected by the existence of these reaction zones and, as such, by injection temperature, although no clear impact of each uncoupled phenomenon can be extracted. Nevertheless, the limited computational resources, resulting in a small total simulation time, is likely a prominent culprit influencing the computation of I_0 and the reduction of uncertainty around this quantitative conclusion, as the flames might not have enough time to reach their stable positions under statistically stable conditions. The combination of both I_0 measurements and flow field interactions with the reaction zone seems to suggest that the flame in case A is subjected to increased flame stretch.

The turbulent interactions, specifically as observed from the Temperature and H_2 contours in the $z = 0$ slice in Figure 7.18 and Figure B.4(Appendix B), could partially explain why the mixing of both fuels is improved by the reduction of inlet temperature. It can be seen that the formation of the relatively H_2 richer jet structure and consequent turbulent structures that significantly interact with the flame front also transport the injected H_2 to the main reaction zone, improving mixing. Figure 7.17 shows that the flame structure changes dramatically between cases A and B, an observation supported by the analysis of the cross-sectional species distribution. Figure 7.17 also reveals that the flame structure from case A is more conical and seems to swirl less around the combustor, although this result cannot be detached from the decrease of the swirl influence on the injected air/hydrogen after the injection port with the decrease of the inlet temperature.

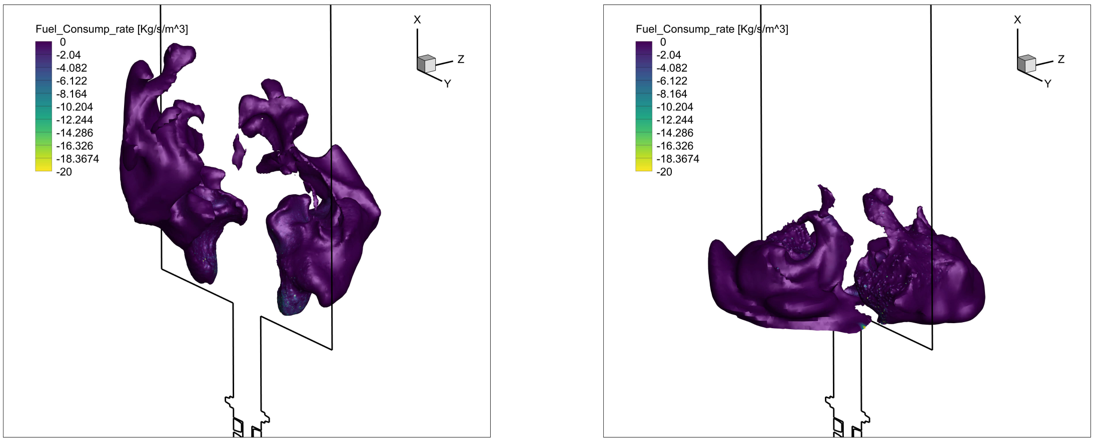

(a) case A, $t = 0.1$ s.

(b) case B,$t = 0.1$ s.

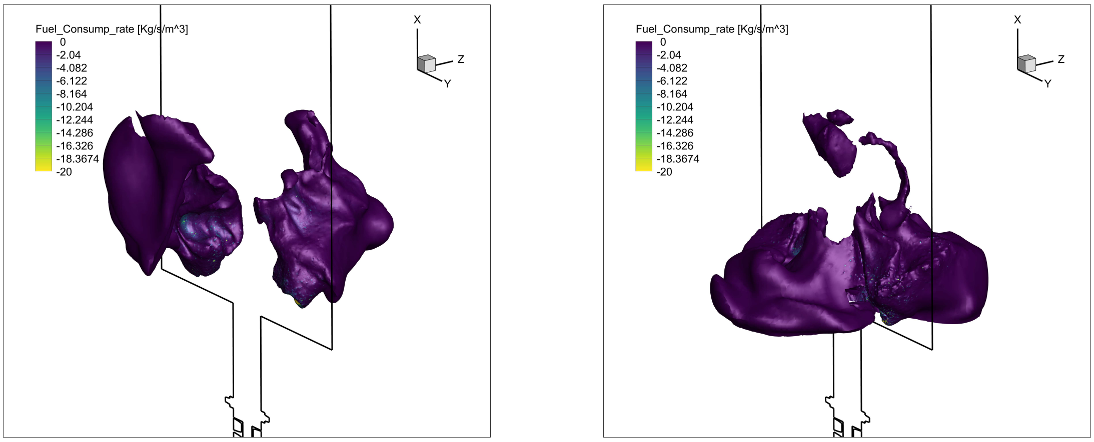

(c) case A, $t = 0.11$ s.

(d) case B, $t = 0.11$ s.

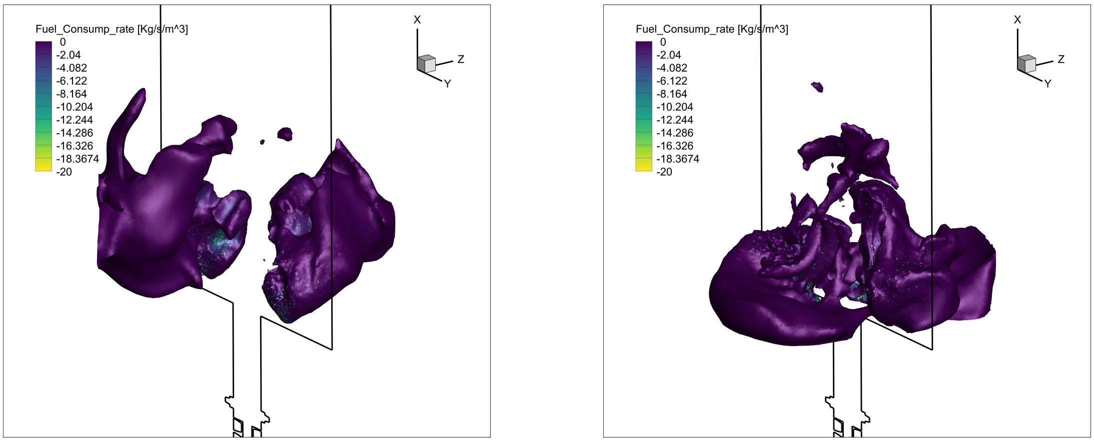

(e) case A, $t = 0.125$ s.

(f) case B, $t = 0.125$ s.

Figure 7.17: $pPV = 0.5$ iso-surface coloured according to the *Fuel_Consump_rate* ($[Kg/m^3/s]$) variable computed by the combined consumption rate of both fuels $\dot{\omega}_w$. Plotted three different relevant solution points for case A and case B.

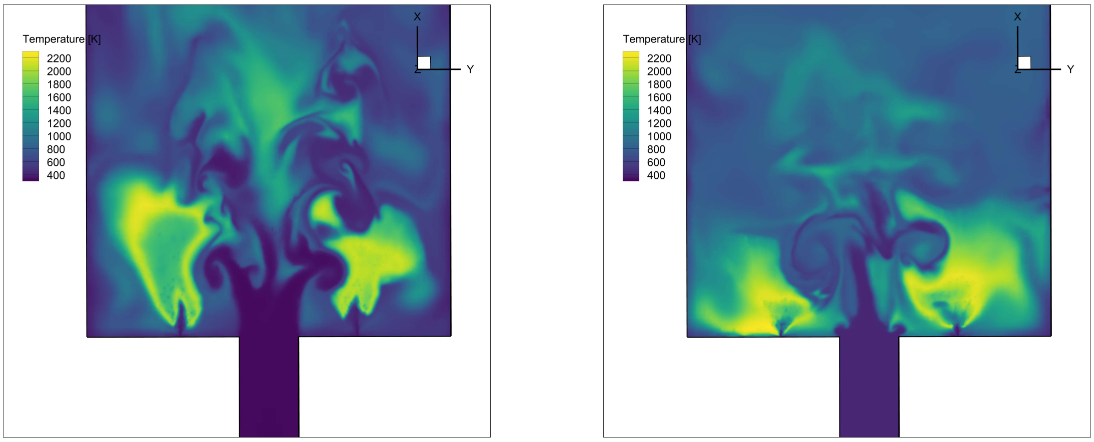

(a) case A, $t = 0.1$ s

(b) case B,$t = 0.1$ s

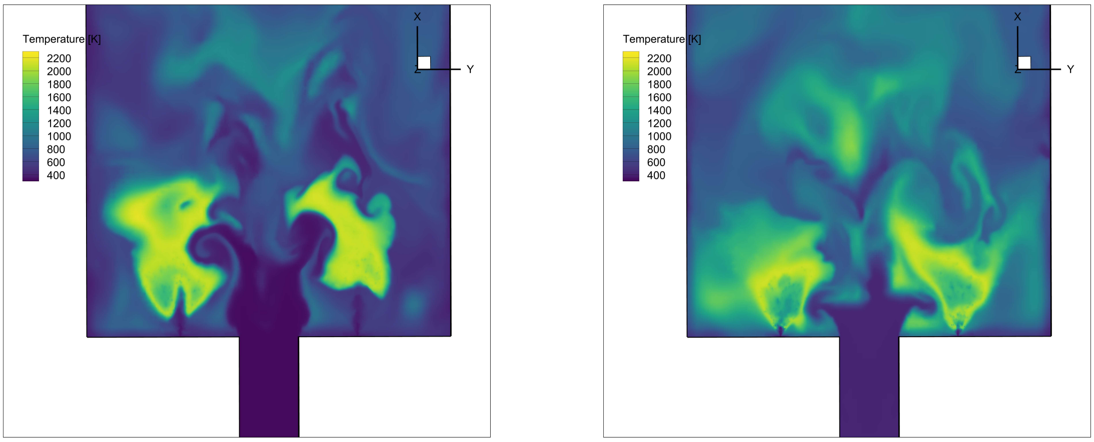

(c) case A, $t = 0.11$ s

(d) case B, $t = 0.11$ s

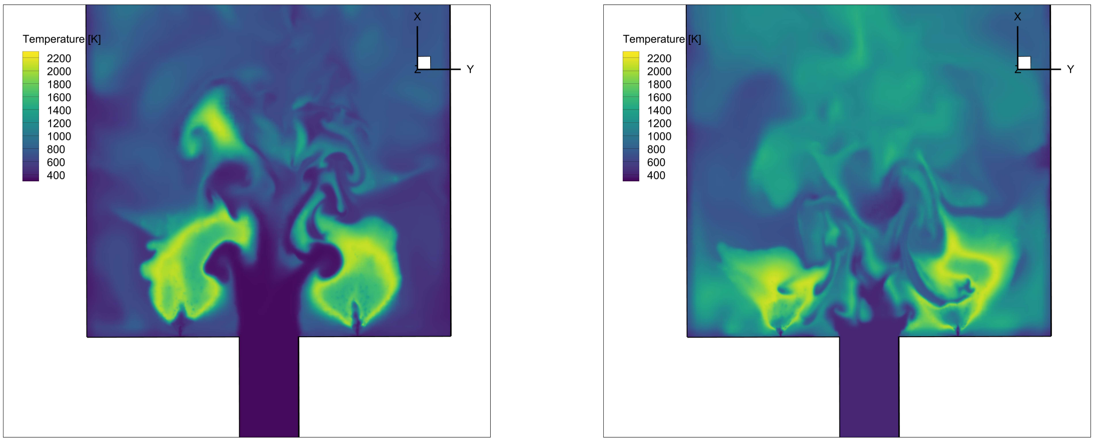

(e) case A, $t = 0.125$ s

(f) case B, $t = 0.125$ s

Figure 7.18: Z=0 slice of the Temperature $[K]$. Plotted for three different relevant solution points for case A and case B.

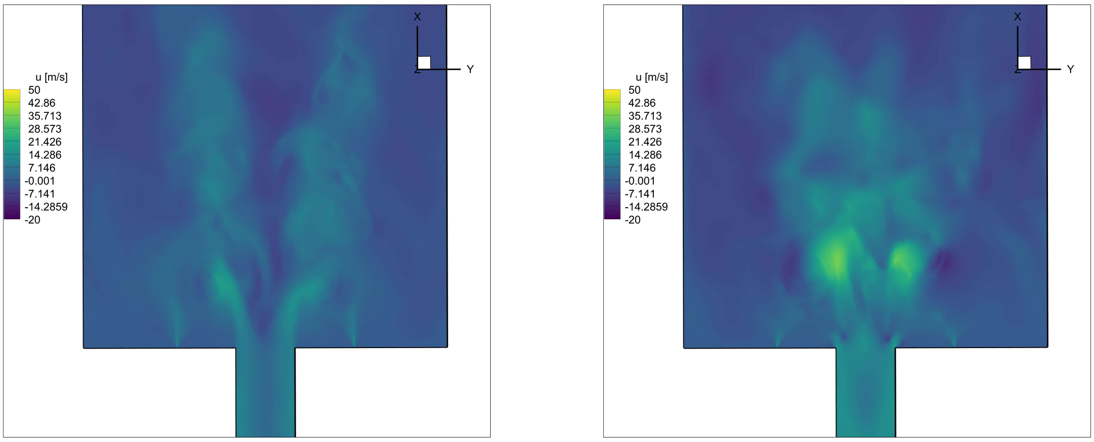

(a) case A, $t = 0.1$ s

(b) case B,$t = 0.1$ s

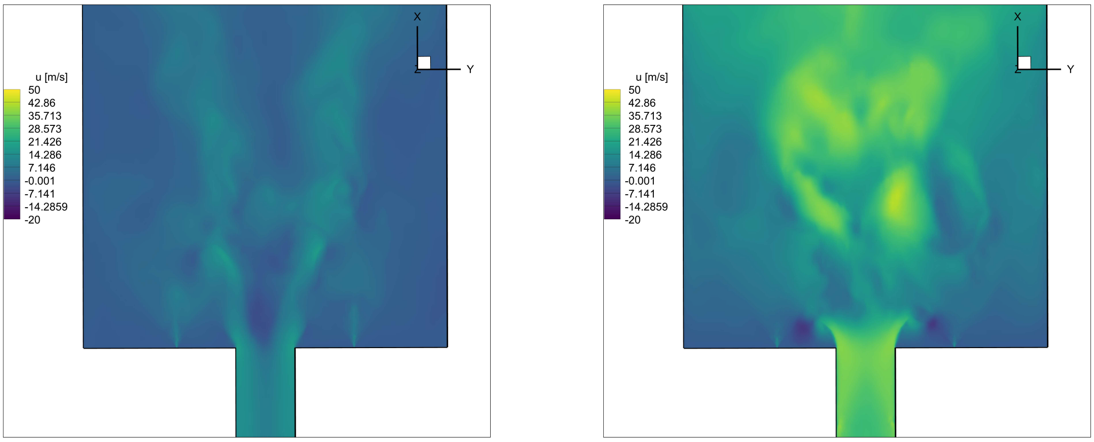

(c) case A, $t = 0.11$ s

(d) case B, $t = 0.11$ s

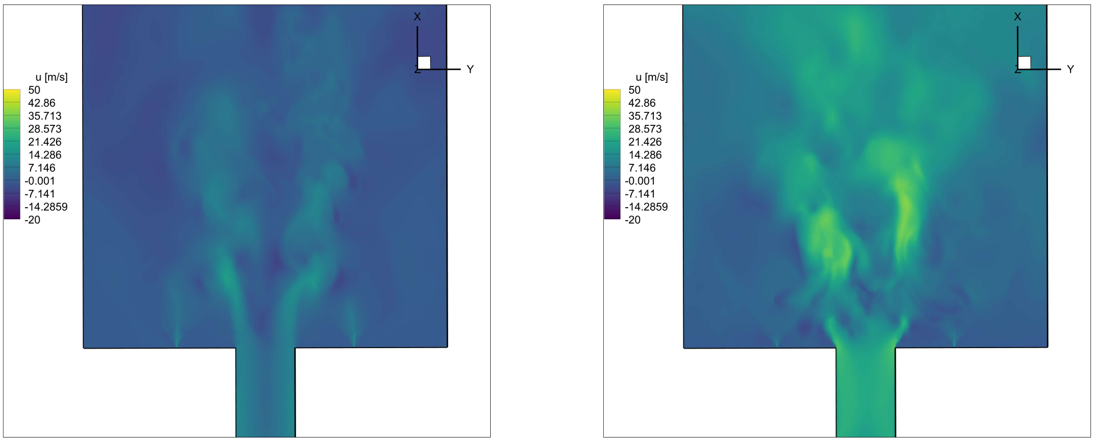

(e) case A, $t = 0.125$ s

(f) case B, $t = 0.125$ s

Figure 7.19: Z=0 slice of the x velocity component $[m/s]$. Plotted three different relevant solution points for case A and case B.

8

Discussion

In this section, the obtained results are analysed beyond the immediate observations made when presenting them, and relevant secondary observations are provided about the work presented. An additional space is created to discuss the applied methodology and its impact on the results, after these have been presented, to further analyse the overall model effect on the results. The proposed research questions are also reviewed in light of the obtained results and the presented analysis.

8.1. Discussion on obtained results

The results show that the implemented modelling strategy for solving the fluid flow field, multiphase interactions, and combustion kinetics is consistent with the expected physical phenomena from the combustion of this fuel blend in this combustor, including the predicted spatial distribution of solved species and reaction zones in the combustor. The lack of validation data casts doubt on the accuracy of the obtained values and whether some of the assumptions made are viable. However, the literature review and the study of the implemented models strongly support the conclusion that the chosen modelling strategy allows the correct modelling of the most relevant phenomena, ensuring that the results presented in this study are representative of the real combustion case.

The mixing quality between the simulated cases is the most strongly supported result from this work. The independent analysis of the mixing quality using the HRR plots in Figure 7.16 shows that there is a distribution of more intense reaction zones towards higher H_2 equivalence ratios and lower overall equivalence ratios, meaning more H_2 is fueling the reaction zones of higher HRR. Although from this analysis it is still not fully clear whether this change is influenced by a possible increase and oxidation of dissociated H atoms into H_2, further analysis from the species distribution over $z = 0$ in Figure 7.13 lines show that the formation of relatively richer H_2 reaction zones near the core of the air/hydrogen injection stream is significantly reduced at lower injection temperatures and, simultaneously, the injected H_2 is transported further into the domain before getting consumed. Additionally, the distribution of OH in Figure 7.14 also suggests a reduction in the quantity of OH being formed in an identified relatively richer H_2 reaction zone near the core of the injected air/hydrogen stream from case B to case A. Both of these observations are in agreement with the hypothesis that cooler H_2 can be used to delay the formation of H_2 rich pilot flames and allow for the proper time for both fuels to mix.

One observation from turbulent interactions with the flame front is that the injection speed may affect fuel mixing quality, in addition to the effect of the lower fuel temperature. The position of large scale structures near the flame characteristic of case A suggests that H_2 is transported over these scales to the flame front, allowing for H_2 to properly mix with $C_{12}H_{23}$. Furthermore, past studies [91] have shown that an increase in flame swirl leads to higher axial temperatures and shorter, wider flame structures. If the decrease in air/hydrogen stream bulk velocity and the formation of more coherent jet streams influence the flame swirl, then the results obtained herein could also be a result of the change in swirl influence on the injected stream. Some conclusions, however, such as the decrease in the intensity of the relatively richer in H_2 reaction zone at the core of the air/hydrogen injection stream in case A, are not consistent with lower stream bulk velocities and indicate that the temperature of the stream is a significant factor in the final results. It is unknown what the exact impact of air/hydrogen stream bulk velocity is relative to the impact of injection temperature is and it is also not known if the H_2 would react before reaching the flame front in case it were injected at the same temperature but at higher injection speeds, however it is acknowledged that this study effectively studies the impact of the coupled lower air/hydrogen stream bulk velocity and lower injection temperature on the fuel mixing quality and emissions.

Differences in measured OH and CO mass fractions along $z = 0$ lines (Figure 7.14 and Figure 7.15, respectively) suggest potential differences in the formation mechanism of pollutant species, pointing towards the formation of higher temperature, higher pollutant production rate characterised zones near the injectors for case B that is consistent with other academic works that studied the typical flame structure in similar combustors. Additionally, the analysis of $Y_{C_{12}H_{23}}$ with x in Figure 7.10 seems to suggest that the new distribution of high temperature regions does not allow for the proper evaporation of all the injected fuel and there could be an increase in emitted UHC from case A to case B and. Both of these observations reveal possible mechanisms that might explain and fundament some of the differences in emissions captured at $x = 0.11\,m$. However, the analysed data does not allow for a definitive conclusion to be drawn about these phenomena. It could be said that it is just the emitted $C_{12}H_{23}$ that grows from case A to case B and not necessarily the UHC as a whole, or it could be said that the production rate of the species between case A and case B is roughly proportional to the volume of the reaction volumes and there is not any disproportionate increase in the production of CO, OH in case B due to any high temperature regions. Intentionally so, no conclusions are made about these observations anywhere in this work, however these observations stand as potential points of interest that could be studied in future works.

The mass-weighted averaging of species mass fraction over a dx volume was used as a way of obtaining the value of the species' mass fraction in a well-stirred volume. However, it is essential to remember that this notion does not hold when there are significant temperature variations inside the volume. This means that, depending on the measurement location, the mass-weighted averaging might be further skewed by the existence of reaction zones and high temperature zones. At $x = 0.11$ m the flow is sufficiently well mixed that this measurement is not affected meaningfully by this phenomenon. However, the mass-weighted averaging of the mass fraction of these species is biased by areas of high temperatures, which, in addition to the existence of recirculation and flow ”entrapment” in said recirculation zones, further makes mass-weighted averaging of a volume unreliable at lower values of x. An alternative that could address both issues is not straightforward and would likely require local probing near the flame front, which is why this analysis is accepted for the purposes of analysing trends in x and evaluating whether the measuring volume for the end-of-flame emissions is appropriately positioned.

The consistent issue with most results is the lack of computational resources and the consequential short total simulation time for each case. The analysis of emissions shows that the data extracted is often not conclusive, as the obtained average is associated with a high standard deviation, often due to the species still not having converged in time at that measuring volume position. Furthermore, it is likely that, despite the preventive measures taken to evaluate emissions, the measurements are still skewed by the formation of the recirculation zones that trap species near the walls of the combustor, leading to non-physical trends in species mass fractions with x. Despite the care in excluding these zones from measurements, because the solution has not been simulated for a sufficient time, there's no way to determine whether the measurements are representative of the far-field emissions. For this reason, the values presented are not analysed in detail, and instead, only conclusions are established around trends between cases. A more accurate study of this combustion would allow for much longer simulation times and would measure emissions at the outlet.

The analysis of the flame structure and of the flame stretch is obviously affected by the choice of a pseudo-progress variable and by the simplified analysis of the reaction zone, reduced to a surface characterised by $pPV = 0.5$, when the flame cannot be characterised as fully diffusive or fully premixed. Analysis of the results shows that an overwhelming part of the primary reaction zone is close to fully diffusive and the pPV is almost limited to a unity and closely overlap high HRR zones (as previously commented from the analysis of Figure B.5 and Figure B.7), meaning the primary reaction zone close to the injector is well tracked, despite the assumptions made. On the other hand however, it is recognized that this simplistic approach makes it hard to precisely isolate the flame front from the product rich recirculation zone, especially in case B as seen in Figure B.8 (Appendix B), explaining why the standard deviation associated with time averaging of the I_0 is so high and why the extracted conclusion is not as evident. Additionally, the HRR and pPV fields suggest that a simple description of pPV may not adequately capture secondary reaction zones directly downstream of the primary reaction zone, where the reactants are partially premixed or nearly fully premixed. This means that $pPV = 0.5$ likely does not capture a representative reactant reaction rate on surfaces that encapsulate these additional reaction zones, and thus the computed value of I_0 is most definitely not accurate. In this work, it is argued that the most relevant flow field and flame front interactions are observed between the well-anchored, consistently positioned primary reaction zones and the axial air/hydrogen stream, and so, the sufficiently precise tracking of the flame front that encapsulates the primary reaction zone allows for the analysis of the trend in stretch rate change between case A and case B in a way that is consistent between both cases.

8.2. Discussion on applied methodology

When modelling combustion, the TFM model is chosen to thicken the flame front and improve the resolution of reaction kinetics. The issue with this model is that it detects only $C_{12}H_{23}$ as the sensor species, which makes it impractical for resolving H_2 flames. This choice influences both simulated cases, as reaction zones that are relativelly rich in H_2 (i.e., the reaction zone detected at the core of the injected air/hydrogen stream) are not correctly refined, and thus the coarse mesh likely leads to gross estimates of the actual heat release and species release. Furthermore, other hydrocarbons that result from the dissociation of $C_{12}H_{23}$ are also not captured, which is also an issue with this combustor since there is significant dissociation of the main fuel species, resulting in significant sections of the flame front further downstream not being properly resolved. This was known before the simulation, and, as a preventive measure, the temperature SGS condition for AMR was used to refine areas of high temperature fluctuations. However, simulation results showed that some reaction zones were not captured by this additional condition, making it such that these reaction zones were affected by significant numerical diffusion. A proper analysis of this combustion likely requires another model or a different sensor definition that better accounts for the several reacting species in the combustor. Furthermore, the sensor was tuned based on existing values for the time scales associated with the Jaravel sensor and test simulations, however the tuning process of the sensor is not a well defined or studied procedure and while the tuning procedure revealed that certain sections of the flame front are well captured, a proper study on the effects of these coefficients on this exact flame might reveal a more appropriate selection of coefficients.

When defining the AMR algorithm, it was chosen to limit the maximum cell count to 10 million, allowing the software to adjust thresholds for each AMR condition dynamically. If allowed to run without a limit on cell count, the AMR algorithm will allow the cell count to grow to anywhere between 15 and 20 million cells, depending on the simulation. The mesh study revealed that, if the Pope [61] criterion can be used to evaluate the mesh in terms of turbulence resolution reliably, then the current mesh resolution is partially sufficient, with notable issues in correctly modelling the sub-grid scales up until the top of the swirler. However, the criterion does not evaluate if the mesh is sufficiently refined to properly refine flame fronts, and it stands that the cell count deficit between the uncapped and capped simulations likely results in some portion of the flame front not being properly refined, even though it would be refined without the cell count limit. The AMR algorithm typically prioritises the criterion with the highest value relative to its threshold. However, it is difficult to precisely evaluate how the mesh is affected over the long run. If sufficient computational resources had been available, this study should have included a mesh convergence study to rule out this possibility.

The choice of models and their applicability were properly outlined when relevant for this study. The choice of the SAGE combustion model proved to be critical, as the wide range of flame regimes and complex fuel mixtures would likely be too complex to model with simplified combustion models. Furthermore, the choice of SAGE as a combustion model most likely allowed the correct modelling of the observed secondary reaction zones and of the significant dissociation reactions downstream of and within the main reaction zones, respectively. Models that do not use detailed chemistry cannot model these reactions as accurately (i.e., FGM, EDM). Furthermore, compared to the RANS based simulations of this combustor by Palanti et al. [46], experimental data by Dave et al. [44], the results on the fluid flow field, spatial distribution of H_2 and mass fraction probing along constant $z = 0$ reveal complex flow structures and sharp gradients in cell values that could not be captured with a RANS approach. The resulting data analysis is likely clearer and more accurate due to the correct description of large-scale transport and the more accurate modelling of SGS fluxes. On the other hand, the impact of a skeletal chemical kinetics model is more ambiguous, and despite the successful validation of this model against more complex models and experimental data on laminar flames, it is not certain whether this model can maintain accuracy in the complex flow interactions with the flame front. The model has been used previously for a similar simulation in the APPU combustor [46], however, no validation data exists for this study either. It is plausible that the lack of soot, NO_x modelling most significantly impacted the formation rates of these species and partially affected the formation of other relevant secondary species, making this choice one of the most negatively impactful modelling choices in this work. However, as stated, since no further studies exist and due to computational limitations, the model is assumed to be sufficiently accurate for obtaining LES results at a cheaper computational cost. The modelling of soot and NO_x and the lack of modelling of radiation, the latter of which is coupled with the correct modelling of soot for the prediction of local temperatures in high reaction zones [159], [160], is also likely a source of some inaccuracy. The correct modelling of these quantities and of radiation might have led to some changes in the visualised trends between case A and case B. However, it is argued that the predicted impact would likely not have altered the conclusions, as radiation-soot absorption is often not a dominant mechanism in controlling the local cell temperature and, consequently, the reaction rate of dissociation reactions.

8.3. Discussion on proposed research questions

On the main research question, *”What is the impact of cooled hydrogen injection on the fuel mixing quality, flame structure and combustor emissions?”*, this work highlights that an increase in mixing quality between H_2 and $C_{12}H_{23}$ is a consequence of the lower temperature injection of hydrogen and air. The emissions analysis does not reveal sufficiently conclusive trends to compare the changes of soot, OH and NO_x against other existing literature, however, an evident drop in CO emissions with a decrease in injection temperature is observed. Finally, the analysis of the stretch factor and of the turbulent structure interactions reveals that a reduction in injection temperature likely leads to a relative increase in the measured primary reaction zone stretch factor and an increase in flame structure axial length. It is recognised, however, that this last observation cannot be attributed to just the decrease in inlet temperature and is also associated with the changes in the structure of the air/hydrogen stream and how it impacts the formation of large scale turbulent structure that significantly act on the curvature of the flame from case B to case A.

On the secondary research questions, it follows that for the first question, *”What is the impact of hydrogen temperature on species and particle distribution over the combustor”*, the analysis reveals that the mean particle distribution does not significantly change between case A and case B as seen from Figure 7.1b and Figure 7.2b. The distribution of species in the combustor does change significantly as seen from the analysis of species contours in a $z = 0$ slice and the cross section analysis of distribution of species. Firstly, it is noted that the peak in the measured mass fraction of OH and CO is observed closer to the injector, likely due to a change in the distribution of the reaction zones. Secondly, the distribution of injected H_2 in the core air/hydrogen stream shows that a lower injection temperature leads to a more gradual decrease in H_2 mass fraction with x and a reduction of the H_2 that reacts near the axial line of the combustor. Furthermore, it is observed that in the higher temperature case, a significantly higher amount of unburned $C_{12}H_{23}$ is allowed to travel downstream of the flame, likely indicating some loss in combustion efficiency as a consequence. The analysis of the H_2 distribution on the $z = 0$ slice from Figure B.4 also shows that the injected H_2 is allowed to penetrate further into the domain.

Finally, on the last secondary research question, *”What is the impact of hydrogen temperature on flame stretch and flame front turbulent interactions”*, it seen that lower injection temperatures and lower air/hydrogen stream bulk velocity leads to the formation of a more coherent jet structure with lower effective swirl intensity that lead to the formation of larger turbulent structures that interact differently with the flame front near the interface between the injected air/hydrogen stream and the main reaction zones. The visualised effect suggests that, in case A, the structures form much closer to the flame front and significantly impact the local flame curvature. It is then qualitatively assessed, through both qualitative assessment of the flow field and the computation of flame stretch factor, that the flame front associated with the primary reaction zone is more strongly affected by large-scale turbulent structures and there is a likelly increase in flame stretch characterizing the main reaction zones in case A.

9

Conclusions and recommendations

In this work, a Large Eddy Simulation approach was used to resolve the combustion for two different cases of different injection temperatures in order to understand the impacts on fuel mixing, emissions and flame characteristics. The two simulations were conducted on a model replica of the APPU using the same boundary conditions, with the static temperature of the hydrogen and air inlets changed from 250 K in case A to 400 K in case B. The LES combustion simulations were run for $t = 0.125$ s and the results were extracted and analysed to answer

9.1. Main conclusions on obtained results

The analysis showed a qualitative improvement in fuel mixing quality across several different analyses, strongly suggesting that the reduction of hydrogen and air inlet temperature leads to better mixing of $C_{12}H_{23}$ and injected H_2 ahead of the reaction zones. The analysis of pollutant emissions does not allow for conclusions to be drawn on the emissions of NO_x, soot and OH, however, it was observed that there is a significant reduction in CO emissions with lower temperature hydrogen injection, which is consistent with past literature on the effects of fuel mixing quality of hydrogen and typical jet fuels. Further analysis of the species distributions reveal that the formation of secondary reaction products is less distributed in the axial direction and peaks closer to the $C_{12}H_{23}$ injectors. Additionally, relatively rich H_2 regions are suppressed as injected H_2 is seen more evenly distributed over the interface between the primary reaction zone and the air/hydrogen stream.

Analysis of the flow field and the stretch factor associated with the pPV captured flame front suggest that the injection of a lower temperature air/hydrogen mixture likelly leads to an increase in stretch rate acting on the primary reaction zone anchored close to the $C_{12}H_{23}$ injectors. However, this phenomenon could not be fully uncoupled from the change in injection velocity, associated with the change in inlet temperature, and the conclusion is only valid from the combined quantitive and qualitative analysis of flame stretch factor and flow field interactions, respectively. The lower injection temperature, coupled with the formation of an air/hydrogen stream with lower effective swirl intensity, has also been observed to impact the formation of large scale structures from the air/hydrogen stream that strongly interact with the primary reaction zone in order to increase the flame stretch associated with the primary reaction zones. The proposed research questions are answered, and the initial hypothesis on the increase in time for proper fuel mixing is strongly supported by the analysis of the results.

It is recognised that the analysis performed in this work is predominantly limited by the lack of computational resources, the use of a skeletal chemical kinetics mechanism, and the uncoupling between injection velocity and injection temperature. Some research questions are left partially answered due to a combination of these factors. This research provides light into the main impact of injection temperature of hydrogen and air in a partially premixed combustor, and creates a basis for the use of lower temperature hydrogen to improve fuel mixing quality in combustors with otherwise poor fuel mixing quality. However, it is recognised that exact results and more definite conclusions on the impact of this effect on emissions and flame characteristics require further studies.

9.2. Future recommendations

As recognised, further research on this topic needs to address the three main issues associated with this work, mainly the simulation of the LES combustion for longer periods of time until, at least, statistical convergence of the outlet species mass fraction flow rate measurements is attained. Furthermore, for the correct analysis of the emissions, a mechanism that includes formation pathways for NO_X and includes soot precursors for the use of detailed soot formation mechanisms is required, as the current models are too dependent on pre-determined coefficients to yield accurate measurements of these quantities. Although less relevant, if soot is modelled correctly, then radiation could also be modelled to obtain an accurate evaluation of the secondary effects of soot reduction. Finally, a mesh validation study should be conducted, not only to ensure that Pope's M criterion is satisfied for the domain, but also to assess whether the maximum number of AMR cells (if AMR is used) conditions the formation and development of any significant reaction zones.

In line with the observations of higher $C_{12}H_{23}$ mass fraction ahead of the flame for the higher temperature case, further studies should also consider cataloguing and accounting for UHC species to evaluate changes in total UHC emissions. Additionally, to understand the exact and isolated impact of H_2 on the emissions and flame structure, the geometry could be altered to maintain the injection speed when changing the injection temperature, or the hydrogen injection strategy could be altered such that there is no need to change the air temperature but still allow for hydrogen to reach the fuel mixing zones at lower temperatures. Finally, future research could also investigate the use of the Q-criterion [161] for vortex visualisation in order to understand exactly how the formation of large scale structures is affected between high and low temperature cases and whether it may be a consequence of injection temperature alone.

A

Z77 chemical kinetics mechanism data files

A.1. Z77 mechanism (Chemkin format)

```
ELEMENTS
H O C N
END

SPECIES
C12H23
C12H22
C12H22O2
C12H22O
C12H22O2H
C12H21OOH
C12H21
C12ket
OOC12H21OOH
C5H11CO
C2H5
C2H4
C2H3
C2H2
C2H
CH2
CH
CH4
CH3
CH3O
CH2O
HCO
CO
CO2
O2
N2
H2O
H
O
OH
H2
HO2
H2O2
END


REACTIONS CAL/MOLE MOLES
C12H23 => C2H3 + 5 C2H4                     300000000000.0 1.5 70000.0
C12H23 + O2 => C12H22 + HO2                 2000000000000000.2 0.0 50150.0
```

```
C12H23 + OH => C12H22 + H2O                 30000000.000000004 1.85 58.5
C12H23 + H => C12H22 + H2                   200000000.00000003 2.0 2500.0
C12H23 + HO2 => C12H22 + H2O2               212000000000000.03 0.0 17690.0
C12H22 + O2 => C12H22O2                     200000000000.00003 0.0 4500.0
C12H22O2 => C12H21OOH                       55100000000000.0 0.0 19000.0
C12H21OOH + O2 => OOC12H21OOH               200000000000.00003 0.0 0.0
OOC12H21OOH => C12ket + OH                  89100000000.0 0.0 17000.0
C12ket => 2 C2H3 + C5H11CO + CH + CH2O + OH 1.98e+16 0.0 41000.0
C5H11CO + O2 => C2H4 + C2H5 + CH + CO + HO2 31600000000000.004 0.0 10000.0
C12H22 + O2 => C12H21 + HO2                 316000000000.00006 0.0 6000.0
C12H21 + O2 => 2 C2H3 + 3 C2H4 + CH2O + HCO 31600000000000.004 0.0 10000.0
C12H22 => 2 C2H3 + 4 C2H4                   40000000000000.0 0.0 28810.0
C2H4 + H + M => C2H5 + M                    41700000000.00001 0.0 11030.0
C2H5 + H => 2 CH3                           31600000000000.004 0.0 0.0
C2H4 => C2H3 + H                            1000000000000.0 0.0 50000.0
C2H4 + H => C2H5                            7000000000000.001 1.0 10800.0
C2H4 + O => CH3 + HCO                       3310000000000.0005 0.0 1130.0
CH3 + HCO => C2H4 + O                       158000000000.00003 0.0 25000.0
C2H4 + OH => C2H3 + H2O                     4790000000000.001 0.0 1230.0
C2H3 + H2O => C2H4 + OH                     1200000000000.0002 0.0 14000.0
C2H4 + CH3 => C2H3 + CH4                    10000000000000.002 0.0 13000.0
C2H3 + CH4 => C2H4 + CH3                    30200000000000.004 0.0 12580.0
C2H2 + H + M => C2H3 + M                    123000000000.00003 1.0 10360.0
C2H3 + H => C2H2 + H2                       20000000000000.004 0.0 2500.0
C2H3 => C2H + H2                            5000000000000.0 0.0 44000.0
C2H + H + M => C2H2 + M                     1100000000.0000002 1.0 770.0
C2H2 + H => C2H + H2                        200000000000000.03 0.0 19000.0
C2H2 + OH => C2H + H2O                      8000000000000.001 0.0 5000.0
C2H + H2O => C2H2 + OH                      5370000000000.001 0.0 16360.0
C2H2 + O => C2H + OH                        3240000000000000.5 0.6 12000.0
C2H + OH => C2H2 + O                        295000000000000.06 0.6 910.0
C2H + O2 => CO + HCO                        10000000000000.002 0.0 6500.0
CO + HCO => C2H + O2                        8510000000000.002 0.0 138400.0
H + O2 => O + OH                            170000000000000.03 0.0 16800.0
O + OH => H + O2                            14000000000000.002 0.0 690.0
H2 + O => H + OH                            18000000000.000004 1.0 8826.0
H + OH => H2 + O                            8000000000.000001 1.0 6760.0
H2 + OH => H + H2O                          1170000000.0000002 1.3 3626.0
H + H2O => H2 + OH                          7000000000.000001 1.3 18588.0
2 OH => H2O + O                             600000000.0000001 1.3 0.0
H2O + O => 2 OH                             5900000000.000001 1.3 17029.000000000004
H + O2 + M => HO2 + M                       8.000000000000001e+17 -0.8 0.0
CH4/6.500E+00/ CO/7.500E-01/ CO2/1.500E+00/ H2/1.000E+00/ H2O/6.500E+00/ N2/4.000E-01/ O2
    /4.000E-01/
H + HO2 => 2 OH                             150000000000000.03 0.0 1004.0
H + HO2 => H2 + O2                          25000000000000.004 0.0 699.9999999999999
HO2 + OH => H2O + O2                        20000000000000.004 0.0 1000.0
CO + OH => CO2 + H                          15100000.000000004 1.3 -758.0
CO2 + H => CO + OH                          1570000000.0000002 1.3 20900.0
CH4 (+M) => CH3 + H (+M)                    630000000000000.0 0.0 104000.0
LOW /1.0000000000000002e+17 0.0 86000.0/
C12H23/3.000E+00/ CH4/6.500E+00/ CO/7.500E-01/ CO2/1.500E+00/ H2/1.000E+00/ H2O/6.500E+00/ N2
    /4.000E-01/ O2/4.000E-01/
CH3 + H (+M) => CH4 (+M)                    5200000000000.001 0.0 -1310.0
LOW /825000000000000.1 0.0 -19310.0/
C12H23/3.000E+00/ CH4/6.500E+00/ CO/7.500E-01/ CO2/1.500E+00/ H2/1.000E+00/ H2O/6.500E+00/ N2
    /4.000E-01/ O2/4.000E-01/
CH4 + H => CH3 + H2                         22000.000000000004 3.0 8750.0
CH3 + H2 => CH4 + H                         957.0000000000002 3.0 8750.0
CH4 + OH => CH3 + H2O                       1600000.0000000002 2.1 2460.0
CH3 + H2O => CH4 + OH                       302000.00000000006 2.1 17422.0
CH3 + O => CH2O + H                         68000000000000.016 0.0 0.0
CH2O + H => H2 + HCO                        50000000000000.01 0.0 3991.0
CH2O + OH => H2O + HCO                      120000000000000.02 0.0 1100.0
H + HCO => CO + H2                          40000000000000.01 0.0 0.0
HCO + M => CO + H + M                       160000000000000.03 0.0 14700.0
CH3 + O2 => CH3O + O                        50000000000000.01 0.0 25652.0
CH3O + H => CH2O + H2                       20000000000000.004 0.0 0.0
CH3O + M => CH2O + H + M                    24000000000000.004 0.0 28812.0
2 HO2 => H2O2 + O2                          80000000000000.02 0.0 0.0
H2O2 + M => 2 OH + M                        1.3000000000000002e+17 0.0 45500.0
```

```
2 OH + M => H2O2 + M                        986000000000000.2 0.0 -5070.0
H2O2 + OH => H2O + HO2                      10000000000000.002 0.0 1800.0
H2O + HO2 => H2O2 + OH                      28600000000000.004 0.0 32790.0
H + OH + M => H2O + M                       2.2000000000000004e+22 -2.0 0.0
2 H + M => H2 + M                           1.8000000000000003e+18 -1.0 0.0
CH3 + OH => CH2 + H2O                       7600000.000000002 2.0 5000.0
CH2 + O => CO + H2                          30000000000000.004 0.0 0.0
CH2 + OH => CH + H2O                        40000000.00000001 2.0 3000.0
CH + O => CO + H                            57000000000000.01 0.0 0.0
CH + OH => H + HCO                          30000000000000.004 0.0 0.0
CH + O2 => HCO + O                          33000000000000.004 0.0 0.0
CH + CO2 => CO + HCO                        84000000000000.02 0.0 200.0
END
```

A.2. Thermodynamical data (Chemkin format)

```
THERMO
200.000   1000.000  5000.000
C12H23                  C  12H  23          G273.150   5000.000  1000.000      1
 2.48802010E+01 7.82500480E-02-3.15509730E-05 5.78789000E-09-3.98279680E-13    2
-3.85088370E+04-9.55682400E+01 2.08692170E+00 1.33149650E-01-8.11574520E-05    3
 2.94092860E-08-6.51952130E-12-3.13109660E+04 2.54423050E+01                   4
C12H22                  C  12H  22          G298.150   5000.000  1000.000      1
 3.17282625E+01 6.57676191E-02-2.47588062E-05 4.36737771E-09-2.92802346E-13    2
-5.21805961E+04-1.23815892E+02 2.72033532E+00 1.26724515E-01-5.65612605E-05    3
-6.33058878E-09 9.83998571E-12-4.24023647E+04 3.24602457E+01                   4
C12H22O2                C  12H  22O   2     G298.150   5000.000  1000.000      1
 3.17282625E+01 6.57676191E-02-2.47588062E-05 4.36737771E-09-2.92802346E-13    2
-5.21805961E+04-1.23815892E+02 2.72033532E+00 1.26724515E-01-5.65612605E-05    3
-6.33058878E-09 9.83998571E-12-4.24023647E+04 3.24602457E+01                   4
C12H22O                 C  12H  22O   1     G298.150   5000.000  1000.000      1
 3.17282625E+01 6.57676191E-02-2.47588062E-05 4.36737771E-09-2.92802346E-13    2
-5.21805961E+04-1.23815892E+02 2.72033532E+00 1.26724515E-01-5.65612605E-05    3
-6.33058878E-09 9.83998571E-12-4.24023647E+04 3.24602457E+01                   4
C12H22O2H               C  12H  23O   2     G298.150   5000.000  1000.000      1
 3.17282625E+01 6.57676191E-02-2.47588062E-05 4.36737771E-09-2.92802346E-13    2
-5.21805961E+04-1.23815892E+02 2.72033532E+00 1.26724515E-01-5.65612605E-05    3
-6.33058878E-09 9.83998571E-12-4.24023647E+04 3.24602457E+01                   4
C12H21OOH               C  12H  22O   2     G298.150   5000.000  1000.000      1
 3.17282625E+01 6.57676191E-02-2.47588062E-05 4.36737771E-09-2.92802346E-13    2
-5.21805961E+04-1.23815892E+02 2.72033532E+00 1.26724515E-01-5.65612605E-05    3
-6.33058878E-09 9.83998571E-12-4.24023647E+04 3.24602457E+01                   4
C12H21                  C  12H  21          G298.150   5000.000  1000.000      1
 3.17282625E+01 6.57676191E-02-2.47588062E-05 4.36737771E-09-2.92802346E-13    2
-5.21805961E+04-1.23815892E+02 2.72033532E+00 1.26724515E-01-5.65612605E-05    3
-6.33058878E-09 9.83998571E-12-4.24023647E+04 3.24602457E+01                   4
C12ket                  C  12H  21O   3     G298.150   5000.000  1000.000      1
 3.17282625E+01 6.57676191E-02-2.47588062E-05 4.36737771E-09-2.92802346E-13    2
-5.21805961E+04-1.23815892E+02 2.72033532E+00 1.26724515E-01-5.65612605E-05    3
-6.33058878E-09 9.83998571E-12-4.24023647E+04 3.24602457E+01                   4
OOC12H21OOH             C  12H  22O   4     G298.150   5000.000  1000.000      1
 3.17282625E+01 6.57676191E-02-2.47588062E-05 4.36737771E-09-2.92802346E-13    2
-5.21805961E+04-1.23815892E+02 2.72033532E+00 1.26724515E-01-5.65612605E-05    3
-6.33058878E-09 9.83998571E-12-4.24023647E+04 3.24602457E+01                   4
C5H11CO                 C   6H  11O   1     G300.000   5000.000  1000.000      1
 1.94783812E+01 2.50466029E-02-8.54861346E-06 1.32557944E-09-7.68503296E-14    2
-2.07923937E+04-7.21995578E+01 2.14479069E+00 6.17863563E-02-3.74134690E-05    3
 1.13283795E-08-1.36917698E-12-1.43451172E+04 2.23128045E+01                   4
C2H5                    C   2H   5          G300.000   5000.000  1000.000      1
 1.95465642E+00 1.73972722E-02-7.98206668E-06 1.75217689E-09-1.49641576E-13    2
 1.28575200E+04 1.34624343E+01 4.30646568E+00-4.18658892E-03 4.97142807E-05    3
-5.99126606E-08 2.30509004E-11 1.28416265E+04 4.70720924E+00                   4
C2H4                    C   2H   4          G300.000   5000.000  1000.000      1
 2.03611116E+00 1.46454151E-02-6.71077915E-06 1.47222923E-09-1.25706061E-13    2
 4.93988614E+03 1.03053693E+01 3.95920148E+00-7.57052247E-03 5.70990292E-05    3
-6.91588753E-08 2.69884373E-11 5.08977593E+03 4.09733096E+00                   4
C2H3                    C   2H   3          G300.000   5000.000  1000.000      1
 3.01672400E+00 1.03302292E-02-4.68082349E-06 1.01763288E-09-8.62607041E-14    2
 3.46128739E+04 7.78732378E+00 3.21246645E+00 1.51479162E-03 2.59209412E-05    3
-3.57657847E-08 1.47150873E-11 3.48598468E+04 8.51054025E+00                   4
```

```
C2H2                    C   2H   2          G300.000   5000.000  1000.000      1
 4.14756964E+00 5.96166664E-03-2.37294852E-06 4.67412171E-10-3.61235213E-14    2
 2.59359992E+04-1.23028121E+00 8.08681094E-01 2.33615629E-02-3.55171815E-05    3
 2.80152437E-08-8.50072974E-12 2.64289807E+04 1.39397051E+01                   4
C2H                     C   2H   1          G300.000   5000.000  1000.000      1
 3.16780652E+00 4.75221902E-03-1.83787077E-06 3.04190252E-10-1.77232770E-14    2
 6.71210650E+04 6.63589475E+00 2.88965733E+00 1.34099611E-02-2.84769501E-05    3
 2.94791045E-08-1.09331511E-11 6.68393932E+04 6.22296438E+00                   4
CH2                     C   1H   2          G200.000   3500.000  1000.000      1
 2.87410113E+00 3.65639292E-03-1.40894597E-06 2.60179549E-10-1.87727567E-14    2
 4.62636040E+04 6.17119324E+00 3.76267867E+00 9.68872143E-04 2.79489841E-06    3
-3.85091153E-09 1.68741719E-12 4.60040401E+04 1.56253185E+00                   4
CH                      C   1H   1          G200.000   3500.000  1000.000      1
 2.87846473E+00 9.70913681E-04 1.44445655E-07-1.30687849E-10 1.76079383E-14    2
 7.10124364E+04 5.48497999E+00 3.48981665E+00 3.23835541E-04-1.68899065E-06    3
 3.16217327E-09-1.40609067E-12 7.07972934E+04 2.08401108E+00                   4
CH4                     C   1H   4          G300.000   5000.000  1000.000      1
 1.68347900E+00 1.02372400E-02-3.87512900E-06 6.78558500E-10-4.50342300E-14    2
-1.00807900E+04 9.62339500E+00 7.78741500E-01 1.74766800E-02-2.78340900E-05    3
 3.04970800E-08-1.22393100E-11-9.82522900E+03 1.37221900E+01                   4
CH3                     C   1H   3          G300.000   5000.000  1000.000      1
 2.84405200E+00 6.13797400E-03-2.23034500E-06 3.78516100E-10-2.45215900E-14    2
 1.64378100E+04 5.45269700E+00 2.43044300E+00 1.11241000E-02-1.68022000E-05    3
 1.62182900E-08-5.86495300E-12 1.64237800E+04 6.78979400E+00                   4
CH3O                    C   1H   3O   1     G300.000   3000.000  1000.000      1
 3.77080000E+00 7.87149700E-03-2.65638400E-06 3.94443100E-10-2.11261600E-14    2
 1.27832500E+02 2.92957500E+00 2.10620400E+00 7.21659500E-03 5.33847200E-06    3
-7.37763600E-09 2.07561100E-12 9.78601100E+02 1.31521800E+01                   4
CH2O                    C   1H   2O   1     G300.000   5000.000  1000.000      1
 2.99560600E+00 6.68132100E-03-2.62895500E-06 4.73715300E-10-3.21251700E-14    2
-1.53203700E+04 6.91257200E+00 1.65273100E+00 1.26314400E-02-1.88816800E-05    3
 2.05003100E-08-8.41323700E-12-1.48654000E+04 1.37848200E+01                   4
HCO                     C   1H   1O   1     G300.000   5000.000  1000.000      1
 3.55727100E+00 3.34557300E-03-1.33500600E-06 2.47057300E-10-1.71385100E-14    2
 3.91632400E+03 5.55229900E+00 2.89833000E+00 6.19914700E-03-9.62308400E-06    3
 1.08982500E-08-4.57488500E-12 4.15992200E+03 8.98361400E+00                   4
CO                      C   1O   1          G300.000   5000.000  1000.000      1
 3.02507800E+00 1.44268900E-03-5.63082800E-07 1.01858100E-10-6.91095200E-15    2
-1.42683500E+04 6.10821800E+00 3.26245200E+00 1.51194100E-03-3.88175500E-06    3
 5.58194400E-09-2.47495100E-12-1.43105400E+04 4.84889700E+00                   4
CO2                     C   1O   2          G300.000   5000.000  1000.000      1
 4.45362300E+00 3.14016900E-03-1.27841100E-06 2.39399700E-10-1.66903300E-14    2
-4.89669600E+04-9.55395900E-01 2.27572500E+00 9.92207200E-03-1.04091100E-05    3
 6.86668700E-09-2.11728000E-12-4.83731400E+04 1.01884900E+01                   4
O2                      O   2               G300.000   5000.000  1000.000      1
 3.69757800E+00 6.13519700E-04-1.25884200E-07 1.77528100E-11-1.13643500E-15    2
-1.23393000E+03 3.18916600E+00 3.21293600E+00 1.12748600E-03-5.75615000E-07    3
 1.31387700E-09-8.76855400E-13-1.00524900E+03 6.03473800E+00                   4
N2                      N   2               G300.000   5000.000  1000.000      1
 2.92664000E+00 1.48797700E-03-5.68476100E-07 1.00970400E-10-6.75335100E-15    2
-9.22797700E+02 5.98052800E+00 3.29867700E+00 1.40824000E-03-3.96322200E-06    3
 5.64151500E-09-2.44485500E-12-1.02090000E+03 3.95037200E+00                   4
H2O                     H   2O   1          G300.000   5000.000  1000.000      1
 2.67214600E+00 3.05629300E-03-8.73026000E-07 1.20099600E-10-6.39161800E-15    2
-2.98992100E+04 6.86281700E+00 3.38684200E+00 3.47498200E-03-6.35469600E-06    3
 6.96858100E-09-2.50658800E-12-3.02081100E+04 2.59023300E+00                   4
H                       H   1               G300.000   5000.000  1000.000      1
 2.50000000E+00 0.00000000E+00 0.00000000E+00 0.00000000E+00 0.00000000E+00    2
 2.54716300E+04-4.60117600E-01 2.50000000E+00 0.00000000E+00 0.00000000E+00    3
 0.00000000E+00 0.00000000E+00 2.54716300E+04-4.60117600E-01                   4
O                       O   1               G300.000   5000.000  1000.000      1
 2.54206000E+00-2.75506200E-05-3.10280300E-09 4.55106700E-12-4.36805200E-16    2
 2.92308000E+04 4.92030800E+00 2.94642900E+00-1.63816600E-03 2.42103200E-06    3
-1.60284300E-09 3.89069600E-13 2.91476400E+04 2.96399500E+00                   4
OH                      H   1O   1          G300.000   5000.000  1000.000      1
 2.88273000E+00 1.01397400E-03-2.27687700E-07 2.17468400E-11-5.12630500E-16    2
 3.88688800E+03 5.59571200E+00 3.63726600E+00 1.85091000E-04-1.67616500E-06    3
 2.38720300E-09-8.43144200E-13 3.60678200E+03 1.35886000E+00                   4
H2                      H   2               G300.000   5000.000  1000.000      1
 2.99142300E+00 7.00064400E-04-5.63382900E-08-9.23157800E-12 1.58275200E-15    2
-8.35034000E+02-1.35511000E+00 3.29812400E+00 8.24944200E-04-8.14301500E-07    3
```

```
-9.47543400E-11 4.13487200E-13-1.01252100E+03-3.29409400E+00                   4
HO2                     H   1O   2          G300.000   5000.000  1000.000      1
 4.01721090E+00 2.23982013E-03-6.33658150E-07 1.14246370E-10-1.07908535E-14    2
 1.11856713E+02 3.78510215E+00 4.30179801E+00-4.74912051E-03 2.11582891E-05    3
-2.42763894E-08 9.29225124E-12 2.94808040E+02 3.71666245E+00                   4
H2O2                    H   2O   2          G300.000   5000.000  1000.000      1
 4.57316700E+00 4.33613600E-03-1.47468900E-06 2.34890400E-10-1.43165400E-14    2
-1.80069600E+04 5.01137000E-01 3.38875400E+00 6.56922600E-03-1.48501300E-07    3
-4.62580600E-09 2.47151500E-12-1.76631500E+04 6.78536300E+00                   4
END
```

A.3. Transport data (Chemkin format)

```
TRANSPORT
C12H23             2   266.800     4.980     0.000     0.000     1.000
C12H22             2   580.000     7.600     0.000     0.000     1.000
C12H22O2           2   580.000     7.600     0.000     0.000     1.000
C12H22O            2   580.000     7.600     0.000     0.000     1.000
C12H22O2H          2   580.000     7.600     0.000     0.000     1.000
C12H21OOH          2   580.000     7.600     0.000     0.000     1.000
C12H21             2   580.000     7.600     0.000     0.000     1.000
C12ket             2   580.000     7.600     0.000     0.000     1.000
OOC12H21OOH        2   580.000     7.600     0.000     0.000     1.000
C5H11CO            2   498.600     6.009     2.000     0.000     1.000
C2H5               2   247.500     4.350     0.000     0.000     1.500
C2H4               2   238.400     3.496     0.000     0.000     1.500
C2H3               2   265.300     3.721     0.000     0.000     1.000
C2H2               1   265.300     3.721     0.000     0.000     2.500
C2H                1   265.300     3.721     0.000     0.000     2.500
CH2                1   144.000     3.800     0.000     0.000     0.000
CH                 1    80.000     2.750     0.000     0.000     0.000
CH4                2   141.400     3.746     0.000     2.600    13.000
CH3                1   144.000     3.800     0.000     0.000     0.000
CH3O               2   417.000     3.690     1.700     0.000     2.000
CH2O               2   498.000     3.590     0.000     0.000     2.000
HCO                2   498.000     3.590     0.000     0.000     0.000
CO                 1    98.100     3.650     0.000     1.950     1.800
CO2                1   244.000     3.763     0.000     2.650     2.100
O2                 1   107.400     3.458     0.000     1.600     3.800
N2                 1    97.530     3.621     0.000     1.760     4.000
H2O                2   572.400     2.605     1.844     0.000     4.000
H                  0   145.000     2.050     0.000     0.000     0.000
O                  0    80.000     2.750     0.000     0.000     0.000
OH                 1    80.000     2.750     0.000     0.000     0.000
H2                 1    38.000     2.920     0.000     0.790   280.000
HO2                2   107.400     3.458     0.000     0.000     1.000
H2O2               2   107.400     3.458     0.000     0.000     3.800
END
```

B

Additional results

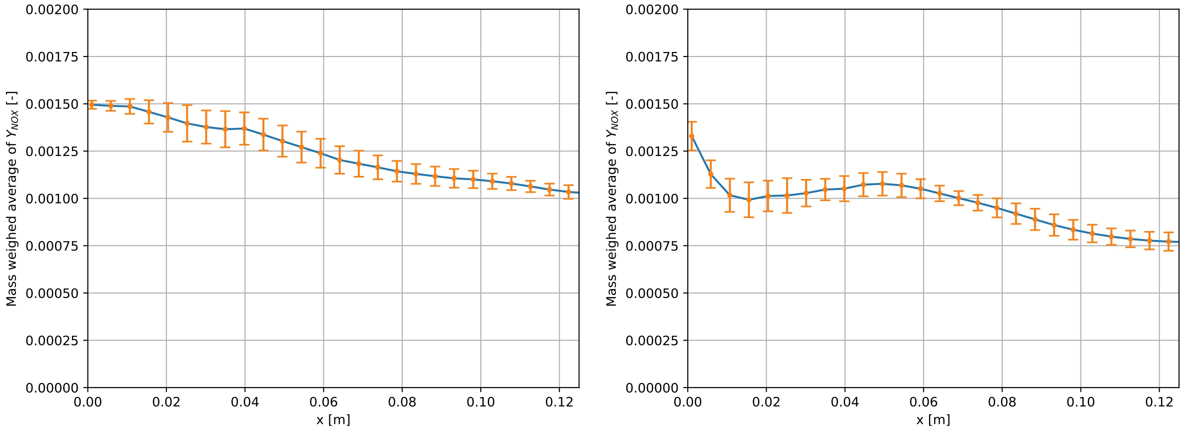

(a) Mass fraction of NO$_x$ plotted for 4 $z = 0$ lines over y, case A **(b)** Mass fraction of NO$_x$ plotted for 4 $z = 0$ lines over y, case B

Figure B.1: Mass weighed averaged of Y_{NO_x} over equidistant planes from $x = 0.001\,m$ to $x = 0.125\,m$ for both cases plotted in blue. The standard deviation (from time averaging) for each plane is plotted in orange.

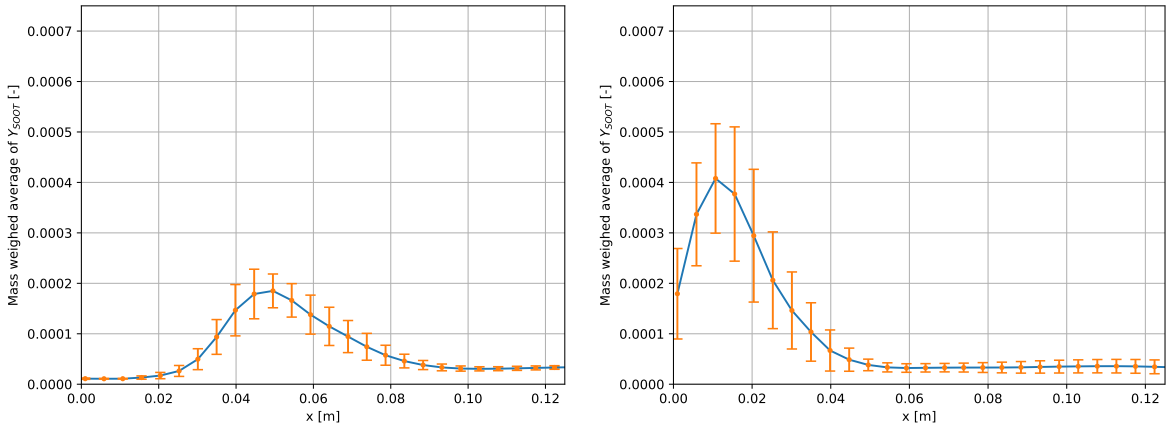

(a) Mass fraction of soot plotted for 4 $z = 0$ lines over y, case A **(b)** Mass fraction of soot plotted for 4 $z = 0$ lines over y, case B

Figure B.2: Mass weighed averaged of Y_{soot} over equidistant planes from $x = 0.001\,m$ to $x = 0.125\,m$ for both cases plotted in blue. The standard deviation (from time averaging) for each plane is plotted in orange.

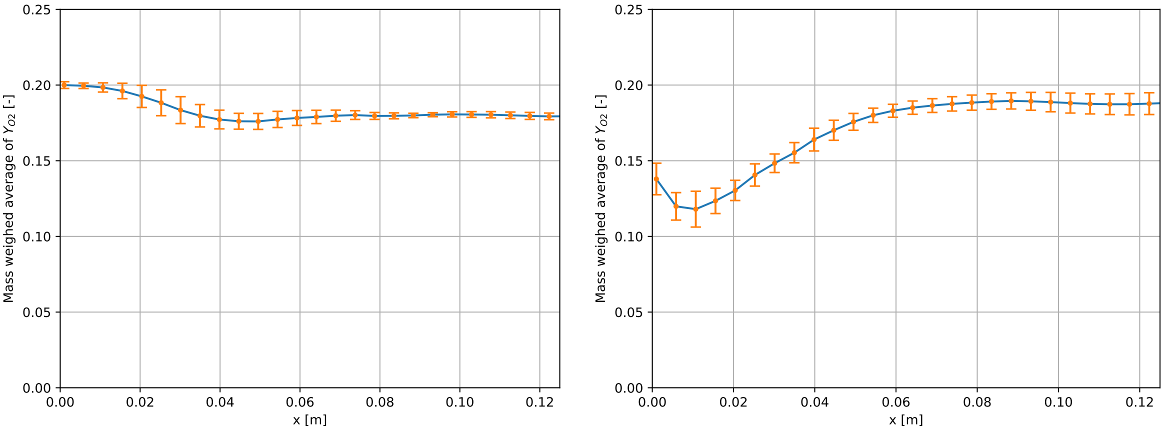

(a) Case A

(b) Case B

Figure B.3: Mass weighed averaged of Y_{O_2} over equidistant planes from $x = 0.001\,m$ to $x = 0.125\,m$ for both cases plotted in blue. The standard deviation (from time averaging) for each plane is plotted in orange.

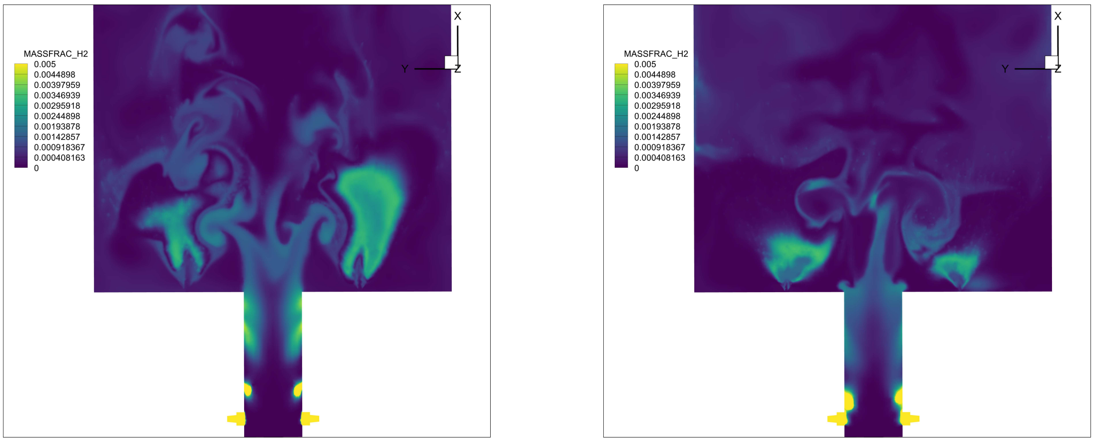

(a) case A, $t = 0.1\,s$

(b) case B,$t = 0.1\,s$

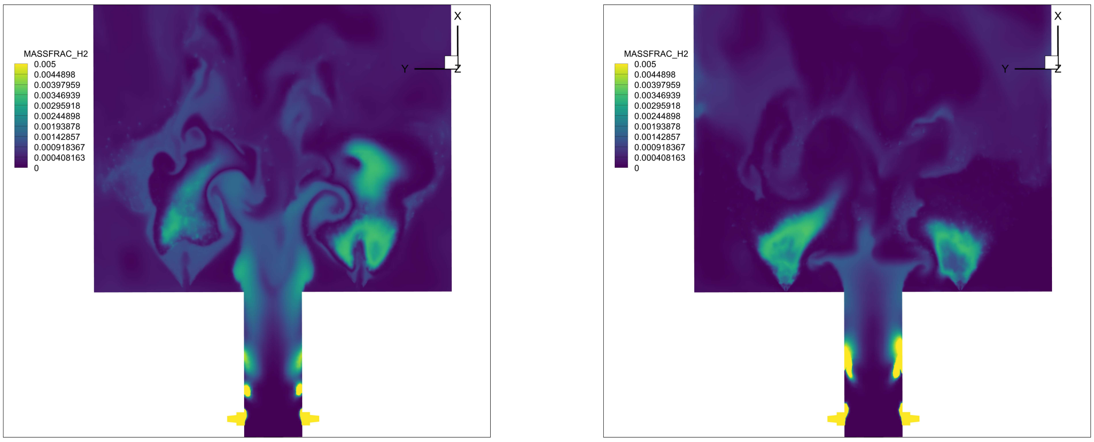

(c) case A, $t = 0.11\,s$

(d) case B, $t = 0.11\,s$

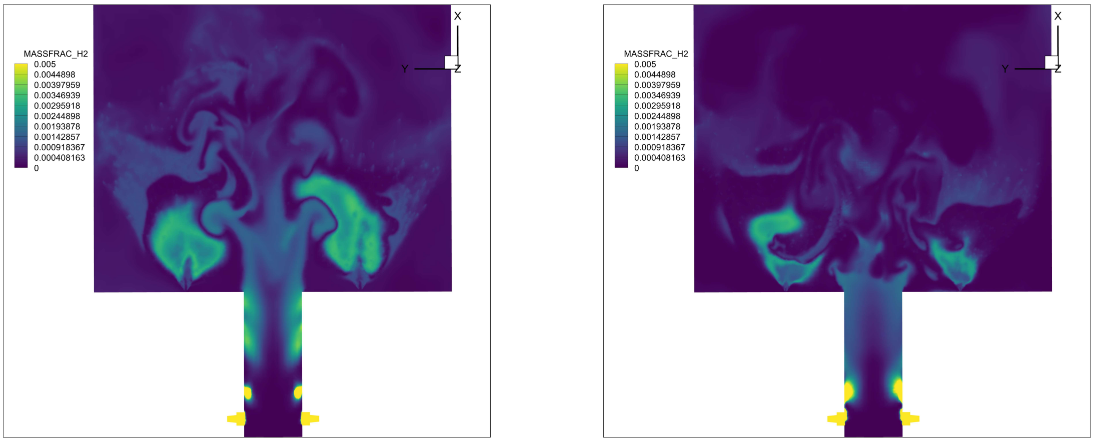

(e) case A, $t = 0.125\,s$

(f) case B, $t = 0.125\,s$

Figure B.4: Z=0 slice of the H$_2$ mass fraction Y_{H_2}, contour scale limited to 0.5% maximum mass fraction. Plotted for three different relevant solution points for case A and case B.

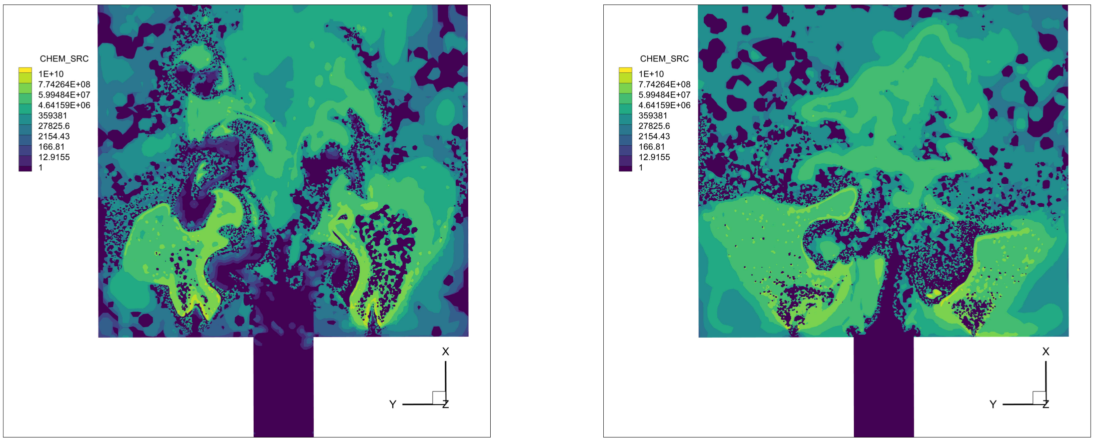

(a) case A, $t = 0.1\ s$

(b) case B,$t = 0.1\ s$

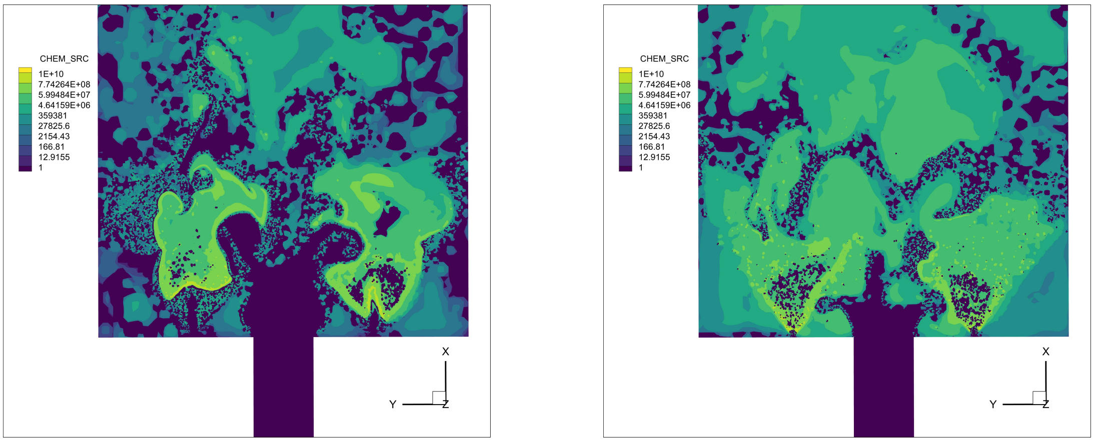

(c) case A, $t = 0.11\ s$

(d) case B, $t = 0.11\ s$

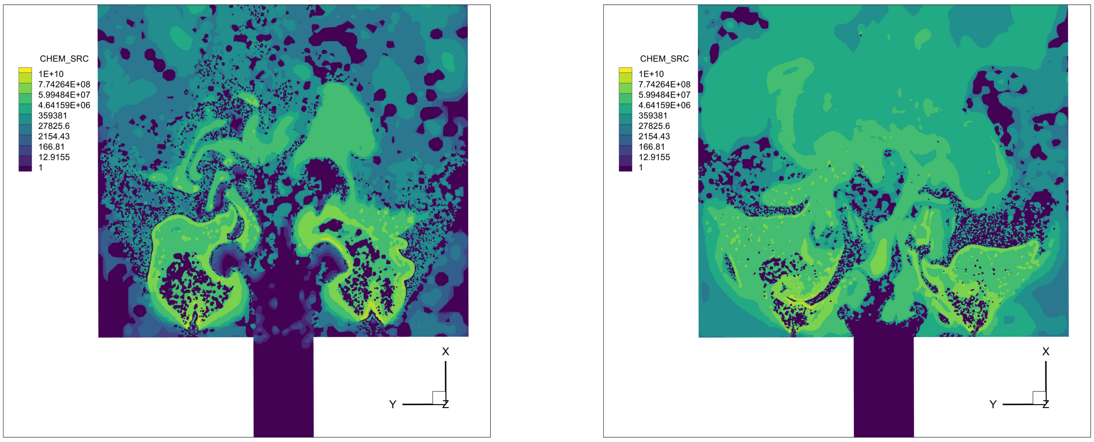

(e) case A, $t = 0.125\ s$

(f) case B, $t = 0.125\ s$

Figure B.5: Z=0 slice of the Heat Release Rate [$J/kg/m^3$] ($CHEM\_SRC$ variable). Contour scale limited to positive values and exponential scale is used to define the values of each of the 10 colour bands used. Plotted for three different relevant solution points for case A and case B

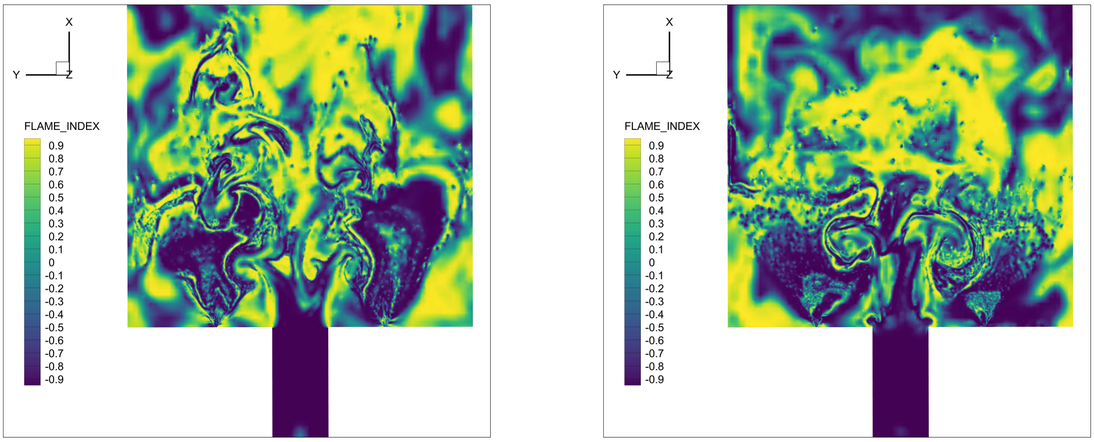

(a) case A, $t = 0.1\,s$ **(b)** case B,$t = 0.1\,s$

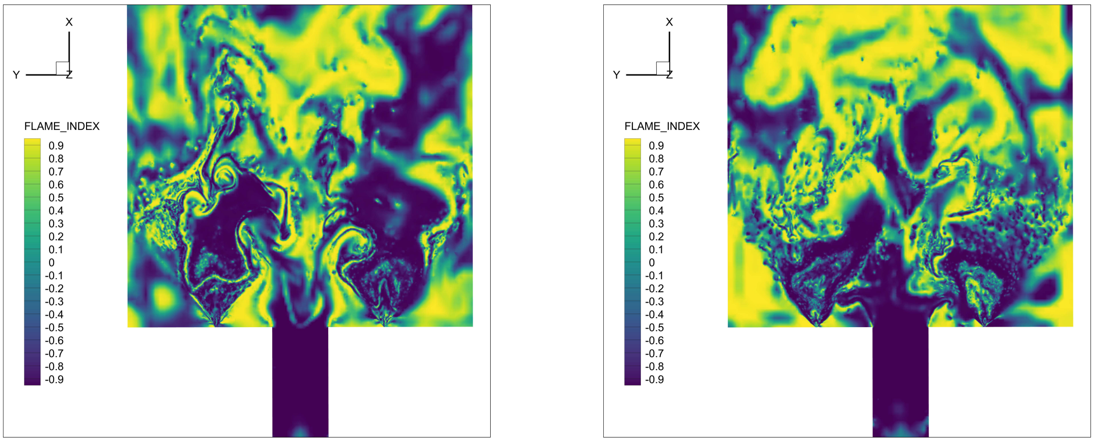

(c) case A, $t = 0.11\,s$ **(d)** case B, $t = 0.11\,s$

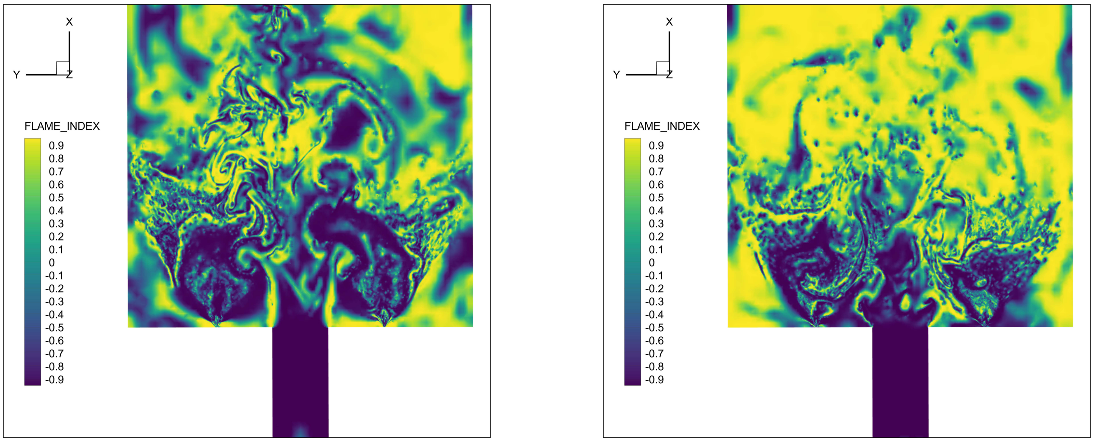

(e) case A, $t = 0.125\,s$ **(f)** case B, $t = 0.125\,s$

Figure B.6: Z=0 slice of the Takeno index [158], shown using the *Flame index* variable. *Flame index* identifies flame regime from 1 (fully premixed) to -1 (fully diffusive). Plotted for three different relevant solution points for case A and case B.

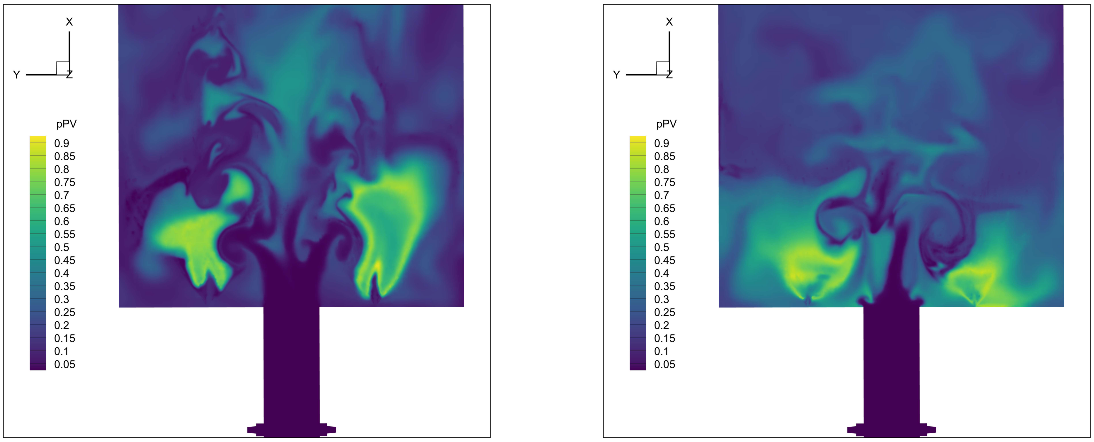

(a) case A, $t = 0.1\,s$

(b) case B,$t = 0.1\,s$

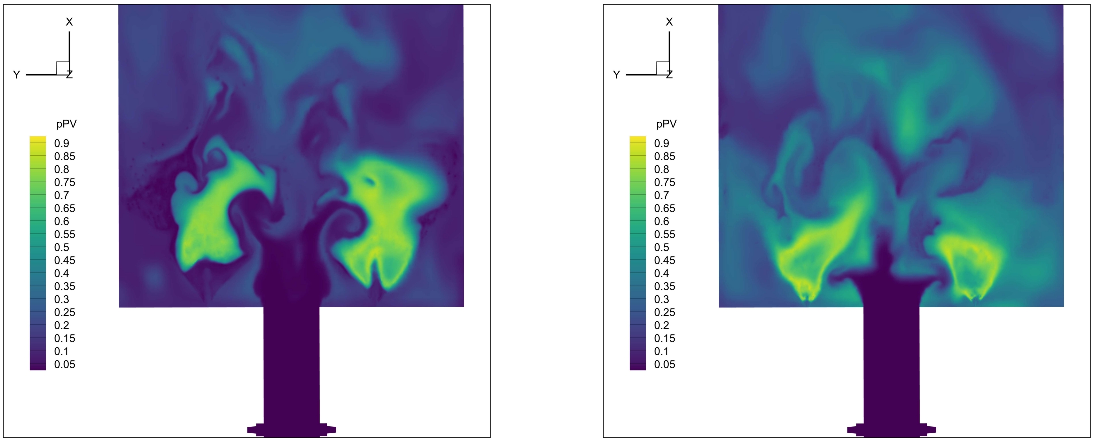

(c) case A, $t = 0.11\,s$

(d) case B, $t = 0.11\,s$

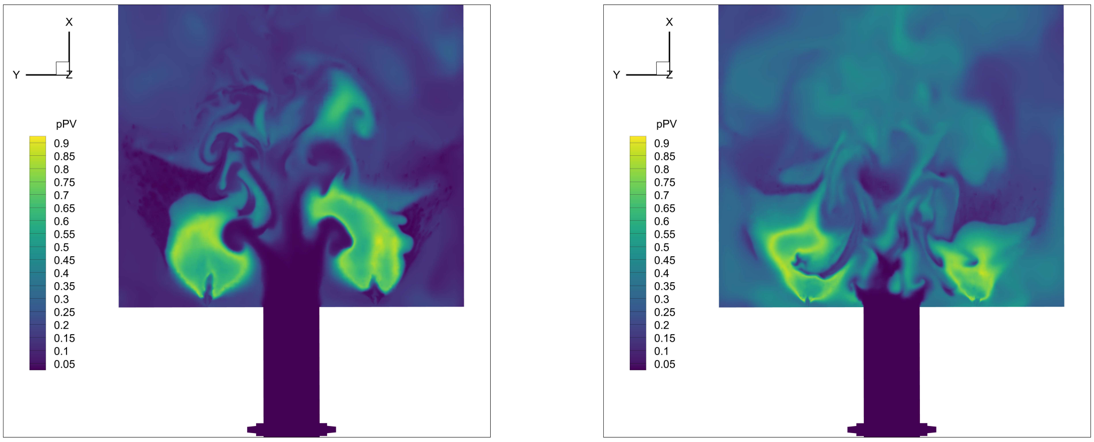

(e) case A, $t = 0.125\,s$

(f) case B, $t = 0.125\,s$

Figure B.7: Z=0 slice of pPV variable. Plotted for three different relevant solution points for case A and case B.

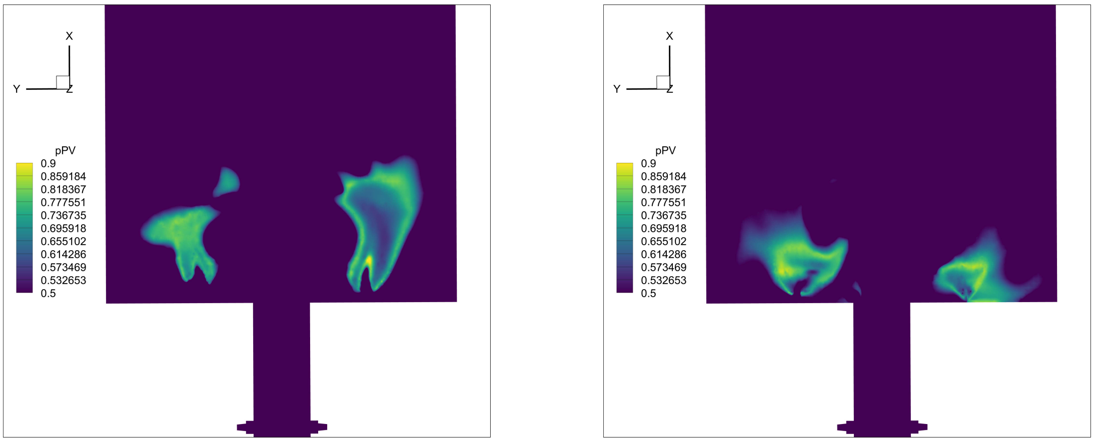

(a) case A, $t = 0.1\,s$

(b) case B,$t = 0.1\,s$

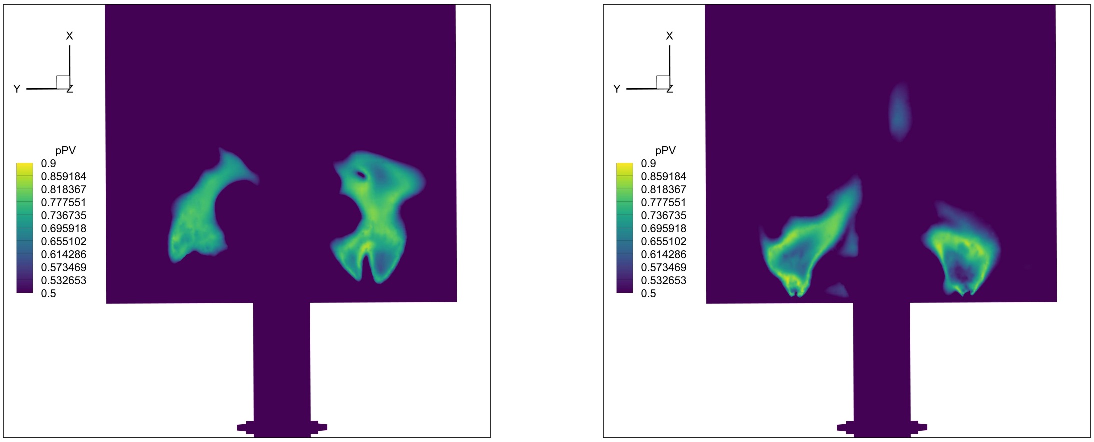

(c) case A, $t = 0.11\,s$

(d) case B, $t = 0.11\,s$

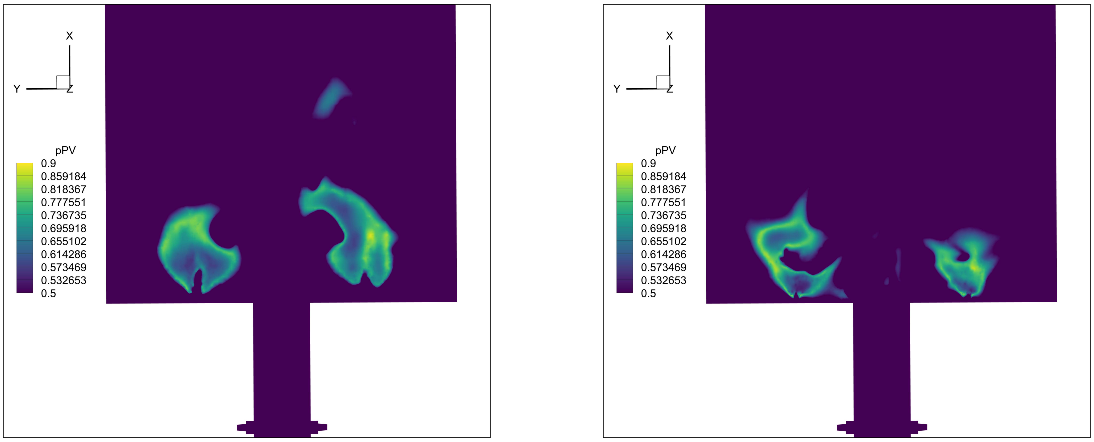

(e) case A, $t = 0.125\,s$

(f) case B, $t = 0.125\,s$

Figure B.8: Z=0 slice of pPV variable, contour capped to $pPV > 0.5$. Plotted for three different relevant solution points for case A and case B.

References

[1] United Nations Environment Programme (UNEP), “Emissions gap report 2024: No more hot air … please!” United Nations Environment Programme (UNEP), Tech. Rep., Oct. 2024, Accessed: 2025-11-03. [Online]. Available: `https://www.unep.org/resources/emissions-gap-report-2024`.

[2] G. G. Fleming, I. de Lépinay, and R. Schaufele, “Environmental trends in aviation to 2050,” *ICAO environmental report*, pp. 17–23, 2019.

[3] International Civil Aviation Organization (ICAO), “ICAO Environmental Report 2025,” ICAO, Tech. Rep., 2025. [Online]. Available: `https://www.icao.int/environmental-protection/Pages/envrep2025.aspx`.

[4] European Commission, Climate Action, *Reducing emissions from aviation*, Accessed: 2025-11-03, 2025. [Online]. Available: `https://climate.ec.europa.eu/eu-action/transport-decarbonisation/reducing-emissions-aviation_en`.

[5] International Energy Agency (IEA), *Global total commercial air passenger traffic, 2019–2023*, Licence: CC BY 4.0, Paris, 2025. [Online]. Available: `https://www.iea.org/data-and-statistics/charts/global-total-commercial-air-passenger-traffic-2019-2023-2`.

[6] International Energy Agency (IEA), *Co2 emissions in aviation in the net zero scenario, 2000–2030*, Licence: CC BY 4.0, Paris, 2025. [Online]. Available: `https://www.iea.org/data-and-statistics/charts/co2-emissions-in-aviation-in-the-net-zero-scenario-2000-2030`.

[7] R. Teoh, Z. Engberg, M. Shapiro, L. Dray, and M. E. J. Stettler, “The high-resolution global aviation emissions inventory based on ads-b (gaia) for 2019–2021,” *Atmospheric Chemistry and Physics*, vol. 24, no. 1, pp. 725–744, 2024. DOI: `10.5194/acp-24-725-2024`.

[8] D. Lee et al., “The contribution of global aviation to anthropogenic climate forcing for 2000 to 2018,” *Atmospheric Environment*, vol. 244, p. 117 834, 2021, ISSN: 1352-2310. DOI: `https://doi.org/10.1016/j.atmosenv.2020.117834`.

[9] S. D. Eastham, G. P. Chossière, R. L. Speth, D. J. Jacob, and S. R. H. Barrett, “Global impacts of aviation on air quality evaluated at high resolution,” *Atmospheric Chemistry and Physics*, vol. 24, no. 4, pp. 2687–2703, 2024. DOI: `10.5194/acp-24-2687-2024`. [Online]. Available: `https://acp.copernicus.org/articles/24/2687/2024/`.

[10] S. D. Eastham and S. R. Barrett, “Aviation-attributable ozone as a driver for changes in mortality related to air quality and skin cancer,” *Atmospheric Environment*, vol. 144, pp. 17–23, 2016, ISSN: 1352-2310. DOI: `https://doi.org/10.1016/j.atmosenv.2016.08.040`.

[11] D. B. Whitt, M. Z. Jacobson, J. T. Wilkerson, A. D. Naiman, and S. K. Lele, “Vertical mixing of commercial aviation emissions from cruise altitude to the surface,” *Journal of Geophysical Research: Atmospheres*, vol. 116, no. D14, 2011. DOI: `https://doi.org/10.1029/2010JD015532`.

[12] P. Mehta, “Science behind acid rain: Analysis of its impacts and advantages on life and heritage structures,” *south Asian journal of tourism and heritage*, vol. 3, no. 2, pp. 123–132, 2010.

[13] U. Trivanovic and S. E. Pratsinis, “Opinion: Eliminating aircraft soot emissions,” *Aerosol Research*, vol. 2, no. 2, pp. 207–223, 2024. DOI: `10.5194/ar-2-207-2024`.

[14] T. C. Bond et al., “Bounding the role of black carbon in the climate system: A scientific assessment,” *Journal of Geophysical Research: Atmospheres*, vol. 118, no. 11, pp. 5380–5552, 2013. DOI: `https://doi.org/10.1002/jgrd.50171`.

[15] Z. Liu, S. Yu, and X. Yang, "Insight of effects of air quality and sustainable aviation fuel blend on energy saving and emission reduction in airport," *Bioresources and Bioprocessing*, vol. 11, no. 1, p. 84, 2024.

[16] European Union Aviation Safety Agency (EASA), "European Aviation Environmental Report 2025," EASA, with support from the European Commission, EEA, and EUROCONTROL, Tech. Rep. TO-01-24-000-EN-N, 2025. DOI: `10.2822/1537033`. [Online]. Available: `https://www.easa.europa.eu/en/domains/environment/eaer`.

[17] J. Holladay, Z. Abdullah, and J. Heyne, "Sustainable aviation fuel: Review of technical pathways," U.S. Department of Energy, Office of Energy Efficiency and Renewable Energy, Bioenergy Technologies Office, Tech. Rep. DOE/EE-2041, 2020, OSTI ID: 1660415; 81 pp. DOI: `10.2172/1660415`. [Online]. Available: `https://www.energy.gov/sites/default/files/2020/09/f78/beto-sust-aviation-fuel-sep-2020.pdf`.

[18] International Civil Aviation Organization (ICAO), *Corsia eligible fuels*, `https://www.icao.int/environmental-protection/CORSIA/Pages/CORSIA-Eligible-Fuels.aspx`, 2025.

[19] International Civil Aviation Organization (ICAO), "Corsia default life cycle emissions values for corsia eligible fuels, seventh edition," ICAO, Tech. Rep. ICAO Document 06, 2025.

[20] L. Boerboom, A. Gangoli Rao, G. Volker, and F. Yin, "A comprehensive well-to-wake climate impact assessment of sustainable aviation fuel," *Scientific Reports*, vol. 15, Aug. 2025. DOI: `10.1038/s41598-025-13445-x`.

[21] European Parliament & Council of the European Union, *Regulation (eu) 2023/2405 on ensuring a level playing field for sustainable air transport (refueleu aviation)*, `https://eur-lex.europa.eu/eli/reg/2023/2405/oj`, Art.4(1)(f) requires 70% SAF share by 2050, 2023.

[22] N. Pavlenko and S. Searle, "Assessing the sustainability implications of alternative aviation fuels," *International Council on Clean Transportation*, vol. 11, 2021.

[23] A. Bell, L. A. Mannion, M. Kelly, R. Parker, M. R. Ghaani, and S. Dooley, "Life cycle co2e intensity of power-to-liquid sustainable aviation fuel scenarios and specific use cases," *Advances in Applied Energy*, vol. 20, p. 100 248, 2025, ISSN: 2666-7924. DOI: `https://doi.org/10.1016/j.adapen.2025.100248`.

[24] Alliance for Zero-Emission Aviation (AZEA) Working Group 4, "Current standardization landscape," Alliance for Zero-Emission Aviation, Brussels, Belgium, Tech. Rep., 2023. [Online]. Available: `https://defence-industry-space.ec.europa.eu/system/files/2023-06/Current%20Standardization%20Landscape.pdf`.

[25] Air Transport Action Group, "Waypoint 2050: 2nd edition — september 2021 (full report)," Air Transport Action Group, 2021. [Online]. Available: `https://aviationbenefits.org/media/167417/w2050_v2021_27sept_full.pdf`.

[26] A. Bauen, N. Bitossi, L. German, A. Harris, and K. Leow, "Sustainable aviation fuels," *Johnson Matthey Technology Review*, vol. 64, Jul. 2020. DOI: `10.1595/205651320X15816756012040`.

[27] A. Sharma and M. Arief, "Hydrogen in aviation: Evaluating the feasibility and benefits of a green fuel alternative," *Journal of High School Research*, vol. 2, Apr. 2025. DOI: `10.70671/hjf9f116`.

[28] D. Verstraete, "Long range transport aircraft using hydrogen fuel," *International Journal of Hydrogen Energy*, vol. 38, no. 34, pp. 14 824–14 831, 2013, ISSN: 0360-3199. DOI: `https://doi.org/10.1016/j.ijhydene.2013.09.021`.

[29] D. Verstraete, "On the energy efficiency of hydrogen-fuelled transport aircraft," *International Journal of Hydrogen Energy*, vol. 40, no. 23, pp. 7388–7394, 2015, ISSN: 0360-3199. DOI: `https://doi.org/10.1016/j.ijhydene.2015.04.055`.

[30] International Air Transport Association (IATA), "Fact sheet 7: Liquid hydrogen as a potential low-carbon fuel for aviation," IATA, Tech. Rep., 2020. [Online]. Available: `https://www.iata.org/contentassets/d13875e9ed784f75bac90f000760e998/fact_sheet7-hydrogen-fact-sheet_072020.pdf`.

[31] P. Agarwal, X. Sun, P. Q. Gauthier, and V. Sethi, “Injector design space exploration for an ultra-low no$_x$ hydrogen micromix combustion system,” in *Proceedings of ASME Turbo Expo 2019: Turbomachinery Technical Conference and Exposition (GT2019)*, American Society of Mechanical Engineers, 2019. DOI: 10.1115/GT2019-90833. [Online]. Available: https://asmedigitalcollection.asme.org/GT/proceedings/GT2019/58608/V003T03A013/1066673.

[32] A. Ebrahimi, A. Rolt, S. Jafari, and J. H. Anton, “A review on liquid hydrogen fuel systems in aircraft applications for gas turbine engines,” *International Journal of Hydrogen Energy*, vol. 91, pp. 88–105, 2024, ISSN: 0360-3199. DOI: https://doi.org/10.1016/j.ijhydene.2024.10.121.

[33] M. Ponater, R. Sausen, U. Schumann, and M. S. Shine, “Potential of the cryoplane technology to reduce aircraft environmental impact,” *Atmospheric Environment*, vol. 40, no. 33, pp. 6928–6935, 2006. DOI: 10.1016/j.atmosenv.2006.06.049.

[34] A. Boretti, “Transitioning from low-emission dry micro-mix hydrogen-air combustion to zero-emission wet micro-mix hydrogen-oxygen combustion in hydrogen energy storage systems,” *International Journal of Hydrogen Energy*, vol. 67, pp. 1066–1073, 2024, ISSN: 0360-3199. DOI: https://doi.org/10.1016/j.ijhydene.2024.02.257.

[35] E. Munktell, *Sustainable aviation: Adding hydrogen propulsion to jet engine designs*, Blog post on the Siemens Simcenter website, Accessed 2025-11-26, 2023. [Online]. Available: https://blogs.sw.siemens.com/simcenter/hydrogen-jet-engine-designs/.

[36] Aerospace Technology Institute (ATI), *Flyzero – zero-carbon emission air travel via liquid-hydrogen aircraft*, ATI project page; provides links to FlyZero reports and project summary, 2022. Accessed: Nov. 25, 2025. [Online]. Available: https://www.ati.org.uk/flyzero/.

[37] Pratt & Whitney, *Pratt & whitney awarded department of energy project to develop hydrogen propulsion technology*, Press release on Pratt & Whitney website, Feb. 2022. Accessed: Nov. 25, 2025. [Online]. Available: https://www.prattwhitney.com/en/newsroom/news/2022/02/21/pw-awarded-department-of-energy-project-to-develop-hydrogen-propulsion-technology.

[38] CRYOPLANE Consortium, “Liquid hydrogen fuelled aircraft – system analysis (cryoplane): Final technical report,” Technische Universität Hamburg□Harburg, European Commission, Final Technical Report, 2003. Accessed: Nov. 25, 2025. [Online]. Available: https://www.fzt.haw-hamburg.de/pers/Scholz/dglr/hh/text_2004_02_26_Cryoplane.pdf.

[39] J. Burguburu, G. Cabot, B. Renou, A. M. Boukhalfa, and M. Cazalens, “Effects of h2 enrichment on flame stability and pollutant emissions for a kerosene/air swirled flame with an aeronautical fuel injector,” *Proceedings of the Combustion Institute*, vol. 33, no. 2, pp. 2927–2935, 2011.

[40] J. Burguburu, G. Cabot, B. Renou, A. Boukhalfa, and M. Cazalens, “Comparisons of the impact of reformer gas and hydrogen enrichment on flame stability and pollutant emissions for a kerosene/air swirled flame with an aeronautical fuel injector,” *International journal of hydrogen energy*, vol. 36, no. 11, pp. 6925–6936, 2011.

[41] J. Frenillot, G. Cabot, M. Cazalens, B. Renou, and M. Boukhalfa, “Impact of h2 addition on flame stability and pollutant emissions for an atmospheric kerosene/air swirled flame of laboratory scaled gas turbine,” *International Journal of Hydrogen Energy*, vol. 34, no. 9, pp. 3930–3944, 2009.

[42] G. Juste, “Hydrogen injection as additional fuel in gas turbine combustor. evaluation of effects,” *International Journal of Hydrogen Energy*, vol. 31, no. 14, pp. 2112–2121, 2006.

[43] H. Hiroyaso, M. Arai, T. Kadota, and J. Yoso, “An experimental study on kerosene-hydrogen hybrid combustion in a gas turbine combustor,” *Bulletin of JSME*, vol. 23, no. 184, pp. 1655–1662, 1980. DOI: 10.1299/jsme1958.23.1655.

[44] K. Dave, S. Link, F. De Domenico, F. Schrijer, F. Scarano, and A. G. Rao, “Kerosene-h2 blending effects on flame properties in a multi-fuel combustor,” *Fuel Communications*, p. 100 139, 2025.

[45] X. Hui, C. Zhang, M. Xia, and C.-J. Sung, “Effects of hydrogen addition on combustion characteristics of n-decane/air mixtures,” *Combustion and flame*, vol. 161, no. 9, pp. 2252–2262, 2014.

[46] L. Palanti et al., “Cfd-based scouting for the design of a multi-fuel kerosene/hydrogen atmospheric burner,” in *34th Congress of the International Council of the Aeronautical Sciences*, ICAS, 2024, ICAS–2024.

[47] G. A. Richards, P. E. Sojka, and A. H. Lefebvre, “Flame speeds in fuel sprays with hydrogen addition,” *Journal of Engineering for Gas Turbines and Power*, vol. 111, no. 1, pp. 84–89, Jan. 1989, ISSN: 0742-4795. DOI: `10.1115/1.3240231`. eprint: `https://asmedigitalcollection.asme.org/gasturbinespower/article-pdf/111/1/84/5888550/84\_1.pdf`. [Online]. Available: `https://doi.org/10.1115/1.3240231`.

[48] G. Yu, C. Law, and C. Wu, “Laminar flame speeds of hydrocarbon + air mixtures with hydrogen addition,” *Combustion and Flame*, vol. 63, no. 3, pp. 339–347, 1986, ISSN: 0010-2180. DOI: `https://doi.org/10.1016/0010-2180(86)90003-9`.

[49] C. Law and O. Kwon, “Effects of hydrocarbon substitution on atmospheric hydrogen–air flame propagation,” *International Journal of Hydrogen Energy*, vol. 29, no. 8, pp. 867–879, 2004, ISSN: 0360-3199. DOI: `https://doi.org/10.1016/j.ijhydene.2003.09.012`. [Online]. Available: `https://www.sciencedirect.com/science/article/pii/S0360319903002519`.

[50] W. Zeng, J. Liu, Y. Liu, B. Chen, and A. Liu, “The effect of hydrogen addition on the combustion characteristics of rp-3 kerosene/air premixed flames,” *Energies*, vol. 10, no. 8, p. 1107, 2017.

[51] R. Kurz, C. Etheridge, and R. Kaiser, “On fuel suitability for gas turbines,” in *Turbomachinery and Pump Symposia*, Texas A&M University, Turbomachinery Laboratories, 2004, pp. 67–66. [Online]. Available: `https://hdl.handle.net/1969.1/163241`.

[52] F. H. Vance, H. Nicolai, and C. Hasse, “A numerical investigation into the stabilization of hydrogen enriched n-dodecane premixed flames,” *International Journal of Hydrogen Energy*, vol. 56, pp. 611–620, 2024.

[53] A. H. Lefebvre, “Fuel effects on gas turbine combustion—ignition, stability, and combustion efficiency,” *Journal of Engineering for Gas Turbines and Power*, vol. 107, no. 1, pp. 24–37, Jan. 1985, ISSN: 0742-4795. DOI: `10.1115/1.3239693`. eprint: `https://asmedigitalcollection.asme.org/gasturbinespower/article-pdf/107/1/24/5759046/24\_1.pdf`. [Online]. Available: `https://doi.org/10.1115/1.3239693`.

[54] Y. M. Annushkin and G. F. Maslov, “Efficiency of combustion of hydrogen-kerosene fuel in a straight duct,” *Combustion, Explosion and Shock Waves*, vol. 21, no. 3, pp. 297–298, 1985.

[55] S. Michaux, K. Chatelain, W. Roberts, and D. Lacoste, “Laminar burning velocities of hydrogen-air and methane-air flames from ambient to cryogenic temperatures at different equivalence ratios,” *International Journal of Hydrogen Energy*, vol. 100, pp. 608–616, Jan. 2025. DOI: `10.1016/j.ijhydene.2024.12.114`.

[56] A. Ghosh, N. M. Munoz-Munoz, K. P. Chatelain, and D. A. Lacoste, “Laminar burning velocity of hydrogen, methane, ethane, ethylene, and propane flames at near-cryogenic temperatures,” *Applications in Energy and Combustion Science*, vol. 12, p. 100 094, 2022, ISSN: 2666-352X. DOI: `https://doi.org/10.1016/j.jaecs.2022.100094`.

[57] I. Ibrahim, A. Elzallat, M. Elsakka, T. Farag, and H. Gad, “Effect of atomizing gas type on kerosene spray combustion using gas-blast atomizer: A comparative numerical study,” *Applied Thermal Engineering*, vol. 239, p. 121 996, 2024.

[58] S. Tamang and H. Park, “Numerical investigation of combustion characteristics for hydrogen mixed fuel in a can-type model of the gas turbine combustor,” *International Journal of Hydrogen Energy*, vol. 48, no. 30, pp. 11 493–11 512, 2023.

[59] H. Yilmaz, O. Cam, S. Tangoz, and I. Yilmaz, “Effect of different turbulence models on combustion and emission characteristics of hydrogen/air flames,” *international journal of hydrogen energy*, vol. 42, no. 40, pp. 25 744–25 755, 2017.

[60] A. Giusti and E. Mastorakos, “Turbulent combustion modelling and experiments: Recent trends and developments,” *Flow, Turbulence and Combustion*, vol. 103, no. 4, pp. 847–869, 2019.

[61] S. B. Pope, “Ten questions concerning the large-eddy simulation of turbulent flows,” *New Journal of Physics*, vol. 6, no. 1, p. 35, Mar. 2004. DOI: `10.1088/1367-2630/6/1/035`.

[62] S. B. Pope, *Turbulent Flows*. Cambridge: Cambridge University Press, 2000, ISBN: 978-0-521-59886-6, 978-0-521-59125-6. DOI: `10.1017/CBO9781316179475`.

[63] H. A. Alabaş and B. A. Çeper, “Effect of the hydrogen/kerosene blend on the combustion characteristics and pollutant emissions in a mini jet engine under cdc conditions,” *International Journal of Hydrogen Energy*, vol. 52, pp. 1275–1287, 2024.

[64] N. Smirnov and V. Nikitin, “Modeling and simulation of hydrogen combustion in engines,” *International Journal of Hydrogen Energy*, vol. 39, no. 2, pp. 1122–1136, 2014.

[65] X. Yang, T. Xi, Y. Qin, H. Zhang, and Y. Wang, “Computational fluid dynamics–discrete phase method simulations in process engineering: A review of recent progress,” *Applied Sciences*, vol. 14, no. 9, p. 3856, 2024.

[66] H. Pitsch, “Large-eddy simulation of turbulent combustion,” *Annual Review of Fluid Mechanics*, vol. 38, pp. 453–482, Jan. 2006. DOI: `10.1146/annurev.fluid.38.050304.092133`.

[67] G. Ferrante, Z. X. Chen, and I. Langella, “Dynamic modelling of subgrid scalar dissipation rate in premixed and partially premixed flames with differential filter,” *Applied Thermal Engineering*, vol. 248, p. 123 233, 2024.

[68] J. V. Oijen and L. D. Goey, “Modelling of premixed laminar flames using flamelet-generated manifolds,” *Combustion Science and Technology*, vol. 161, no. 1, pp. 113–137, 2000. DOI: `10.1080/00102200008935814`. [Online]. Available: `https://doi.org/10.1080/00102200008935814`.

[69] G. Lemmi et al., “Fgm vs atf: A comparative les analysis in predicting the flame characteristics of an industrial lean premixed burner for gas turbine applications,” *Fuel Communications*, vol. 19, p. 100 117, 2024.

[70] E. Pérez-Sánchez, E. Fortes, and D. Mira, “Assessment of the flamelet generated manifold method with preferential diffusion modelling for the prediction of partially premixed hydrogen flames,” Dec. 2023. DOI: `10.48550/arXiv.2312.00929`. [Online]. Available: `https://api.semanticscholar.org/CorpusID:265609301`.

[71] T. Nilsson, I. Langella, N. A. K. Doan, N. Swaminathan, R. Yu, and X.-S. Bai, “A priori analysis of sub-grid variance of a reactive scalar using dns data of high ka flames,” *Combustion Theory and Modelling*, vol. 23, no. 5, pp. 885–906, 2019.

[72] F. Almutairi, K. R. Dinesh, and J. A. van Oijen, “Modelling of hydrogen-blended dual-fuel combustion using flamelet-generated manifold and preferential diffusion effects,” *international journal of hydrogen energy*, vol. 48, no. 4, pp. 1602–1624, 2023.

[73] G. Kuenne, A. Ketelheun, and J. Janicka, “Les modeling of premixed combustion using a thickened flame approach coupled with fgm tabulated chemistry,” *Combustion and Flame*, vol. 158, no. 9, pp. 1750–1767, 2011.

[74] K. Wan, Y. Huang, Z. Gao, Y. He, and C. Jiang, “Large-eddy simulation of a swirling aviation kerosene spray flame using 3-component surrogate fuels,” in *32nd Congress of the International Council of the Aeronautical Sciences, Shanghai China, Spetember*, 2021, pp. 6–10.

[75] B. Magnussen and B. Hjertager, “On mathematical modeling of turbulent combustion with special emphasis on soot formation and combustion,” *Symposium (International) on Combustion*, vol. 16, no. 1, pp. 719–729, 1977, ISSN: 0082-0784. DOI: `https://doi.org/10.1016/S0082-0784(77)80366-4`. [Online]. Available: `https://www.sciencedirect.com/science/article/pii/S0082078477803664`.

[76] P. Senecal et al., “Multi-dimensional modeling of direct-injection diesel spray liquid length and flame lift-off length using cfd and parallel detailed chemistry,” in *SAE International*, vol. 112, Mar. 2003. DOI: `10.4271/2003-01-1043`.

[77] P. Saxena and F. A. Williams, “Testing a small detailed chemical-kinetic mechanism for the combustion of hydrogen and carbon monoxide,” *Combustion and Flame*, vol. 145, no. 1-2, pp. 316–323, 2006.

[78] N. Zettervall, C. Fureby, and E. Nilsson, “A reduced chemical kinetic reaction mechanism for kerosene-air combustion,” *Fuel*, vol. 269, p. 117 446, 2020.

[79] C. V. Naik et al., “Detailed chemical kinetic mechanism for surrogates of alternative jet fuels,” *Combustion and Flame*, vol. 158, no. 3, pp. 434–445, 2011.

[80] D. G. Goodwin, H. K. Moffat, I. Schoegl, R. L. Speth, and B. W. Weber, *Cantera: An object-oriented software toolkit for chemical kinetics, thermodynamics, and transport processes*, `https://www.cantera.org`, Version 3.1.0, 2024. DOI: `10.5281/zenodo.14455267`.

[81] B. Somers and E. U. of Technology, *Chem1d*. swmath: `22208`. [Online]. Available: `https://www.tue.nl/en/university/departments/mechanical-engineering/research/research-groups/multiphase-and-reactive-flows/our-expertise/chem1d/`.

[82] S. Dong et al., “Applications in energy and combustion science,” 2022.

[83] H. Wang et al., “A physics-based approach to modeling real-fuel combustion chemistry - i. evidence from experiments, and thermodynamic, chemical kinetic and statistical considerations,” *Combustion and Flame*, vol. 193, pp. 502–519, 2018, ISSN: 0010-2180. DOI: `https://doi.org/10.1016/j.combustflame.2018.03.019`. [Online]. Available: `https://www.sciencedirect.com/science/article/pii/S0010218018301299`.

[84] R. Xu et al., “A physics-based approach to modeling real-fuel combustion chemistry–ii. reaction kinetic models of jet and rocket fuels,” *Combustion and Flame*, vol. 193, pp. 520–537, 2018, ISSN: 0010-2180. DOI: `https://doi.org/10.1016/j.combustflame.2018.03.021`. [Online]. Available: `https://www.sciencedirect.com/science/article/pii/S0010218018301317`.

[85] I. T. Delft, *Hight powered computational center nmr. 12*, `https://hpcwiki.tudelft.nl/index.php?title=Introduction`, 2024.

[86] D. H. P. C. C. (DHPC), *DelftBlue Supercomputer (Phase 2)*, `https://www.tudelft.nl/dhpc/ark:/44463/DelftBluePhase2`, 2024.

[87] Fluidics Instruments B.V., *Simplex atomizers*, Accessed: 2025-10-05, 2025. [Online]. Available: `https://fluidics.nl/product/simplex-atomizers/`.

[88] Convergent Science, *Converge 3.1 manual*, Available online at `https://convergecfd.com`, Madison, Wisconsin, 2021.

[89] K. J. Richards, P. K. Senecal, and E. Pomraning, *Converge 3.1.9*, Convergent Science, Madison, WI, 2025.

[90] C. Letty, E. Mastorakos, A. Masri, M. Juddoo, and W. O’Loughlin, “Structure of igniting ethanol and n-heptane spray flames with and without swirl,” *Experimental Thermal and Fluid Science*, vol. 43, pp. 47–54, Nov. 2012. DOI: `10.1016/j.expthermflusci.2012.03.020`.

[91] G. Asar, A. Khodir, and W. El-Askary, “Effect of atomizing air swirl angle on combustion and emission characteristics of spray flame,” *International Journal of Mechanical and Civil Engineering*, vol. 16, pp. 1–11, Apr. 2019. DOI: `10.9790/1684-1602050111`.

[92] G. Hindi, E. Paladino, and A. A. M. de Oliviera, “Effect of mesh refinement and model parameters on les simulation of diesel sprays,” *International Journal of Heat and Fluid Flow*, vol. 71, pp. 246–259, 2018, ISSN: 0142-727X. DOI: `https://doi.org/10.1016/j.ijheatfluidflow.2018.04.001`.

[93] Q. Xue et al., “Eulerian cfd modeling of coupled nozzle flow and spray with validation against x-ray radiography data,” *SAE International Journal of Engines*, vol. 7, Apr. 2014. DOI: `10.4271/2014-01-1425`.

[94] L. Bravo, Q. Xue, S. Som, C. Powell, and C.-B. Kweon, “Fuel effects on nozzle flow and spray using fully coupled eulerian simulations,” Jun. 2015. DOI: `10.1115/POWER2015-49554`.

[95] Q. Xue et al., “An eulerian cfd model and x-ray radiography for coupled nozzle flow and spray in internal combustion engines,” *International Journal of Multiphase Flow*, vol. 70, pp. 77–88, 2015, ISSN: 0301-9322. DOI: `https://doi.org/10.1016/j.ijmultiphaseflow.2014.11.012`.

[96] E. Pomraning, “Development of large eddy simulation turbulence models,” Ph.D. dissertation, University of Wisconsin-Madison, Dec. 2000. DOI: `10.13140/2.1.2035.7929`.

[97] S. Cant, “Rans and les modelling of premixed turbulent combustion,” in *Turbulent Combustion Modeling: Advances, New Trends and Perspectives*, T. Echekki and E. Mastorakos, Eds. Dordrecht: Springer Netherlands, 2011, ISBN: 978-94-007-0412-1. DOI: `10.1007/978-94-007-0412-1_4`. [Online]. Available: `https://doi.org/10.1007/978-94-007-0412-1_4`.

[98] H. K. Versteeg and W. Malalasekera, *An Introduction to Computational Fluid Dynamics: The Finite Volume Method*, Second. Harlow, Essex, England; New York: Longman Scientific & Technical; Wiley, 2007, ISBN: 978-0-13-127498-3.

[99] www.idealsimulations.com. "Turbulence models in cfd - rans, des, les and dns," Accessed: Oct. 8, 2025. [Online]. Available: `https://www.idealsimulations.com/resources/turbulence-models-in-cfd/`.

[100] I. Langella, N. A. K. Doan, N. Swaminathan, and S. B. Pope, "Study of subgrid-scale velocity models for reacting and nonreacting flows," *Physical Review Fluids*, vol. 3, no. 5, p. 054 602, 2018.

[101] J. Guerrero, *Large eddy simulation (les) - part 2*, Lecture slides accessed: 2025-03-21, 2021. [Online]. Available: `http://www.dicat.unige.it/guerrero/turbulence2021/slides/lecture10/10LES_p2.pdf`.

[102] G. Ferrante, L. Doodeman, A. G. Rao, and I. Langella, "Les of hydrogen-enriched methane flames in a lean-burn combustor with axial air injection," in *Turbo Expo: Power for Land, Sea, and Air*, American Society of Mechanical Engineers, vol. 86960, 2023, V03BT04A015.

[103] B. Magnussen, "On the structure of turbulence and a generalized eddy dissipation concept for chemical reaction in turbulent flow," in *19th Aerospace Sciences Meeting*, 1981. DOI: `10.2514/6.1981-42`. [Online]. Available: `https://arc.aiaa.org/doi/10.2514/6.1981-42`.

[104] J. Smagorinsky, "General circulation experiments with the primitive equation i: The basic experiment," *Monthly Weather Review*, vol. 91, pp. 99–164, 1963. DOI: `10.1175/1520-0493(1963)091<0099:GCEWTP>2.3.CO;2`. [Online]. Available: `http://dx.doi.org/10.1175/1520-0493(1963)091%3C0099:GCEWTP%3E2.3.CO;2`.

[105] H. Werner and H. Wengle, "Large-eddy simulation of turbulent flow over and around a cube in a plate channel," in *Turbulent Shear Flows 8*, F. "Durst, R. Friedrich, B. E. Launder, F. W. Schmidt, U. Schumann, and J. H. Whitelaw, Eds., Berlin, Heidelberg: Springer Berlin Heidelberg, 1993, pp. 155–168, ISBN: 978-3-642-77674-8.

[106] R. McDermott, *Fds wall flows part i: Straight channels*, en, 2009-07-10 2009. [Online]. Available: `https://tsapps.nist.gov/publication/get_pdf.cfm?pub_id=902843`.

[107] M. Breuer, B. Kniazev, and M. Abel, "Development of wall models for les of separated flows using statistical evaluations," *Computers Fluids*, vol. 36, no. 5, pp. 817–837, 2007, ISSN: 0045-7930. DOI: `https://doi.org/10.1016/j.compfluid.2006.09.001`. [Online]. Available: `https://www.sciencedirect.com/science/article/pii/S0045793006001046`.

[108] P. Jenny, D. Roekaerts, and N. Beishuizen, "Modeling of turbulent dilute spray combustion," *Progress in Energy and Combustion Science*, vol. 38, pp. 846–887, Dec. 2012. DOI: `10.1016/j.pecs.2012.07.001`.

[109] S. S. Sazhin, "Advanced models of fuel droplet heating and evaporation," *Progress in energy and combustion science*, vol. 32, no. 2, pp. 162–214, 2006.

[110] P. R. Pousada, N. A. K. Doan, K. Aditya, M. Düsing, A. Ciani, and I. Langella, "Flashback prevention in a hydrogen-fueled reheat combustor by water injection optimized with global sensitivity analysis," *Journal of Engineering for Gas Turbines and Power*, vol. 147, no. 6, 2025.

[111] A. A. Amsden, P. J. O'Rourke, and T. D. Butler, "Kiva-ii: A computer program for chemically reactive flows with sprays," Los Alamos National Lab. (LANL), Los Alamos, NM (United States), Tech. Rep., May 1989. DOI: `10.2172/6228444`. [Online]. Available: `https://www.osti.gov/biblio/6228444`.

[112] A. H. Lefebvre and V. G. McDonell, *Atomization and sprays / arthur h. lefebvre and vincent g. mcdonell.* Boca Raton ; 2017. DOI: `https://doi.org/10.1201/9781315120911`.

[113] P. Senecal, E. Pomraning, K. Richards, and S. Som, "Grid-convergent spray models for internal combustion engine cfd simulations," Sep. 2012. DOI: `10.1115/ICEF2012-92043`.

[114] I. E. Barton, "Comparison of SIMPLE- and PISO-type algorithms for transient flows," *International Journal for Numerical Methods in Fluids*, vol. 26, no. 4, pp. 459–483, Feb. 1998. DOI: `10.1002/(SICI)1097-0363(19980228)26:4<459::AID-FLD645>3.0.CO;2-U`.

[115] W. K. Chow and Y. L. Cheung, "Comparison of the algorithms piso and simpler for solving pressure-velocity linked equations in simulating compartmental fire," *Numerical Heat Transfer, Part A: Applications*, vol. 31, no. 1, pp. 87–112, 1997. DOI: `10.1080/10407789708914027`.

[116] W. Kahan, "Gauss-seidel methods for solving large systems," Ph.D. dissertation, University of Toronto, Toronto, 1958.

[117] M. M. Martins, "Note on irreducible diagonally dominant matrices and the convergence of the aor iterative method," *Mathematics of Computation*, vol. 37, no. 155, pp. 101–103, 1981, ISSN: 00255718, 10886842.

[118] F. Durst, "Numerical solutions of the basic equations," in *Fluid Mechanics: An Introduction to the Theory of Fluid Flows*. Berlin, Heidelberg: Springer Berlin Heidelberg, 2022, pp. 671–714, ISBN: 978-3-662-63915-3. DOI: `10.1007/978-3-662-63915-3_20`.

[119] A. M. Simei and Y. Saad, Eds., *Krylov Subspace Methods for Linear Systems* (Springer Series in Computational Mathematics). Cham, Switzerland: Springer, 2022, vol. 60, ISBN: 978-981-19-8531-7. [Online]. Available: `https://doi.org/10.1007/978-981-19-8532-4`.

[120] K. Ahuja, "Recycling bi-lanczos algorithms: Bicg, cgs, and bicgstab," M.S. thesis, Virginia Polytechnic Institute and State University, Blacksburg, VA, USA, 2009. [Online]. Available: `http://hdl.handle.net/10919/34765`.

[121] H. A. van der Vorst, "Bi-cgstab: A fast and smoothly converging variant of bi-cg for the solution of nonsymmetric linear systems," *SIAM Journal on Scientific and Statistical Computing*, vol. 13, no. 2, pp. 631–644, 1992. DOI: `10.1137/0913035`.

[122] A. Y. Klimenko, "Multicomponent diffusion of various admixtures in turbulent flow," *Fluid dynamics*, vol. 25, no. 3, pp. 327–334, 1990.

[123] C. Science. "Gas turbines – converge cfd software applications," Accessed: Dec. 5, 2025. [Online]. Available: `https://convergecfd.com/applications/gas-turbines`.

[124] V. Shettihalli Anandreddy, "Calibration and validation of efficient combustion and emission models for 3d-cfd engine simulations," ISRN: LIU-IEI-TEK-A–19/03617–SE, Master's Thesis, Linköping University, Department of Management, Engineering, Applied Thermodynamics, and Fluid Mechanics, Linköping, Sweden, 2019. [Online]. Available: `https://liu.diva-portal.org/smash/record.jsf?pid=diva2:1525203`.

[125] N. Zettervall, C. Fureby, and E. Nilsson, "Small skeletal kinetic mechanism for kerosene combustion," *Energy & Fuels*, vol. 30, no. 11, pp. 9801–9813, 2016.

[126] R. Xu, H. Wang, M. Colket, and T. Edwards, "Thermochemical properties of jet fuels," Stanford University, HAI-Wang Lab / HyChem Project, Tech. Rep., Jul. 2015, HyChem report — thermochemical data for conventional and alternative jet fuels. Accessed: Nov. 25, 2025. [Online]. Available: `https://web.stanford.edu/group/haiwanglab/HyChem/approach/Report_Jet_Fuel_Thermochemical_Properties_v6.pdf`.

[127] S. De, A. K. Agarwal, S. Chaudhuri, and S. Sen, Eds., *Modeling and Simulation of Turbulent Combustion* (Energy, Environment, and Sustainability), 1st ed. Singapore: Springer Singapore, 2018, ISBN: 978-981-10-7409-7, 978-981-13-5628-5, 978-981-10-7410-3. DOI: `10.1007/978-981-10-7410-3`.

[128] N. Zettervall, "Methodology for developing reduced reaction mechanisms, and their use in combustion simulations," English, Doctoral Thesis, Lund University, Mar. 2021, ISBN: 978-91-7895-729-3.

[129] C. Ji, E. Dames, Y. L. Wang, H. Wang, and F. N. Egolfopoulos, "Propagation and extinction of premixed c5–c12 n-alkane flames," *Combustion and Flame*, vol. 157, no. 2, pp. 277–287, 2010, ISSN: 0010-2180. DOI: `https://doi.org/10.1016/j.combustflame.2009.06.011`.

[130] K. Kumar and C.-J. Sung, "Laminar flame speeds and extinction limits of preheated n-decane/o2/n2 and n-dodecane/o2/n2 mixtures," *Combustion and Flame*, vol. 151, no. 1, pp. 209–224, 2007, ISSN: 0010-2180. DOI: `https://doi.org/10.1016/j.combustflame.2007.05.002`.

[131] K. Kumar, C.-J. Sung, and X. Hui, "Laminar flame speeds and extinction limits of conventional and alternative jet fuels," *Fuel*, vol. 90, no. 3, pp. 1004–1011, 2011, ISSN: 0016-2361. DOI: `https://doi.org/10.1016/j.fuel.2010.11.022`.

[132] X. Hui and C.-J. Sung, “Laminar flame speeds of transportation-relevant hydrocarbons and jet fuels at elevated temperatures and pressures,” *Fuel*, vol. 109, pp. 191–200, 2013, ISSN: 0016-2361. DOI: `https://doi.org/10.1016/j.fuel.2012.12.084`. [Online]. Available: `https://www.sciencedirect.com/science/article/pii/S0016236112011088`.

[133] A. Larsson et al., “Skeletal methane–air reaction mechanism for large eddy simulation of turbulent microwave-assisted combustion,” *Energy & Fuels*, vol. 31, no. 2, pp. 1904–1926, 2017.

[134] M. Ó Conaire, H. J. Curran, J. M. Simmie, W. J. Pitz, and C. K. Westbrook, “A comprehensive modeling study of hydrogen oxidation,” *International journal of chemical kinetics*, vol. 36, no. 11, pp. 603–622, 2004.

[135] S. Aly and H. Salem, “Prediction of premixed laminar flame characteristics of commercial kerosene fuel,” *Fuel*, vol. 68, no. 9, pp. 1203–1209, 1989, ISSN: 0016-2361. DOI: `https://doi.org/10.1016/0016-2361(89)90196-8`. [Online]. Available: `https://www.sciencedirect.com/science/article/pii/0016236189901968`.

[136] V. Robin, A. Mura, and M. Champion, “Direct and indirect thermal expansion effects in turbulent premixed flames,” *Journal of Fluid Mechanics*, vol. 689, pp. 149–182, 2011. DOI: `10.1017/jfm.2011.409`.

[137] J.-P. Legier, T. Poinsot, and D. Veynante, “Dynamically thickened flame les model for premixed and non-premixed turbulent combustion,” in *Proceedings of the summer program*, Center for Turbulence Research Stanford, CA, vol. 12, 2000, pp. 157–168.

[138] T. Butler and P. O’Rourke, “A numerical method for two dimensional unsteady reacting flows,” *Symposium (International) on Combustion*, vol. 16, no. 1, pp. 1503–1515, 1977, ISSN: 0082-0784. DOI: `https://doi.org/10.1016/S0082-0784(77)80432-3`.

[139] C. Science, “Premixed combustion modeling,” Available for conference attendees or Converge users, 2022.

[140] T. Jaravel, “Prediction of pollutants in gas turbines using large eddy simulation,” Ph.D. dissertation, Institut National Polytechnique de Toulouse-INPT, 2016.

[141] Convergent Science, “Gas turbine modeling,” Available for conference attendees or Converge users, 2022.

[142] O. Colin, F. Ducros, D. Veynante, and T. Poinsot, “A thickened flame model for large eddy simulations of turbulent premixed combustion,” *Physics of fluids*, vol. 12, no. 7, pp. 1843–1863, 2000.

[143] B. Rochette, E. Riber, B. Cuenot, and O. Vermorel, “A generic and self-adapting method for flame detection and thickening in the thickened flame model,” *Combustion and Flame*, vol. 212, pp. 448–458, 2020, ISSN: 0010-2180. DOI: `https://doi.org/10.1016/j.combustflame.2019.11.015`. [Online]. Available: `https://www.sciencedirect.com/science/article/pii/S0010218019305206`.

[144] F. Charlette, C. Meneveau, and D. Veynante, “A power-law flame wrinkling model for les of premixed turbulent combustion part i: Non-dynamic formulation and initial tests,” *Combustion and Flame*, vol. 131, no. 1, pp. 159–180, 2002, ISSN: 0010-2180. DOI: `https://doi.org/10.1016/S0010-2180(02)00400-5`. [Online]. Available: `https://www.sciencedirect.com/science/article/pii/S0010218002004005`.

[145] F. Zhao, W. Yang, and W. Yu, “A progress review of practical soot modelling development in diesel engine combustion,” *Journal of Traffic and Transportation Engineering (English Edition)*, vol. 7, no. 3, pp. 269–281, 2020, Special Issue: Clean Alternative Fuels for Transport Vehicles, ISSN: 2095-7564. DOI: `https://doi.org/10.1016/j.jtte.2020.04.002`.

[146] H. Hiroyaso, T. Kadota, and M. Arai, “Development and use of a spray combustion modeling to predict diesel engine efficiency and pollutant emissions : Part 1 combustion modeling,” *Bulletin of JSME*, vol. 26, no. 214, pp. 569–575, 1983. DOI: `10.1299/jsme1958.26.569`.

[147] J. F. Nagle and R. F. Strickland-Constable, “Oxidation of carbon between 1000–2000°c,” 1962. [Online]. Available: `https://api.semanticscholar.org/CorpusID:104212331`.

[148] A. Dempsey, “A comprehensive evaluation of diesel engine cfd modeling predictions using a semi-empirical soot model over a broad range of combustion systems,” *SAE International Journal of Engines*, vol. 11, pp. 1399–1420, Apr. 2018. DOI: `10.4271/2018-01-0242`.

[149] G. Ferrante, L. Doodeman, A. Gangoli Rao, and I. Langella, “Les of hydrogen-enriched methane flames in a lean-burn combustor with axial air injection,” Sep. 2023. DOI: `10.1115/GT2023-103006`.

[150] P. Glarborg, J. A. Miller, B. Ruscic, and S. J. Klippenstein, “Modeling nitrogen chemistry in combustion,” *Progress in Energy and Combustion Science*, vol. 67, pp. 31–68, 2018, ISSN: 0360-1285. DOI: `https://doi.org/10.1016/j.pecs.2018.01.002`.

[151] S. Naha and S. K. Aggarwal, “Fuel effects on nox emissions in partially premixed flames,” *Combustion and Flame*, vol. 139, no. 1, pp. 90–105, 2004, ISSN: 0010-2180. DOI: `https://doi.org/10.1016/j.combustflame.2004.07.006`.

[152] J. B. Heywood, *Internal Combustion Engine Fundamentals*. McGraw-Hill, Inc., 1988.

[153] C. J. Mueller, “The quantification of mixture stoichiometry when fuel molecules contain oxidizer elements or oxidizer molecules contain fuel elements.,” Sandia National Laboratories, May 2005. [Online]. Available: `https://www.osti.gov/biblio/970223`.

[154] Q. Cazères, “Unifying definition of the local equivalence ratio for complex mixtures and the concept of bonding fraction,” *Combustion Theory and Modelling*, vol. 29, no. 2, pp. 177–195, 2025. DOI: `10.1080/13647830.2025.2464848`.

[155] B. Akkurt, “Modelling multi-pulse diesel injection with flamelet generated manifolds,” English, Proefschrift, Phd Thesis 1 (Research TU/e / Graduation TU/e), Mechanical Engineering, Feb. 2019, ISBN: 978-90-386-4666-4.

[156] P. Rahnama, A. Maghbouli, H. Bao, A. Vasavan, R. Novella, and B. Somers, “Generalizing progress variable definition in cfd simulation of combustion systems using tabulated chemistry models,” *Applications in Energy and Combustion Science*, vol. 14, p. 100 132, 2023, ISSN: 2666-352X. DOI: `https://doi.org/10.1016/j.jaecs.2023.100132`.

[157] Z. X. Chen, N. A. K. Doan, S. Ruan, I. Langella, and N. Swaminathan, “A priori investigation of subgrid correlation of mixture fraction and progress variable in partially premixed flames,” *Combustion Theory and Modelling*, vol. 22, no. 5, pp. 862–882, 2018. DOI: `10.1080/13647830.2018.1459862`.

[158] H. Yamashita, M. Shimada, and T. Takeno, “A numerical study on flame stability at the transition point of jet diffusion flames,” *Symposium (International) on Combustion*, vol. 26, no. 1, pp. 27–34, 1996, ISSN: 0082-0784. DOI: `https://doi.org/10.1016/S0082-0784(96)80196-2`.

[159] P. Koob, F. Ferraro, H. Nicolai, R. Eggels, M. Staufer, and C. Hasse, “Large eddy simulation of soot formation in a real aero-engine combustor using tabulated chemistry and a quadrature-based method of moments,” *Journal of Engineering for Gas Turbines and Power*, vol. 146, no. 1, p. 011 015, Nov. 2023, ISSN: 0742-4795. DOI: `10.1115/1.4063376`.

[160] D. Haworth, “Modeling Radiative Heat Transfer and Turbulence-Radiation Interactions Using PDF and FDF Methods,” in *APS Division of Fluid Dynamics Meeting Abstracts*, ser. APS Meeting Abstracts, Nov. 2019, C01.008, p. C01.008.

[161] J. C. R. Hunt, A. A. Wray, and P. Moin, “Eddies, streams, and convergence zones in turbulent flows,” in *Proceedings of the Summer Program*, Center for Turbulence Research, Stanford University, 1988, pp. 193–208.